Johan Fredrik Agerup

SOL energy transport and radiation loss modelling based on EMC3-EIRENE simulations of W7-X

Master's thesis in Applied Physics
Supervisor: Dr. Felix Reimold
Co-supervisor: Dr. Holger Reimerdes & Assoc. Prof. Jon Andreas Støvneng
September 2022

Master's thesis

NTNU
Norwegian University of
Science and Technology

MAX PLANCK
GESELLSCHAFT

EUROfusion

Johan Fredrik Agerup

SOL energy transport and radiation loss modelling based on EMC3-EIRENE simulations of W7-X

Master's thesis in Applied Physics
Supervisor: Dr. Felix Reimold
Co-supervisor: Dr. Holger Reimerdes & Assoc. Prof. Jon Andreas Støvneng
September 2022

Norwegian University of Science and Technology
Faculty of Natural Sciences
Department of Physics

NTNU
Norwegian University of
Science and Technology

MAX PLANCK INSTITUTE FOR PLASMA PHYSICS
NTNU - APPLIED PHYSICS AND MATHEMATICS

MASTER'S THESIS

SOL energy transport and radiation loss modelling based on EMC3-EIRENE simulations of W7-X

Institute Group: E5 - Impurity transport and radiation physics

Author:
Johan Fredrik Agerup

Supervisors:
Felix Reimold - Max Planck, IPP
Holger Reimerdes - EPFL, SPC
Jon Andreas Støvneng - NTNU, IFY

September 5, 2022

Abstract

Lengyel's and Feng's models for energy transport in the scrape-off layer are commonly applied to stellarator island divertors without justifying the validity of the assumptions imposed to simplify the models. This thesis presents a new framework for assessing the validity of the assumptions made by these models based on field line tracing of EMC3-EIRENE simulations covering a low and a high radiation scenario with total radiated power fraction $f_{rad} = 0.2$ and $f_{rad} = 0.8$, respectively. The framework is based on the concept of a limiting heat flux density at the target. We have examined field lines that intersect the target at the limiting locations and then evaluated the integral of the product of the energy sources and sinks and transport from upstream to the target. The framework aims to capture the driving physics of the peaks of the target heat flux distribution to predict the impurity concentration required for a certain radiated power fraction.

The global energy balance of the low and high radiation cases was shown to agree with Feng et al. (2021) [1]. An important observation is that the cross-field heat flux densities are concentrated around the X-points, so a large amount of power is transported to the PFR.

The parallel heat flux density profiles, the global energy balance and the approximated cross-field heat flux densities show that the energy transport is not conduction dominated nor dominated by parallel terms. Furthermore, the observed neutral losses in the SOL and the PFR are significant.

The effective radiated power loss function from the EMC3 simulations shows that the effect of impurity transport is significant. The integration of the effective radiated power loss function is not well approximated by assuming a constant impurity residence time for $f_{rad} = 0.2$ as it is characterised by transport from low to high-temperature regions and vice versa. Promising results are obtained for $f_{rad} = 0.8$ for transport from low to high-temperature regions, which is consistent with the observed inward movement of the radiation front. The field lines in the PFR have shorter connection lengths, so less power is removed through impurity radiation. Since a significant amount of power enters the PFR through cross-field transport, the PFR might be crucial to consider for power exhaust handling.

The loss from upstream to the target of the parallel electron conductive channel was used to assess the assumptions made in the simplified SOL energy transport models. The observed importance of heat convection disagrees with the assumption of conduction-dominated energy transport as the convection is significant and even dominant in some regions of the SOL. Furthermore, the effect of dilution due to the magnetic field strength variation along a field line in the SOL was significant. The values given in this thesis are upper estimates and are very sensitive to the integration bounds as the magnetic field strength has a toroidal periodicity. Furthermore, the dilution is significantly more prominent in the PFR, so this term cannot be ignored and should be investigated further.

Using the parallel electron conduction loss from upstream to target to assess assumptions made in Lengyel's and Feng's model gave incomplete results as it did not capture the loss due to impurity radiation. Therefore the loss from upstream to the target of the total parallel channel was derived for comparison. The results show that the dilution due to the magnetic field strength variation is significant. Furthermore, the cross-field term is observed to be significant of the total loss for $f_{rad} = 0.2$, and dominant for $f_{rad} = 0.8$. The neutral loss due to electron impact is significant and decreases for $f_{rad} = 0.8$, which is consistent with the results using the loss from the parallel electron conduction channel. The impurity loss is better captured, but it still does not tend to dominate the losses as we would expect for $f_{rad} = 0.8$. Thus, the results presented in this thesis imply that the framework used to analyse the energy transport is not optimal for impurity radiation scaling. However, it enabled identifying the driving transport mechanisms in the SOL, which determined the valid assumptions imposed in the energy transport model.

Preface

This master's thesis presents a new framework for validating assumptions imposed in simplified models for energy transport in the stellarator island divertor scrape-off layer. It represents 26 weeks of work and was carried out during the spring semester partially at EPFL, SPC in Lausanne, and partially at the Max Planck institute for plasma physics in Greifswald, supervised by Dr. Felix Reimold and co-supervised by Dr. Holger Reimerdes (SPC, EPFL) and Assoc. Prof. Jon Andreas Støvneng (NTNU). This master's thesis was a continuation of a semester project on impurity radiation scaling carried out during the fall of 2021.

I am truly grateful for all the help I got from all my supervisors. First, I must thank Dr. Felix Reimold for giving me the opportunity of doing this thesis as a continuation of a semester project and a summer internship. I have grown through our collaboration, and I feel lucky to have been a part of an elite research institute such as the MPIPP. I have enjoyed my time at IPP in Greifswald, both professionally and socially. I also want to thank Dr. Winters, Dr. Bold, Dr. Heinke, Dr. Boeyaert, Małgorzata Jabłczyńska and Dr. Feng for insightful discussions and answering crucial questions. I am indebted to Dr. Holger Reimerdes at SPC. He enabled me to combine an external master's with an exchange to EPFL when he accepted to supervise my master's thesis without prior knowledge of the complicated setup. The inclusive culture at SPC is something I highly appreciate, and I am glad I was a part of the inspiring environment at the institute. At NTNU, I have to thank Assoc. Prof. Jon Andreas Støvneng and Brit Wenche Meland for their support and critical help in solving administrative problems that come with an external master. Lastly, I sincerely thank my friends and family in Oslo, Bodø, Trondheim, Greifswald and Lausanne for their support and collaboration throughout my studies.

Johan Fredrik Agerup
Oslo, Norway
August, 2022

Table of Contents

List of Figures

List of Tables

1 Introduction

This section explains the conditions for fusion reactions and how to maintain continuous reactions in magnetic confinement fusion devices focusing on the W7-X stellarator. Furthermore, the problem of heat exhaust and concentrated heat loads on the plasma-facing components (PFCs) will be introduced and put in perspective the energy transport in the edge of the stellarator. The energy transport in the edge is coupled with energy loss mechanisms where the most considerable contribution to the loss is due to impurity radiation. Therefore, one would want to know how the total radiated power scales with the density controlled by fueling, the temperature controlled by heating, and the impurity fraction $f_Z = n_Z/n_e$ controlled by impurity injection/seeding. Simplified models are often used to obtain such a scaling as previously proposed by Lengyel et al. (1981), Post et al. (1995), Stangeby et al. (2000), and Feng et al. (2006) [6, 7, 8, 4]. The Lengyel model is widely used for radiation scaling in magnetic confinement fusion. Although, the assumptions of the model do not necessarily hold for edge transport in the stellarator because energy transport across the magnetic field, excluded in the Lengyel model, is significant due to the transport properties that follow from the magnetic field configuration. However, Feng has developed a stellarator-relevant version of Lengyel's model where cross-field energy transport is considered. *This thesis reviewed the assumptions imposed in the Lengyel model and its stellarator-relevant version to clarify the validity of the models based on EMC3-EIRENE modeling of the scrape-off layer of W7-X.*

1.1 The fusion reaction

In a fusion reaction, two nuclei collide with sufficient kinetic energy to overcome the Coulomb barrier such that the strong nuclear force can become dominant. The collision eventually results in the two nuclei creating a heavier nucleus [9]. The probability of a fusion reaction occurring depends on the relative velocity of the colliding particles and will be discussed in one of the following subsections. Relevant velocities for fusion reactions correspond to temperatures around $\sim 10 - 100$ keV.

Due to the high temperature required for fusion reactions, neutral atoms are ionized into a plasma. A plasma is an ensemble of charged particles that is globally neutral but locally charged. This property is called quasi-neutrality and is a consequence of the dominant electric force between the ions and electrons whose range is characterized by the Debye length $\lambda_D = \left(e^2 n/\epsilon_0 T_e + e^2 n/\epsilon_0 T_i\right)^{-1/2}$ [9] where $n = n_e = n_i$ is the plasma density assuming quasi-neutrality, e the electron charge, and T_e and T_i is the electron and ion temperature, respectively. Any deviation from neutrality on scales larger than λ_D will be counteracted by the resulting electric interactions between the particles (shielding). The plasma behaves collectively if enough particles are within a Debye sphere $N_D = 4\pi\lambda_D^3 n_0/3$, a sphere with a radius equal to the Debye length λ_D, and the plasma dimension is much larger than the Debye length $L_{\text{plasma}} \gg \lambda_D$. Thus, the plasma can be described as a fluid assuming that collisionality is strong in the SOL, which in this thesis will be used to describe the energy transport of the plasma [8].

The prime candidate for a fusion reaction to be used in magnetically confined fusion is the deuterium-tritium (D-T) reaction, as it has the highest reaction rate at comparably low T_i [9]. The D-T reaction is given by the equation:

$$ {}^2_1\text{D} + {}^3_1\text{T} \longrightarrow {}^4_2\text{He (3.5 MeV)} + {}^1_0\text{n (14.1 MeV)}, \tag{1} $$
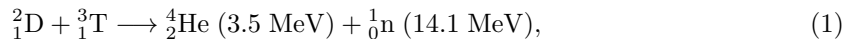
describing a collision between the hydrogen isotopes deuterium and tritium which produces an alpha particle ${}^4_2\text{He}$ and a neutron ${}^1_0\text{n}$ with kinetic energies 3.5MeV and 14.1MeV, respectively.

1.2 Nuclear fusion and power generation

The energy released in a nuclear fusion reaction results from the mass difference between the reactants and the products. The energy released can be directly computed by Einstein's famous

formula stating the relation between energy and mass:

$$\Delta E = \Delta m c^2. \tag{2}$$
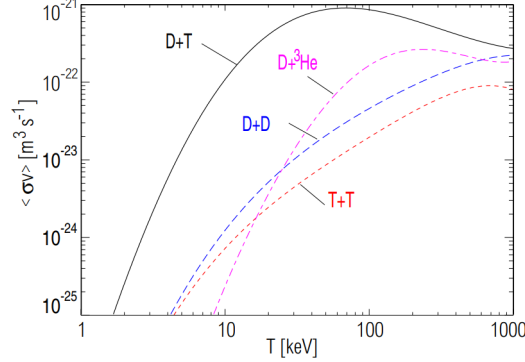
Figure 1: The Maxwellian average reaction rate $\langle \sigma v \rangle$ for some fusion reactions. The D-T reaction rate is given by the black line. Source: [2].

Thus, the D-T reaction produces the energy $\Delta E = (m_\alpha + m_n - m_D - m_T)c^2 \approx 17.6\text{MeV}$ per reaction [9]. To give an impression of the scale of the fusion power, one can compute the number of fusion reactions per second and unit volume and integrate to get the extensive measure of energy production in a fusion reactor. For the D-T reaction in a confined plasma, this is given by:

$$\frac{\# \text{ fusion reactions}}{\text{unit volume} \times \text{unit time}} = n_D n_T \langle \sigma_{DT} v \rangle_{f_{\text{Maxwellian}}} \tag{3}$$

where v is the relative velocity between the colliding particles, n_D and n_T are the deuterium and tritium density using the subscript D and T, respectively. The D-T collisional cross-section σ_{DT} is averaged over a Maxwellian particle distribution $f_{\text{Maxwellian}}$ indicated by $\langle \cdot \rangle_{f_{\text{Maxwellian}}}$ and represents the probability of a collision. The collisional cross-section depends on the colliding ions' relative velocity[9, 10].

Using Eq. 3 the fusion power density can be expressed as:

$$p_f = n_D n_T \langle \sigma_{DT}(v) v \rangle_v \Delta E_f. \tag{4}$$

Furthermore, assuming a 50/50% mix of D-T fuel, giving $n_D = n_T = \frac{1}{2} n_e$ and the effective ionic charge $Z_{eff} = 1$ meaning a plasma without impurities, Eq. 4 gives an expression for the fusion power density:

$$p_f = \frac{1}{4} n_e^2 \langle \sigma_{DT} v \rangle \Delta E_f. \tag{5}$$

The simplified total power balance [9] for the plasma can be expressed as:

$$Q_\alpha + Q_h = Q_B + Q_T \tag{6}$$

where α-heating $Q_\alpha = (\Delta E_\alpha / \Delta E_f) P_f = P_f/5$, Q_h is the heating power, Q_B is the energy loss due to bremsstrahlung and radiation from high Z materials if impurities are present, and Q_T is the energy loss due to transport often parametrized by the energy confinement time τ_E. The neutron power loss $P_n = (\Delta E_n / \Delta E_f) P_f = 4P_f/5$ was ignored in Eq. 6 because the neutrons are not confined and do not contribute to the power balance within the plasma [9].

Inserting power plant relevant values such as electron density $n_e = 10^{20}\text{m}^{-3}$, a plasma volume of $V_p \sim 500\text{m}^3$ and maximum reaction rate $\langle \sigma_{DT} v \rangle = 10^{-21}\text{m}^3\text{s}^{-1}$ gives a fusion power and power

entering the scrape-off layer (SOL) P_{SOL} at [11, 12]:

$$P_f \approx \frac{1}{4}(10^{20})^2\text{m}^{-6} \times 500\textbf{m}^3 \times 10^{-21}\text{m}^3\text{s}^{-1} \times 17.6 \times 10^6 \times 1.6 \times 10^{-19}\text{J} = 5\text{GW}$$

$$P_{\text{SOL}} \approx Q_\alpha = \frac{1}{5}P_f \sim 1\text{GW}, \tag{7}$$

where it is assumed that power is lost at the entrance of the SOL due to cross-field transport and that the radiation loss in the core is equal to the heating power $Q_B = Q_h$. The divertor targets have a total surface A_t on the order of $100\ \text{m}^2$, so the target plates must withstand a homogeneously distributed heat flux density around $10\ \text{MWm}^{-2}$ [13]. The heat flux in magnetic confinement fusion devices is not homogeneously distributed. So some regions on the target will have heat flux densities exceeding $10\ \text{MWm}^{-2}$. Thus, it is key not only to reduce the total target heat load but also to dissipate the power that enters the SOL to homogenize the heat flux distribution [11, 13].

1.2.1   Magnetic confinement fusion

The thermal energy needed for fusion reactions leads to the challenge of plasma confinement: the thermal pressure of the plasma must be counteracted to prevent expansion. One way to address this problem is to embed the plasma in a magnetic field with a shape that allows the field to function as a cage for the plasma. The consequence of the plasma being locally charged is that the particles gyrate around magnetic field lines due to the Lorentz force. The desired effect of the magnetic field is that the direction of the Lorentz force on the particles opposes the expanding force of the thermal pressure of the plasma.
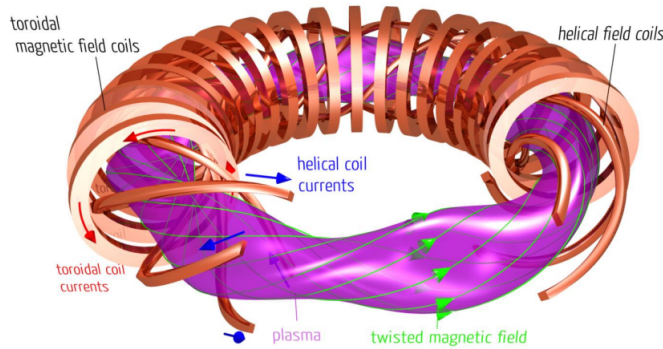
Figure 2: The classical stellarator depicted with the copper coloured magnetic coils, toroidal coil current in red and helical coil currents in blue. The resulting helical magnetic field is indicated by the green arrows twisting around the plasma in purple. Source: [3], originally C. Brandt IPP.

Thus, confining the plasma is achieved if the shape of the magnetic field is helical, as seen in Fig. 2, which depicts a classical stellarator. The helical shape of the magnetic field in the classic stellarator is achieved from a combination of the magnetic field induced by currents in helical and toroidal coils, as shown in Fig. 2. The helical shape of the field, as opposed to a purely toroidal field, prevents charge separation originating from the curvature and the ∇B-drift by averaging out the vertical ∇B and curvature drifts as particles can move freely along the field line [9]. If charge separation takes place, it will create an electric field, and the presence of both an electric and a magnetic field results in $\boldsymbol{E} \times \boldsymbol{B}$-drifts which pushes the plasma radially out from the centre of the torus, breaking confinement [9, 14]. Thus, since a helical field prevents charge accumulation, no $\boldsymbol{E} \times \boldsymbol{B}$-drifts will occur.
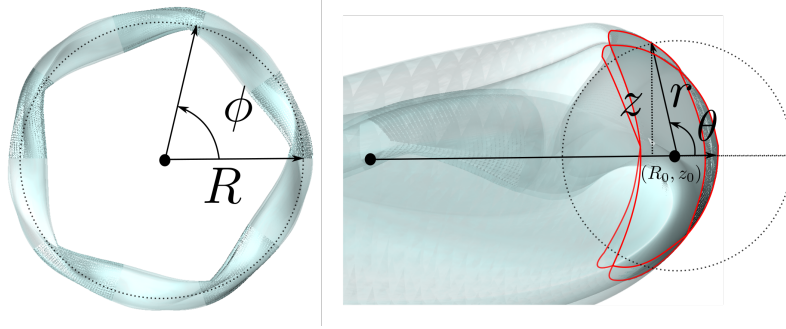
Figure 3: Illustration of the toroidal and cylindrical coordinates system using the separatrix of W7-X in the standard configuration as a reference. The separatrix has been outlined in red in the right figure. The black dot in the left illustration and left side of the right illustration represents z-axis and the origin, respectively, of the cylindrical coordinate system. The horizontal line going from the origin of the cylindrical system to the black dot within the separatrix represents the midplane $z_0 = 0$. The black dot within the separatrix in the right illustration represents the ϕ-axis of the toroidal coordinate system at major radius R_0 and midplane. The dashed circles represent the radius contour of the major radius (ϕ-axis) in the cylindrical coordinate system in the left illustration and the radius contour in the toroidal coordinate system in the right illustration.

Since magnetic confinement fusion devices usually have the same topology as a torus, it is common to describe the device using cylindrical and toroidal coordinate systems. The cylindrical coordinate system is best explained by viewing the torus from above, as in the left illustration of Fig. 3. The radius R goes radially out from the origin of the torus, the vertical distance from the midplane is z and the toroidal angle ϕ. The poloidal cross sections at $\phi = 0°, 12°, 36°$ is shown in Fig. 4 where the horizontal axis is represented by R and the vertical axis is represented by z. The toroidal coordinates can be related to the cylindrical coordinates:

$$r = \sqrt{(R - R_0)^2 + z^2} \tag{8}$$

$$\theta = \arcsin(z/r) = \arctan(z/[R - R_0]) \tag{9}$$

where r defined in Eq. 8 is the radius in a poloidal cross-section centered at the toroidal axis at the major radius R_0. The poloidal angle θ defined in Eq. 9 is the angle between the position vector and the horizontal midplane in a poloidal cross-section shown in the left illustration of Fig. 3.
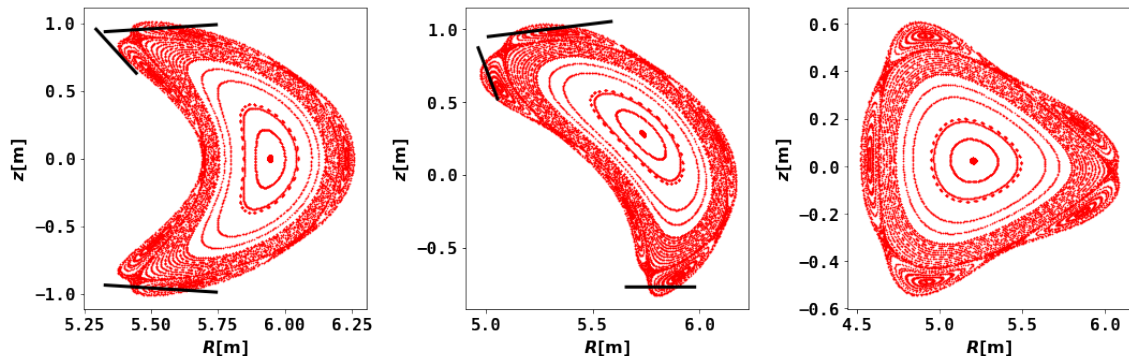
Figure 4: Poincaré plot of the magnetic field (red) with the islands for toroidal angles $\phi = 0°, 12°, 36°$, and target components (black) to illustrate the island divertor in the standard configuration. The horizontal axis represent the major radius R of the torus and the vertical axis the vertical distance z from the midplane.

In most reactors, the magnetic field is generated to intersect with parts of the machine, as illustrated in Fig. 4. The Poincaré plot in red, a concept we will return to in section 2, represents a poloidal cross-section of the magnetic field lines. Each red point represents a magnetic field line intersecting

the Rz-plane. As seen in Fig. 4 the red points map out surfaces in the poloidal cross-section. These surfaces are densely traced out by field lines and close on themselves after a toroidal revolution. They are called *flux surfaces* because the magnetic field flux is constant at the surface for any poloidal and toroidal angle. The field lines in the SOL are intercepted by the divertor target components in black [15]. This magnetic field configuration is one of the heat exhaust solutions in magnetic confinement fusion called a divertor. The name originates from its function: it diverts the particles and heat to the divertor targets specifically made for particle and heat exhaust. Naturally, the targets have a limited maximum heat flux density capacity. The current limit lies at $10\,\mathrm{MWm}^{-2}$ [16, 17, 18]. A viable fusion power plant will have a thermal output of several hundreds of MW and the divertor target surface area on the scale of 10 m [12, 11, 13]. The amount of thermal output required for viable fusion power production and the current limit on the heat flux density capability implies that a significant amount of the heat entering the SOL needs to be dissipated to keep the targets intact for continuous operation [12, 19, 13, 11].

1.3   The island divertor

The island divertor is the version of the divertor used in the W7-X stellarator, which will be described in this subsection. The divertor is characterised by open field lines. Open field lines are called open because they intersect the divertor targets, as seen in Fig. 4, where the divertor targets (black) cut the magnetic islands (red). The confined region is bounded by the last closed flux surface (LCFS) shown as the red surface in Fig. 5 also called the separatrix [8]. The separatrix distinguishes between two regions of different physical behaviour: the confined region and the scrape-off layer (SOL). The power enters the SOL through the LCFS by perpendicular transport and is diverted down to the targets by the field lines in the magnetic islands [20]. Thus, particles and heat that follow open field lines will ultimately end up at one of the targets or the wall components via parallel transport.
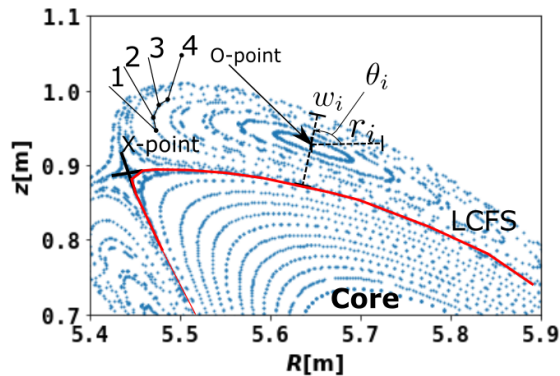
Figure 5: The island at the $\phi = 0°$ poloidal cross-section associated with field lines ending up at the upper horizontal target with the features of the island divertor geometry. The X-point is indicated where the black lines cross between the two islands. The binormal direction is indicated by the direction of the increase in the number of the points 1,2,3 and 4 which represents consecutive transits of the field line around the torus. It is is the poloidal direction in the island reference frame. The island reference frame is centered at the O-point - the center of the island. The radial size of the island is given by r_i and the width w_i, the LCFS is represented by the red line, and the core is the region bounded by the LCFS.

The island divertor (ID) has poloidally and toroidally localized resonances in the magnetic topology due to a perturbation $\delta \boldsymbol{B}$ in the magnetic field $\boldsymbol{B} = \boldsymbol{B}_0(\boldsymbol{x}) + \delta \boldsymbol{B}$, called magnetic islands [21, 15]. The width of the island:

$$w_{i,mn} = 4\sqrt{\frac{R_0 b_{mn}}{m d\iota/dr}} \tag{10}$$

depends on the square-root of the resonant magnetic field component b_{mn}, also referred to as the

Fourier component of the perturbation of the magnetic field [22, 22]. The number of islands is given by the poloidal mode number in the rotational transform ι, which is the number of poloidal transits of a field line for each toroidal transit [23, 21, 24]. Since there are more irrational than rational numbers, ι is usually irrational. The interpretation of an irrational ι means that a magnetic field line does not close on itself but densely traces out a two-dimensional surface [21, 24]. However, it can be divided into a rational and an irrational part [4]:

$$\iota = \frac{n}{m} + r_i \iota' \tag{11}$$

where the fraction n/m indicates the resonance in the magnetic field at which the island chain appears. n represents the toroidal mode number and m the poloidal mode number, r_i is the island radius shown in Fig. 6 and ι' the magnetic shear $d\iota/dr$ describing the degree of rotation of the magnetic field at the n/m-resonance [4, 21]. A rotational transform $\iota = \frac{5}{5}$ indicates that the islands consist of helical flux bundles that circle the torus five times toroidally and poloidally before returning to their starting point. The second term in Eq. 11 represents the internal rotational transform, i.e. the poloidal displacement per toroidal transit in the island reference frame centred at the island O-point. The divertor-relevant field line pitch $\Theta = \Delta x_{\hat{n} \times \hat{b}}/\Delta L_c$, where $\Delta x_{\hat{n} \times \hat{b}}$ is the binormal displacement in the island reference frame and ΔL_c is the arclength of the field line for the toroidal transit corresponding to the the binormal displacement. The binormal direction $\hat{n} \times \hat{b}$ is indicated in Fig. 6. The divertor-relevant field line pitch is an important geometrical quantity because it can be used as a measure of the ratio between parallel and cross-field transport [20, 4].
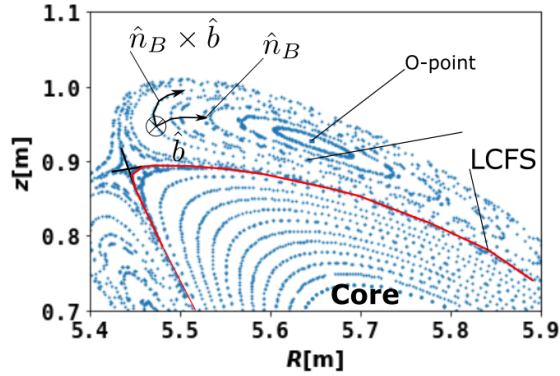
Figure 6: The orthogonal transport directions parallel $\hat{b}$, normal $\hat{n}_B$, and binormal $\hat{n}_B \times \hat{b}$ are indicated in the island reference frame for a poloidal cross-section at $\phi = 0°$.

In W7-X, the ID has three main magnetic configurations: low iota $\left(\frac{5}{6}\right)$, standard $\left(\frac{5}{5}\right)$ and high iota $\left(\frac{5}{4}\right)$, each with slightly different field line pitch varying the footprint of the magnetic field on the target [25]. The W7-X is a five-fold device, as shown from the top view of the separatrix surface shown in Fig. 3, implying that the toroidal mode number $n = 5$ for W7-X. The poloidal mode number m can be chosen freely. This thesis is restricted to the standard $\iota = \frac{5}{5}$ configuration shown in Fig. 7 where the number of islands is determined by the poloidal mode number $m = 5$ as shown in the right plot of Fig. 3. The magnetic field in the standard configuration is used for all the EMC3-EIRENE simulations on which the thesis results are based.
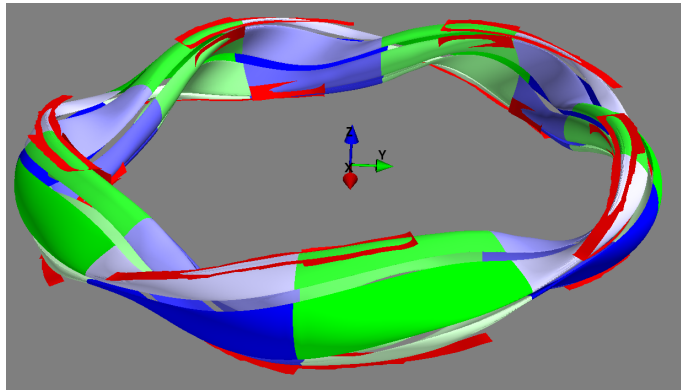
Figure 7: A 3D plot of the magnetic islands and the divertor targets. The islands are indicated in shades of blue and green where blue and green indicate different half modules extending 36° toroidally where the torus consists of 10 half modules put together in up-down symmetric pairs. The different islands are indicated by the strength of the colour, but the particular shade of the colour is not correlated between half modules. The divertor targets are shown in red.

Specific regions in the divertor will be referred to further in the thesis, so some additional definitions are needed. The X-points are defined in axisymmetric devices like the tokamak as the point(s) for which the poloidal component of the magnetic field $B_p = 0$ [9, 24]. However, the definition of the X-points is not so simple for non-axisymmetric devices like the stellarator. However, their locations are illustrated in Fig. 5 and wrap helically around the LCFS [14]. The O-point are the lines that define the centres of the islands and are characterised by infinite connection length because they never intersect the targets [14]. The regions around the O-points are without colour in the insets of Fig. 9 because the connection lengths are above a set threshold of 1km. The topology of the island divertor consists of nested closed magnetic flux surfaces, which are defined in the single-fluid model as isobaric surfaces [9]. This follows from the equilibrium condition $\nabla p = \boldsymbol{j} \times \boldsymbol{B}$ implying $\boldsymbol{B} \cdot \nabla p = 0$. The magnetic islands have closed flux surfaces wrapping helically around the LCFS, as shown in Fig. 7. The region outside the confined region and the islands is called the private flux region (PFR). The PFR is characterised by shorter connection lengths than the SOL and shown in Fig. 9 as the region between the islands outlined in pink in the inset of the first and second plots from the left.
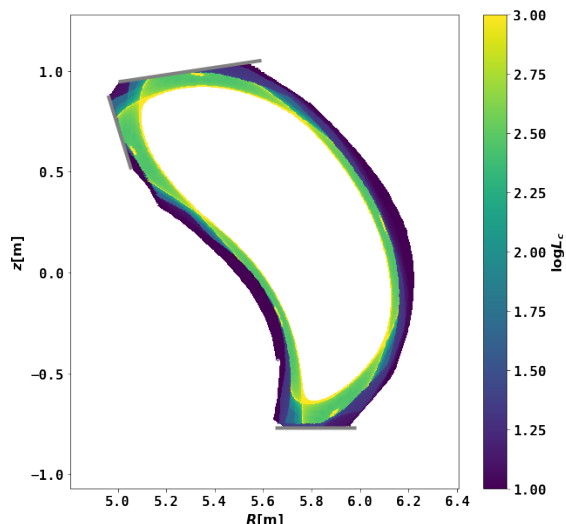
Figure 8: The log-scaled connection length L_c at the poloidal cross-section $\phi = 12°$. The divertor targets are plotted in grey. The values of the colourbar was clipped at 1 and 3.
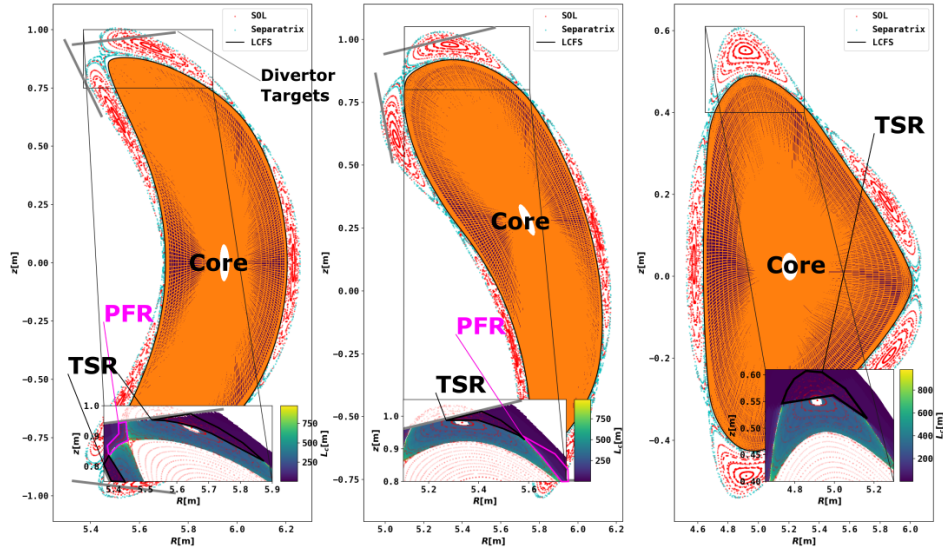
Figure 9: The $\phi = \{0°, 12°, 36°\}$ cross-sections are shown in the left, middle and right plot, respectively. The core region is shown in orange, the LCFS is represented by the black line, the SOL is indicated by the red Poincaré plot, and the separatrix in cyan. The colour scale in the inset indicates the connection length L_c by which the PFR and TSR can be separated from the SOL because they have much smaller connection lengths. All points with $L_c > 10^3$m were removed to obtain a reasonable colour scaling.

The divertor targets in W7-X are toroidally discontinuous as shown in Fig. 7. The region after the field lines intersect the target in the toroidal direction is called the target shadowed region (TSR). A schematic description of the TSR is given in Fig. 10 as the region adjacent to the main transport channel in the SOL. The TSR is visible by the sudden drop in the connection length from the O-point and radially outwards in the inset of the first subfigure from the right in Fig. 9. Even though particles are deposited on the target at the point where the field line and the target intersect due to parallel transport, particles can still enter the TSR by cross-field transport.
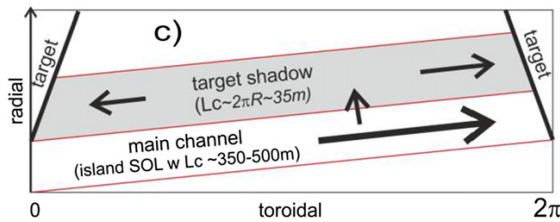
Figure 10: The TSR is illustrated with the SOL and the connection lengths are indicated. The main transport channel in the SOL is depicted in white. The boundary between the SOL, and the TSR starts where the field line intersects the first part of the target in the radial position at $\phi = 0°$ in the left side of the figure. Source: [4].

The PFR and TSR connection lengths, plotted in the insets of Fig. 9 and for a poloidal cross-section at $\phi = 12°$ in Fig. 8, are on the order of $10 - 100$ m and 10 m, respectively. The connection lengths for regions characterised by both parallel and perpendicular transport are typically on the order of $100 - 1000$ m for W7-X [1, 14]. For field lines with short connection lengths, the perpendicular transport, the sources and the sinks are not very efficient because shorter connection lengths imply shorter transport time from upstream to the target. So, for short L_c, the cross-field transport and

the radiation will have little time to dissipate the energy leading to a target heat flux distribution that will have an inverse relation with the L_c footprint. For long L_cs the cross-field transport and radiation loss are more efficient, leaving a target heat flux distribution that tends to be broadened by the effect of cross-field transport and the impurity radiation. In the extreme values of the connection lengths, the parallel (short L_c) or the cross-field (long L_c) can dominate the transport, but for the more general case of intermediate L_cs, parallel and cross-field transport compete. The targets have non-uniform target connection length distribution as seen in Fig. 11, implying a non-uniform distribution of transport properties in the SOL resulting in a heterogeneous target heat flux distribution [25]. Each magnetic field configuration leaves a unique footprint on the targets with a distribution of connection lengths. Thus, the magnetic field configuration gives some degree of control of the transport properties in the SOL.
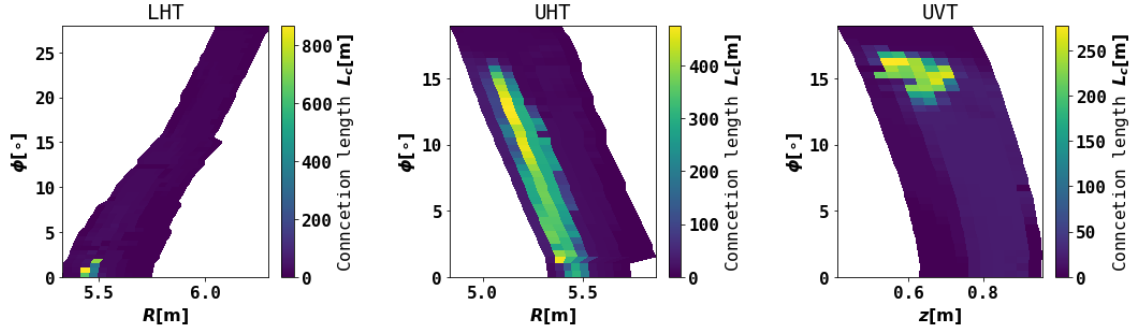
Figure 11: The connection length distribution on the divertor targets. LHT stands for lower horizontal target, UHT the upper horizontal target and UVT the upper vertical target. The horizontal targets are projected in the $R\phi$-plane and the vertical target in the $z\phi$-plane for interpretability.

Furthermore, due to significant target regions with long connection lengths, the discretization of the divertor targets, and the short distance from the plasma to the targets, the cross-field transport is significant in the ID of W7-X [26].

1.4 Target unloading and heat exhaust

The magnitude and the heterogeneity of the target heat flux density indicate that further total and local reduction is needed to handle higher powers required for viable fusion energy production [11, 13]. Furthermore, the complicated geometry of the ID in stellarators makes the 3D treatment of heat transport inevitable. One of the main problems in fusion research is that the heat is not homogeneously distributed at the targets [16, 27, 11, 13]. Thus, the target heat load distribution must be treated in 2D, where the peaks of the heat loads are of greatest concern because the divertor targets have limited heat flux density tolerance [17]. Therefore, it is essential to identify the underlying transport mechanisms that cause these hot spots. What appears to be the driving physics behind the target heat flux might be different for the hot spots. So, focusing on the energy transport mechanisms that determine the hot spots might lead to the discovery of a simplification of the physics model that analysing the total target heat load would not.

1.4.1 Exploiting radiation for cooling the plasma

Radiation is an important part of the heat exhaust because if it is well distributed in the ID, it can be used to homogeneously reduce the target heat loads. The radiation loss can facilitate higher input powers and reduce the degree of maintenance by thermal unloading of the PFCs [11, 13]. The SOL impurity radiation, meaning radiation from particle species different to that of the plasma fuel, is considered the dominant dissipation mechanism in the global energy balance. Impurity radiation occurs due to the excitation or de-excitation of bound electrons via collisions between electrons and heavier ions or neutrals or due to acceleration of electrons in the ion potential (bremsstrahlung). Collisional radiation dominates in the SOL because bremsstrahlung is only significant at high

electron temperature and for high Z impurities, i.e., on the same temperature scale as the core [2]. Impurity radiation is exploited to dissipate heat in the SOL and PFR instead of depositing the heat onto the targets via the electron and ion fluxes. Radiation can be set to a certain level by injecting impurities into the plasma. However, impurities are also unavoidably introduced from the PFCs through erosion, and sputtering [17, 8]. Therefore, spreading heat through impurity radiation is always accompanied by negative effects such as dilution of the plasma or excessive radiation in the core, jeopardising the fusion power output from the core. For high radiative power fraction $f_{\mathrm{rad}} = P_{\mathrm{rad}}/P_{\mathrm{SOL}}$ the radiation layer tends to move inwards from the targets towards the core as shown in Fig. 12. The degree of inward movement of the radiation layer depends on the charge state Z. Higher Z impurities ionise at higher electron temperatures and radiate more efficiently at high temperatures than lower Z impurities. This inward movement can lead to a radiation level in the core where the stored energy in the plasma is decreased to a point where it breaks down [1, 2]. So, a scaling law for f_{rad} to be used for machine control needs to be calibrated for such negative effects.
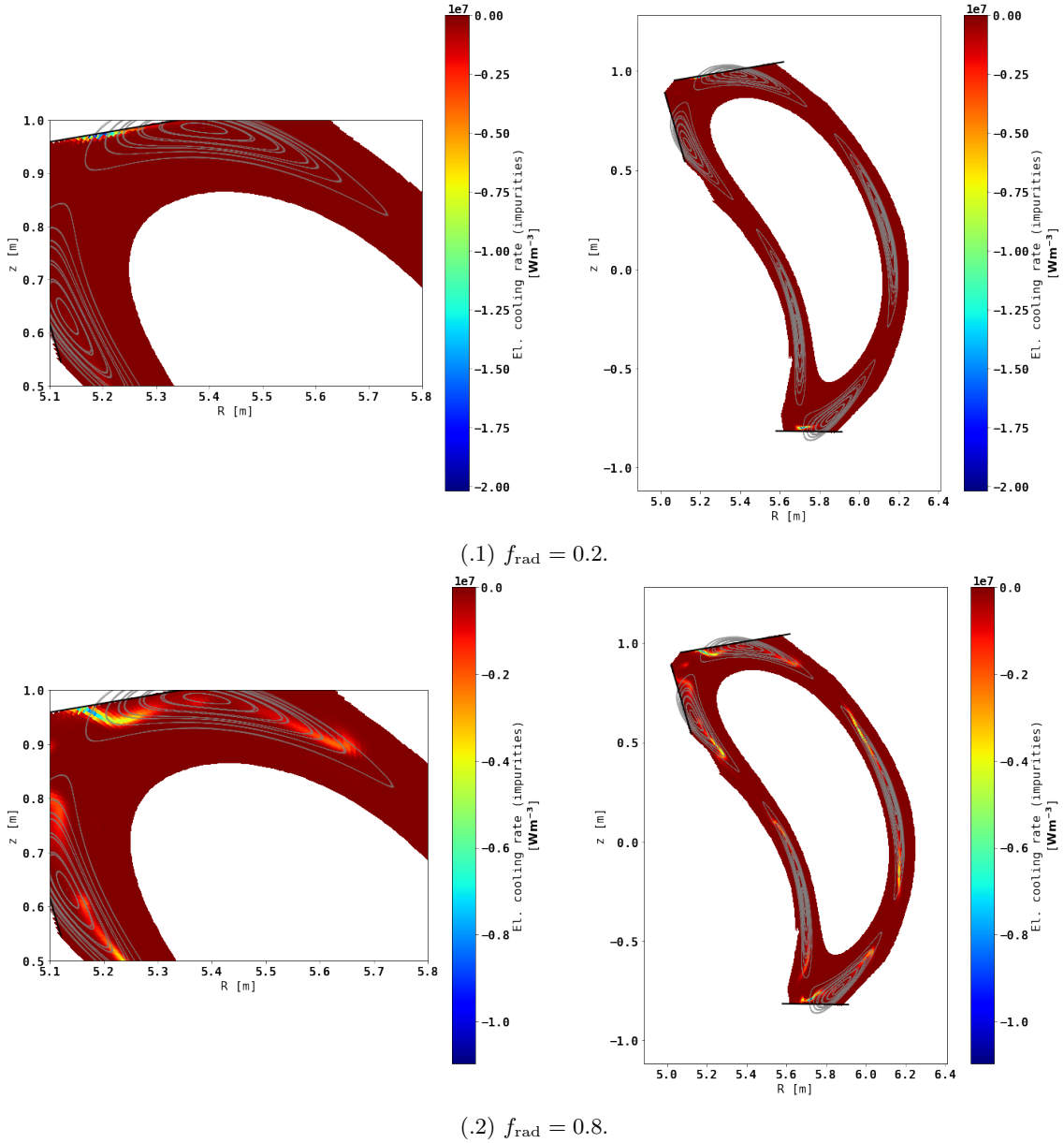
(.1) $f_{\mathrm{rad}} = 0.2$.

(.2) $f_{\mathrm{rad}} = 0.8$.

Figure 12: The radiation distribution of EMC3 simulation where the total radiated power fraction $f_{\mathrm{rad}} = 0.2$ and $f_{\mathrm{rad}} = 0.8$. The left plot zooms in on the upper targets plotted in black. The magnetic islands are indicated by the Poincaré plot in grey. The plot shows inward movement of the radiation front when the radiated power fraction is increased.

The amount of radiation is governed by the *fractional abundances* - the distribution of the charge states of the radiating species and the product between the rate coefficients and the energy released in the atomic processes that cause radiation given by the *photon emission coefficients (PECs)*. The fractional abundances and the distribution of particle species in a fusion reactor are governed by ionisation and recombination processes and transport. The equilibrium of the atomic processes can be described by a collisional radiative model (CRM), stating that the charge states of one impurity species are in local equilibrium [28]. One would want to know the relation between the impurity density and the radiation intensity to control the amount of radiation. The solution of the rate equation in the CRM gives the fractional abundances, the distribution of charge states, for a given electron density and electron temperature. CRM equilibrium is assumed for the equilibrium fractional abundances and is reached when the overall recombination rate balances the overall ionisation rate citepost1977steady, summers2002atomic, summers2006ionization. Summing over the product between photon emission coefficients of transitions from state p to q, $PEC(p,q)$, and the impurity density n_Z gives the radiation intensity:

$$S_{\text{imp}}(n_e, n_Z, T_e, \tau_Z) = \sum_Z \sum_\alpha F_{\alpha Z} \sum_{p,q} PEC_{\alpha Z}(p,q) \times n_e n_{Z_\alpha}$$

$$S_{\text{imp}}(n_e, n_Z, T_e, \tau_Z) = \sum_\alpha L_\alpha(n_e, T_e, \tau_Z) \times n_e^2 c_\alpha \tag{12}$$

at a given density n_e, temperature T_e assuming that the effect of transport on the fractional abundances can be captured by a constant impurity residence time τ_Z [29, 30, 31, 32, 33]. The impurity concentration $c_\alpha \equiv \sum_Z^{Z_0} n_{\alpha Z}/n_e$. In Eq. 12 $F_{\alpha Z}$ is the fractional abundance of impurity species α in charge state Z. The total radiative power is then given by:

$$P_{\text{rad}} = \iiint_{V_{\text{rad}}} S_{\text{imp}} dV, \tag{13}$$

where V_{rad} is the radiative volume.

1.5   Energy transport in the SOL

The divertor-relevant field line pitch Θ is crucial when comparing parallel and cross-field transport in island divertors. For a spatially varying Θ there could be situations where the SOL has different local regimes; one where cross-field transport and parallel transport compete, and another where either dominates. The spatial variation of the transport properties of the SOL is averaged out in global energy analysis. So, a global energy analysis must be seen in the context of the local energy analysis to compensate for the effect that the local transport behaviour will have on the target heat load. Therefore, the global and local energy balance and transport will be presented in this context.

1.5.1   Global energy transport analysis

Global energy balance is obtained by integrating the local energy balance:

$$\nabla \cdot \boldsymbol{q} = S \tag{14}$$

given by the divergence of the heat flux density terms $\nabla \cdot \boldsymbol{q}$ and the sources and sinks S. *Global energy balance and transport refer to the heat flux balance and transport, respectively.* The sources S represent input power, energy loss due to plasma-neutral interaction and energy loss due to impurity radiation. Assuming that the boundary condition at the entrance of the SOL (LCFS) is a constant positive radially oriented flux, the global power balance for the SOL can be written as:

$$\iiint_{r_{\text{sep}}}^{r_t} \nabla \cdot \boldsymbol{q} dV = \iiint_{r_{\text{sep}}}^{r_t} S dV, \tag{15}$$

where r_{sep} is the effective radius at the separatrix, r_t is the effective radius at the target. Note that the integration is performed after mapping nested approximate flux surfaces to nested surfaces at given radii for a toroidal coordinate system shown in Fig. 13. The volume bounded by a surface is an invariant of the mapping as indicated in Fig. 13. The integration requires the flux surfaces in the island divertor to be approximated because the magnetic field structure of the SOL in the ID does not consist of nested surfaces. So, the approximation will be erroneous due to incomplete resolution of the magnetic islands, which themselves are closed flux surfaces. The mapping is a homeomorphism since an approximate flux surface is topologically equivalent to a surface at a given radius in a toroidal coordinates system.
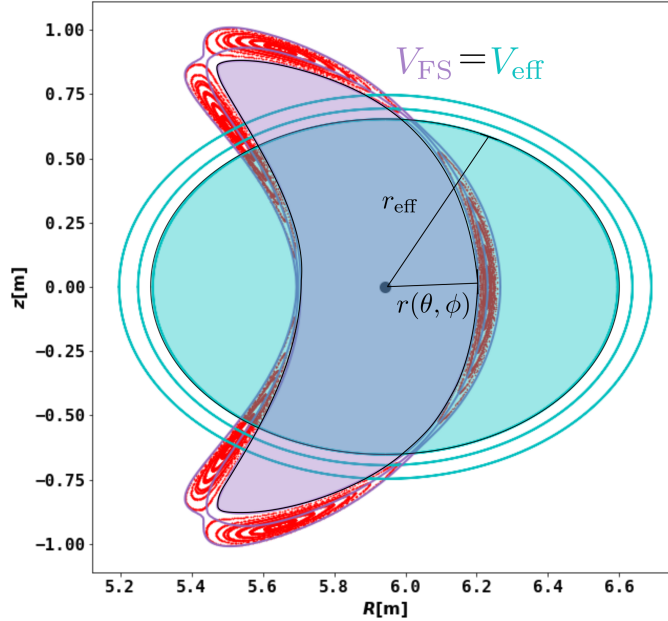
Figure 13: The flux surface approximation and the corresponding surface at a given r_{eff} after the mapping that preserves the volume bounded by the surfaces $V_{\mathrm{FS}} = V_{\mathrm{eff}} = 2\pi^2 R_0 r_{\mathrm{eff}}^2$. Each purple surface represents the approximated nested flux surfaces and their corresponding mapped toroidal surfaces in cyan which is exemplified by the black dotted circle in the right illustration of Fig. 3. The magnetic field is represented by the Poincaré plot in red and shows how the approximate flux surfaces resolves the islands.

The approximation of nested flux surfaces is necessary to define the radial direction consistently. The radial direction can be defined as the vector $\vec{r}_{\mathrm{eff}} \equiv [(\hat{n}_{\mathrm{FS}})_R, (\hat{n}_{\mathrm{FS}})_z, 0]$ in a cylindrical coordinate system which differs from the flux surface normal $\hat{n}_{\mathrm{FS}}$ because it has a zero ϕ-component. The islands are resolved by surfaces shaped such that they resolve the X-points and have a similar shape as the inner or outer separatrix indicated by the innermost and outermost purple surface in Fig. 13.

The integration of the local energy transport is done such that the resulting heat flux goes through a radially oriented surface given by the Green-Gauss theorem:

$$Q(r) = \iiint_{r_{\mathrm{sep}}}^{r} \nabla \cdot \boldsymbol{q} dV = \iint_{S_r} \boldsymbol{q} \cdot d(\boldsymbol{s} \cdot \hat{r}) \tag{16}$$

$$Q_{\mathrm{S}}(r) = \iiint_{r_{\mathrm{sep}}}^{r} (S_{\mathrm{imp}} + S_{\mathrm{neutral}}) dV + Q_t(r) = Q_{\mathrm{imp}}(r) + Q_{\mathrm{neutral}}(r) + Q_t(r), \tag{17}$$

where $Q_t(r)$ is the heat flux lost to the target, $\boldsymbol{s}$ is the surface element associated with the heat flux density vector $\boldsymbol{q}$ oriented in the direction $\hat{s} \perp \hat{q}$. Q_{imp} represents the heat flux due to impurity radiation and Q_{neutral} the heat flux due to interaction with neutral particles (excitation, ionization, recombination, dissociation and charge exchange) [34].

The dot product $\boldsymbol{s} \cdot \hat{r}$ is the radial projection of the surface element $\boldsymbol{s}$. Thus, $S_r = S_r(r, \theta, \phi)$ is the radial projection of a flux surface. Note that the radius at the target varies toroidally as the targets intercept the magnetic field of different radial locations. In a poloidal cross-section, $Q(r)$ represents the amount of heat transported in the direction out of the radially projected flux surface. The field lines in the SOL are open, so both the parallel and the cross-field heat flux densities have components in the radial direction. For any given radius, heat going out of the surface $\boldsymbol{s} \cdot \hat{r}\, Q(r)$ plus the loss from the sinks and gain from the sources Q_S must be equal to the heat flux entering the SOL from the confined region across the separatrix P_{sep}:

$$\iiint_{\boldsymbol{r}_{\text{sep}}}^{r} \nabla \cdot \boldsymbol{q}\, dV = Q(r) - P_{\text{sep}} = Q_S(r) - Q_S(r_{\text{sep}})$$

$$P_{\text{sep}} \equiv \iiint_{0}^{\boldsymbol{r}_{\text{sep}}} \nabla_\perp \cdot \boldsymbol{q} \tag{18}$$

$$P_{\text{sep}} = Q(r) - Q_S(r) \tag{19}$$

assuming that the loss from the sources and sinks in the core $Q_S(r_{\text{sep}})$ is omitted in P_{sep}. The sources and sinks include radiation energy loss, energy loss from plasma-neutral interaction and target heat flux. The transport from the confined region coming from cross-field transport is given by P_{sep}. However, in the SOL field lines are open, thus having a radial component. Consequently, a part of the parallel transport contributes to the heat flux going through the radially oriented surface of the poloidal cross-section. The radial component of the parallel heat flux is substantially smaller than its total magnitude $q_\parallel(\hat{r} \cdot \hat{b}) \ll |\boldsymbol{q}_\parallel|$. Still, it can be large enough to be significant compared to the radial component of the cross-field transport. Therefore, one has to include both terms when obtaining the total heat flux out of a radially oriented surface.

Global energy balance captures the accumulated heat flux at the targets. The target heat flux term included in Q_S in Eq. 19 is obtained by integrating over the surface area of the target. The surface integral puts more weight on areas with smaller heat flux values than the peaks because small heat flux values cover more area. The magnitude of the region of small heat flux can be insignificant concerning the capability of the target material. Consequently, the importance of the localisation of the heat flux is underestimated. The underestimation of the localisation of the heat flux can lead to imprecise conclusions about the driving transport terms regarding the critical spots on the targets. *Thus, the global energy balance analysis to identify the driving physics of the critical regions in the SOL is incomplete and should be additionally analysed in the context of local analysis.*

1.5.2 Local transport

The heat flux density $\boldsymbol{q}$ can be decomposed into a parallel and perpendicular term. The parallel heat flux can be decomposed into a conductive and convective part:

$$\boldsymbol{q}_{\parallel,cond} = \underbrace{-\kappa_{e,0} T_e^{\frac{5}{2}} \nabla_\parallel T_e}_{q_{\parallel,\text{cond},e}} \underbrace{-\kappa_{i,0} T_i^{\frac{5}{2}} \nabla_\parallel T_i}_{q_{\parallel,\text{cond},i}} \tag{20}$$

$$\boldsymbol{q}_{\parallel,\text{conv}} = \underbrace{\frac{5}{2} n T_e v_\parallel \boldsymbol{b}}_{q_{\parallel,\text{conv},e}} + \underbrace{\frac{5}{2} n T_i v_\parallel \boldsymbol{b}}_{q_{\parallel,\text{conv},i}} \tag{21}$$

where quasi-neutrality is assumed in Eq. 21 and $v_\parallel$ is the plasma velocity. The perpendicular transport can be decomposed the same way:

$$\boldsymbol{q}_{\perp,\text{cond}} = \underbrace{-\chi_e n \nabla_\perp T_e}_{q_{\perp,\text{cond},e}} \underbrace{-\chi_i n \nabla_\perp T_i}_{q_{\perp,\text{cond},i}} \tag{22}$$

$$\boldsymbol{q}_{\perp,\text{conv}} = \underbrace{\frac{5}{2} D T_e \nabla_\perp n}_{q_{\perp,\text{conv},e}} + \underbrace{\frac{5}{2} D T_i \nabla_\perp n}_{q_{\perp,\text{conv},i}}. \tag{23}$$

where the cross-field diffusion and energy transport coefficients D and χ, respectively, represents the cross-field anomalous transport characterised by turbulence [35, 36, 37]. The cross-field heat flux density:

$$\boldsymbol{q}_\perp = (\hat{n}_{\mathrm{FS}} \cdot \boldsymbol{q})\hat{n}_{\mathrm{FS}} + [(\hat{n}_{\mathrm{FS}} \times \hat{b}) \cdot \boldsymbol{q}](\hat{n}_{\mathrm{FS}} \times \hat{b}), \qquad (24)$$

where it is separated into a normal component $(\hat{n}_{\mathrm{FS}} \cdot \boldsymbol{q})\hat{n}_{\mathrm{FS}}$ and a binormal component $[(\hat{n}_{\mathrm{FS}} \times \hat{b}) \cdot \boldsymbol{q}](\hat{n}_{\mathrm{FS}} \times \hat{b})$. The normal unit vector $\hat{n}_{\mathrm{FS}}$ is defined as the unit vector normal to the flux surfaces and the binormal direction is the cross product between the normal and field aligned unit vectors $\hat{n}_{\mathrm{FS}} \times \boldsymbol{b}$ as shown in Fig. 6.

1.5.3   Description of local energy transport in the ID

The effect of the terms from Eq. 14 from the core to the targets through the SOL will be described in this subsection to facilitate further discussions of energy transport. Since the LCFS and all other flux surfaces interior to the LCFS are parallel to the magnetic field, heat can only be transported across the LCFS through cross-field transport indicated by $\vec{q}_\perp$ from the core in Fig. 14 [20, 26]. Furthermore, the normal heat flux density $\vec{q}_{\hat{n}_{\mathrm{FS}}}$ tends to transport heat towards the O-point from the region of the island adjacent to the O-point. In the same region, the parallel and binormal component tends to smooth the heat toroidally and poloidally, respectively [38, 1]. However, the binormal component tends to shorten the transport path due to the non-zero projection onto a poloidal cross-section. The gradients in the region below the X-point are predominantly in the binormal direction (perpendicular to the target plate) [38]. Thus, the dissipative effect of normal transport, smoothing of plasma parameters by parallel heat conduction and dissipation due to impurity radiation will be reduced if the binormal component is relatively large.
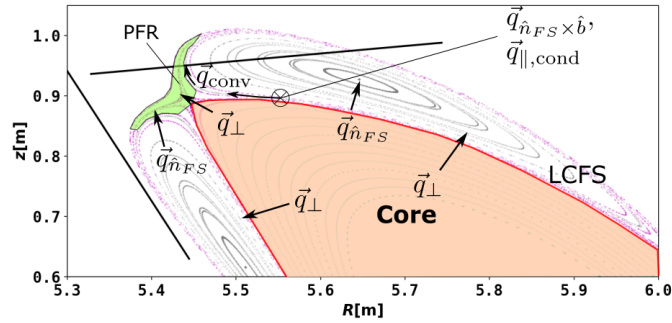
Figure 14: The energy transport is illustrated schematically for the core in pastel orange, the LCFS in red and the PFR in lime green. The heat gets transported from the core to the SOL via cross-field transport $\vec{q}_\perp$ where the parallel and binormal transport $\vec{q}_{\hat{n}_{\mathrm{FS}} \times \hat{b}}$ tends to divert the heat in the binormal direction. Furthermore, the term normal to the flux surfaces $\vec{q}_{\hat{n}_{\mathrm{FS}}}$ will transport heat towards the island O-point. Power enters the PFR at the X-point via the cross-field heat flux $\vec{q}_\perp$ and the normal component $\vec{q}_{\hat{n}_{\mathrm{FS}}}$ below X-point. At the radial distance from the targets where the neutrals ionise, the convective transport becomes important. The increase in convection is indicated by the black arrow going along the poloidal direction of the island flux surface.

At the X-point, the perpendicular heat flux density $\vec{q}_\perp$ can short-circuit the heat transport directly from the core region to the PFR as shown in Fig. 14. Moreover, below the X-point, the normal component of the heat flux density $\vec{q}_{\hat{n}_{\mathrm{FS}}}$ can transport heat from the island to the PFR. The ionisation front of the neutrals is located below the X-point for low radiation scenarios, where power is transferred to the convective term of the heat flux density. The region from the ionisation front to the targets is characterised by relatively low temperatures and thus small temperature gradients. This leaves out transport through conduction as it requires a temperature gradient. Thus, power is transferred from being carried via conductive transport to convective transport $\vec{q}_{\mathrm{conv}}$. The transition from conductive to convective transport needs to be seen in the context of the continuity of ions, as the source of the newly ionised neutrals needs to be balanced out by an

ion flux to the targets. Furthermore, the ions born at the ionisation front are accelerated to ion sound speed at the target as follows from the Bohm boundary condition [8]. This means there is a significant flow of particles allowing for heat to be carried by particles via convection behind the ionisation front to the target.

1.6   Objectives

This thesis will assess the validity of applying simplified models to the energy balance in the ID SOL as a basis for a scaling of the impurity radiation with plasma parameters $(n_e, T_e, P_{\text{Heat}})$ focusing on the Lengyel model and Feng's correction of the Lengyel model for stellarators [6, 4]. In addition, a new framework is suggested to address the challenging task of justifying the assumptions of these models. In this framework, field lines are traced from target to target, which intersects the target at the peaks of the target heat flux distribution. Thus, this selection of field lines is intended to give insight into the driving physics of the energy transport in the ID SOL, which can eventually be used to validate the assumptions made in the simplified models. Ultimately, this will lead to a conclusion about what needs to be included in the SOL energy transport model used to derive a scaling of the radiated power.

1.7   Thesis structure

In Section 2, the CRM will be described in further detail to give a complete picture of the impurity radiation and transport and the related atomic processes. Furthermore, we will present the energy transport in the context of the fluid equations. Moreover, a description of the EMC3-EIRENE code used to simulate the plasma and the plasma-surface interactions (PSI) and the computational methods used in the thesis will be presented.

In section 3, related work is presented to introduce the current state of the energy transport analysis in the SOL for divertors, as well as the simplified models used to derive a scaling of the radiated power. Furthermore, the differences between the framework for energy analysis in this thesis and already established frameworks will be highlighted.

The results will be presented in section 4. First, the global power balance will be presented and compared with previous results. Second, the main results of the thesis will be presented, highlighting the main transport mechanisms through analysis of profiles along field lines and their contribution to the heat flux distribution on the targets. Third, the results will be discussed in terms of assessing the assumptions imposed in the simple models. Ultimately, the predicted impurity concentration needed for a given radiated power fraction will be presented.

In section 5 the conclusion of the discussion of the results will be presented, and an outlook will be given.

2 Theory and methods

This section will first focus on the radiation source as the thesis's main concern is assessing simple energy transport models to be used for scaling the total radiated power. First, the CRM model will be explained and the database used to compute the radiation will be presented. Then, the complete global energy balance will be presented followed by a derivation of the equations for the complete local energy balance. Moreover, the EMC3-EIRENE code and the field line tracer will be described. Last, the two simulation cases representing a low and high radiation scenario will be presented with boundary conditions and all the relevant transport parameters.

2.1 Collisional Radiative Model

As the power loss due to impurity radiation is the main focus points of this thesis, a more detailed description of its physics is presented. The impurity radiation in this thesis is modeled using a collisional radiative model (CRM), introduced in section 1. The CRM was first introduced by Bates et al. and describes the population dynamics of an ion based on collisional theory [39]. This subsection aims to explain what causes the ionisation distribution, how it is affected by the transport in the plasma and the resulting radiation distribution. In the CRM in equilibrium the following assumptions are made about the plasma ([28]):

1. The plasma is optically thin meaning all the photons emitted by ions in the plasma leaves the plasma without being absorbed.

2. The plasma is isotropic, so transport is irrelevant because there are no gradients. The isotropy of the plasma implies that emitted photons are unpolarized and the angular intensity is isotropically distributed.

The observed line-intensity $\Phi(p,q)$[W] for excitation of lower-lying state q to higher-lying state p is given by the lower-level population $n(p)$ and the radiative transition probability $\mathcal{F}(p,q)$:

$$\Phi(p,q) = \underbrace{n(p)\mathcal{F}(p,q)}_{PEC_{p,q}} h\nu V \tag{25}$$

where V is the volume of the radiating plasma and $PEC_{p,q} = n(p)\mathcal{F}(p,q)$ is the photon emission coefficient for the transition from p to q. To compute the line-intensity the population $n(p)$ in state p must be known. This can be computed using the rate equation which is described in the following subsection.

2.1.1 Atomic processes and the rate equation

In a hot plasma, atoms and ions transition between their quantum states due to radiative and collisional processes. The most important of these are spontaneous radiative transitions induced by electron collisions [28]. The CRM considers only these transitions. All other transition processes are omitted, such as photo-ionisation as an optically thin plasma was assumed and transitions induced by collisions with ions. The transitions considered in the rate equation are given in Fig. 15. The relevant transition coefficients due to electron impact are computed by integrating the product of the cross-section and the energy distribution of the incoming electron(s) [28].

$$q \xrightarrow{A(q,p)[\text{s}^{-1}]} p + h\nu \qquad \text{spontaneous radiative transition}$$

$$p + e \xrightarrow{C(p,q)[\text{m}^3\text{s}^{-1}]} q + e \qquad \text{excitation by electron impact}$$

$$q + e \xrightarrow{F(q,p)[\text{m}^3\text{s}^{-1}]} p + e \qquad \text{deexcitation by electron impact}$$

$$z + e \xrightarrow{\beta(p)[\text{m}^3\text{s}^{-1}]} p + h\nu \qquad \text{radiative recombination}$$

$$p + e \xrightarrow{S(p)[\text{m}^3\text{s}^{-1}]} z + e + e \qquad \text{ionisation by electron impact}$$

$$z + e + e \xrightarrow{\alpha(p)[\text{m}^6\text{s}^{-1}]} p + e \qquad \text{three-body recombination}$$
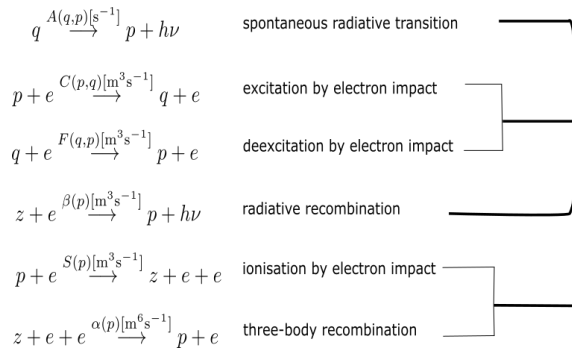
Figure 15: Reaction equations of the transitions included in the rate equation. The thick lines denote transitions which are similar in nature and the thin lines denote inverse processes. The transition coefficients (letters above the arrows) are explained in Table 1. p and q indicate different excited energy states of atoms, the electron charge is given by e, the energy of a photon $h\nu$ with frequency ν, and Z represents an ion in ionisation stage Z.

Einstein's A for transition probability for $q \to p$ and $p \to q$	$A(q,p), A(p,q)$	s^{-1}
Einstein's B for photon absorption and induced emission	$C(q,p), C(p,q)$	m^{3}s^{-1}
Excitation and deexcitation rate coefficients	$\mathcal{F}(q,p), \mathcal{F}(p,q)$	m^{3}s^{-1}
Ionisation rate coefficients	$S(p)$	m^{3}s^{-1}
Three-body recombination rate	$\alpha(p)$	m^{6}s^{-1}
Radiative recombination	$\beta(p)$	m^{3}s^{-1}

Table 1: Transition coefficients and their dimensions.

Spontaneous radiative transition and radiative recombination

Spontaneous radiative transition is where an electron in state $q > p$ spontaneously decays to a lower energy state p emitting a photon with energy $h\nu$ corresponding to the difference between the two energy levels $E(q,p)$. Radiative recombination is a similar process where a ground state ion in ionisation stage Z captures an electron in continuum state q_ϵ having energy ϵ to form an atom in level p in ionisation stage $Z - 1$ by emitting a photon with energy $E(q_\epsilon, p)$ and frequency ν.

Excitation and deexcitation by electron impact

Excitation by electron impact is when an electron collides with an ion in state p which excites the ion to a higher energy state q and the electron is scattered. The projectile electron needs to have a higher energy than the energy gap between the two states, and the likelihood of the collision depends on the velocity of the incoming electron. In the inverse process, de-excitation by electron impact, the energy difference between energy state q and p is converted into kinetic energy of the scattered electron.

Ionisation by electron impact and three-body recombination

Ionisation by electron impact may be regarded as the continuation of the excitation process. In addition to exciting the state p to the highest bound energy level q the electron in this state breaks free from the atom, thus ionising the atom from ionisation stage $Z - 1$ to Z. The incoming electron is scattered after the collision. Three-body recombination is the inverse process involving two electrons and an ion. The ion is then recombined from ionisation stage Z to $Z - 1$. The transition processes are given in terms of reaction equations in Fig. 15.

The rate equation

The rate equation describes the change in the population of discrete energy levels accounting for the processes given in table 1. All other transition processes are omitted as assumed for the CRM. The evolution of the population in state p, where $p = 1$ is the ground state, $n_Z(p)$ for each Z is then given by the rate equation:

$$\frac{d}{dt}n_Z(p) = \underbrace{\sum_{q<p} C(q,p)n_e n_Z(q)}_{\text{Excitation flux}}$$

$$- \underbrace{\left[\left\{\sum_{q<p}\mathcal{F}(p,q)n_e + \sum_{q>p}C(p,q) + S(p)\right\}n_e + \sum_{q<p}A(p,q)\right]n_Z(p)}_{\text{Depopulating flux}} \qquad (26)$$

$$+ \underbrace{\sum_{q>p}\left[\mathcal{F}(q,p)n_e + A(q,p)\right]n_Z(q)}_{\text{Flux from higher levels}}$$

$$+ \underbrace{[\alpha(p)n_e + \beta(p)]n_{Z+1}}_{\text{Direct recombination flux}}$$

$$+ \underbrace{S(p)n_e n_{Z-1}}_{\text{Ionisation flux}}$$

where n_e denotes the electron density and n_Z the ion density with nuclear charge Ze. The summation convention is that the summation over $q < p$ is over levels q that lie energetically below level p.

(.1) The rate equation illustrated as a graph where the node $E_{q<p}$ are all the energy levels which are lower than the energy state p in ionisation stage $Z-1$. $E_{q>p}$ is the node denoting the energy levels which are higher than E_p. E_Z represents the ground state energy of the ions.

(.2) Atomic processes illustrated by the transitions between the excited populations p and q for $q > p$. The ground state of the neighbouring ionisation stages $Z-1$ and Z are represented as the lower and upper slap, respectively. The coefficients associated with the transitional probabilities are $C(p,q)$, $\mathcal{F}(q,p)$, $A(q,p)$, $S(p)$, $\alpha(p)$, $\beta(p)$, and the ionisation potential of state p is $\chi(p)$.

Figure 16: Illustrations of the transitions associated with the rate equation.

The dimensions of the transition coefficients is given in table 1 and the rate equation is illustrated as a graph in Fig. 16.1. The first line in Eq. 26 represents the excitation flux from lower lying levels q into level p and the second line the flux population out of level p. The third line is the populating flux into level p from higher lying levels and the last line represents populating influx due to direct recombination. It is important to note that Eq. 26 is coupled with similar equations for other excited levels, an the neighbouring charge states n_{Z-1} and n_{Z+1} via recombination. In the SOL the validity of the first assumption in the CRM is questionable considering that the density conditions can change significantly due to plasma-neutral interaction being highly localised [20, 1]. The second assumption follows the same argument. Globally the ion transport might be small, but in regions close to the targets it can be relatively large. The couplings between the neighbouring charge states are generally not in an equilibrium due to transport in an inhomogeneous plasma. Therefore, the results using atomic data based on the rate equation must be seen in context of

these assumptions. However, the equation can be simplified by assuming a *quasi stationary-state* which will be described in the following subsection.

2.1.2 Quasi steady-state

In reality the system described by the rate equation has a relaxation time to a steady-state solution. However, if the ground state density $n(1)$ or the plasma undergoes a rapid change in the electron density n_e and temperature T_e the ground and *metastable* states do not have enough time to relax to equilibrium. In realistic situations for magnetic confinement fusion it is expected that at a certain time the excited-level populations have already reached their steady-state values given by the ground-state density $n_Z(1)$, T_e and n_e at that time. Hence, the excited-level populations are defined by an impurity density n_Z, electron density n_e and electron temperature T_e. The timescales of the metastable and the ground state populations are comparable to the plasma ion diffusion across temperature or density scale lengths, relaxation times of transient phenomena and observation times $\tau_{\text{rec}}, \tau_{\text{ion}} \sim \tau_{\text{transport}}$ [32]. Thus, the metastable and the ground state populations evolve in order of the timescale of the plasma dynamics and should be modeled explicitly. The excited states of impurities may assumed to be relaxed with respect to the instantaneous metastable and grounds state populations and thus are said to be in a quasi steady-state (QSS) as the equilibration times are shorter than $\tau_{\text{transport}}$. In the QSS the time derivative of the excited-level populations is therefore approximated as being zero:

$$\frac{dn(p)}{dt} = 0 \ \ for \ p = 2, 3, \ldots \tag{27}$$

The time derivatives of the ground-state populations $n_Z(1)$, $n_{Z-1}(1)$ and $n_{Z+1}(1)$ are kept non-zero. The formulation splits up the system in two parts: the excited-state population, and the ground-state population and ion density. Thus, Eq. 27 can be expressed in a set of linear equations on matrix form:

$$\begin{pmatrix} \cdot & \cdot & \cdot & \cdot \\ \cdot & \cdot & \cdot & \cdot \\ \cdot & \cdot & \cdot & \cdot \\ \cdot & \cdot & \cdot & \cdot \end{pmatrix} \begin{pmatrix} n(2) \\ \cdot \\ n(p) \\ \cdot \end{pmatrix} = \begin{pmatrix} \cdot \\ \cdot \\ \cdot \\ \cdot \end{pmatrix} n_Z(1) + \begin{pmatrix} \cdot \\ \cdot \\ \cdot \\ \cdot \end{pmatrix} n_{Z+1} + \begin{pmatrix} \cdot \\ \cdot \\ \cdot \\ \cdot \end{pmatrix} n_{Z-1} \tag{28}$$

where the elements of the square matrix on the LHS and the column matrices on the RHS are terms of the RHS of Eq. 26. These terms are functions of the electron temperature T_e, via the collisional rate coefficients, and electron density n_e [28, 32]. The imply that we can get the photon emission coefficients for transitions between level p and q $PEC_{p,q} = n(p)\mathcal{F}(p, q)$.

Once the ionisation has been solved, one can obtain the normalised fraction of the ionisation stages compared to the initial atom density before ionisation at given plasma conditions. This quantity is called the *fractional abundances* and is given by:

$$F_{\alpha_Z} = \frac{n_{\alpha_Z}}{n_{\alpha_0}}; \quad Z = 1, \ldots Z_0 \tag{29}$$

where Z indicates the ionisation stage of the ion of species α and n_{α_0} is the neutral impurity density. The equilibrium radiated power loss function can be obtained by combining the expression of the fractional abundances and the power coefficients associated with overall excitation and recombination. The following subsection will explain how these coefficients and the power loss function are obtained.

2.1.3 Atomic data and analysis structure

OPEN-ADAS (Atomic Data and Analysis Structure) is an atomic database which can be used to compute the radiated power loss from impurities in plasmas [32]. The data from ADAS is used to obtain both the ionisation distribution and the radiative power loss for given plasma

conditions. The following assumptions are made for the radiative power loss, which in thesis will be approximated by what is referred to as the electron energy loss in Summers et al. (2006) [32]:

1. Ground states of ions and metastable states have long lifetimes compared to other excited states. Thus the excited state population is in QSS.

2. The transition between meta-stables are negligible. We use data where metastables are only ground states, i.e. we simulate full ion charge states only.

The ADF11 iso-nuclear master files include the overall ionisation and recombination, and the line power coefficients following the abovementioned assumptions. This thesis uses these files to compute the impurity radiation in the EMC3-EIRENE simulations. The temperature dependence of the coefficients used in this computation is shown for equilibrium in Fig. 17. The solution of Eq. 28 gives the ionisation distribution in quasi-steady state. Now assuming that the only metastables present are the ground states of ions the LHS of Eq. 28 is zero and the overall recombination and ionisation coefficients are found by solving the following set of equations:

$$\dot{n}_Z = -S_Z n_Z + \alpha n_e n_{Z+1} + \beta n_{Z+1} + S_{Z-1} n_{Z-1} \tag{30}$$

for which the equilibrium is:

$$\dot{n}_Z = 0 = \begin{pmatrix} -S_0 & \alpha_1 n_e + \beta_1 & 0 & \cdots \\ S_0 & -S_1 & \alpha_2 n_e + \beta_2 & \cdots \\ \vdots & \ddots & \ddots & \end{pmatrix} \begin{pmatrix} n_0 \\ n_1 \\ \vdots \\ n_Z \end{pmatrix} \tag{31}$$

where the overall recombination rate coefficient ACD is given by:

$$ACD \equiv \alpha n_e + \beta \tag{32}$$

and the overall ionisation rate coefficient SCD is:

$$SCD \equiv S \tag{33}$$

where the symbols on the RHS of Eqs. 32 and 33 are described in Tab. 1. CD indicates that the CRM includes dielectronic recombination for both coefficients [31].

PLT is the line power coefficient for line power driven by excitation of ions in the metastable states, given by [32]:

$$PLT_Z = \sum_{p,q} E(p,q) \underbrace{\mathcal{F}(p,q) \mathrm{F}_Z^{\mathrm{exc}}(p)}_{PEC^{\mathrm{exc}}}. \tag{34}$$

The sum in Eq. 34 is taken over the transitions of the ion in stage Z from $p \rightarrow q$ where $\mathcal{F}(p,q)\mathrm{F}_Z^{\mathrm{exc}}(p)$ is the excitation photon emissivity coefficient for this transition [32]. The energy difference between the two states p and q is given by $E(p,q)$. The recombination-bremsstrahlung power coefficient PRB is based on line power driven by recombination and bremsstrahlung of dominant ions:

$$PRB_{Z+1} = \sum_{p,q} E(p,q) \underbrace{\mathcal{F}(p,q) \mathrm{F}_{Z+1}^{\mathrm{rec}}(p)}_{PEC^{\mathrm{rec}}}, \tag{35}$$

where $\mathcal{F}(p,q)\mathrm{F}_Z^{\mathrm{rec}}(p)$ is the recombination photon emissivity coefficient [32]. $\mathrm{F}_Z^{\mathrm{exc}}(p)$ and $\mathrm{F}_Z^{\mathrm{rec}}(p)$ are the effective contributions to the fractional abundances from excited populations of metastables and free electron capture by higher-lying metastable states [31]. However, since this thesis only concerns the ground states $p = 1$ the coefficients reduces to:

$$PLT_Z = \sum_q E(1,q)\mathcal{F}(1,q)\mathrm{F}_Z^{\mathrm{exc}}(1) \tag{36}$$

$$PRB_{Z+1} = \sum_q E(1,q)\mathcal{F}(1,q)\mathrm{F}_{Z+1}^{\mathrm{rec}}(1) \tag{37}$$

In the reduced equations, both the excitation and recombination emissivity coefficient are associated with the ground states of the ions in ionisation stage Z and $Z + 1$, respectively.
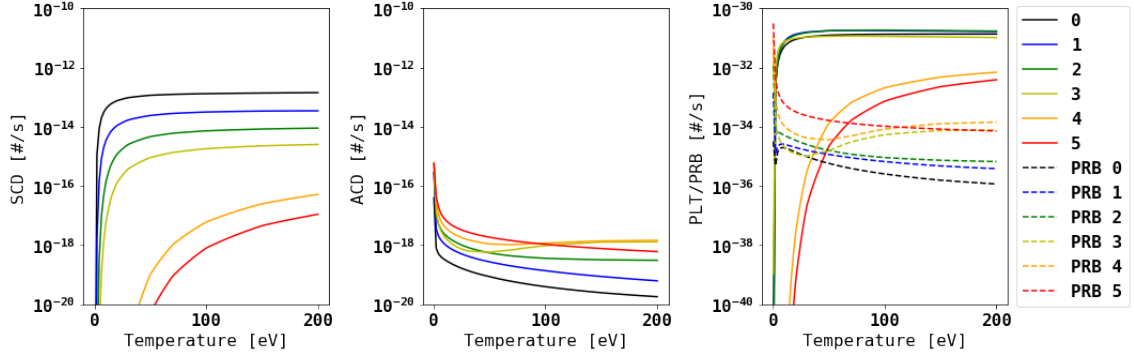
Figure 17: The coefficients used in the computation of the fractional abundances and radiation power loss function in coronal equilibrium is plotted against the electron temperature. From the top left: the effective ionisation coefficient SCD, the effective recombination coefficient ACD and the line power driven by excitation of ions in the ground state PLT and the continuum and line power driven by recombination and bremsstrahlung of ions in the ground state PRB. The rate coefficients SCD and ACD are given in m^3s^{-1} and line power coefficients PLT and PRB are given in Wm^3. Note that for the recombination coefficients 0-5 is the ionisation stages $Z = 1 - 6$.

The impurity model uses the effective recombination (ACD) and ionisation coefficients (SCD) to compute the ionisation distribution for local plasma parameters in CRM equilibrium. However, transport of impurities is included in the EMC3 impurity model which will be discussed in further detail the subsection on EMC3-EIRENE.

2.1.4 Radiated power loss function

Now that the ionisation, recombination and power coefficients have been introduced they will be used to obtain the fractional abundances and the radiated power loss function. The effect of transport assuming a constant residence time τ_Z of the impurities can be assessed with data from ADAS, and will introduced for later discussion in section 4.

(.1) Constant impurity residence time $\tau_Z = 10^{-2}$s.

(.2) Constant impurity residence time $\tau_Z = 10^{-4}$s.
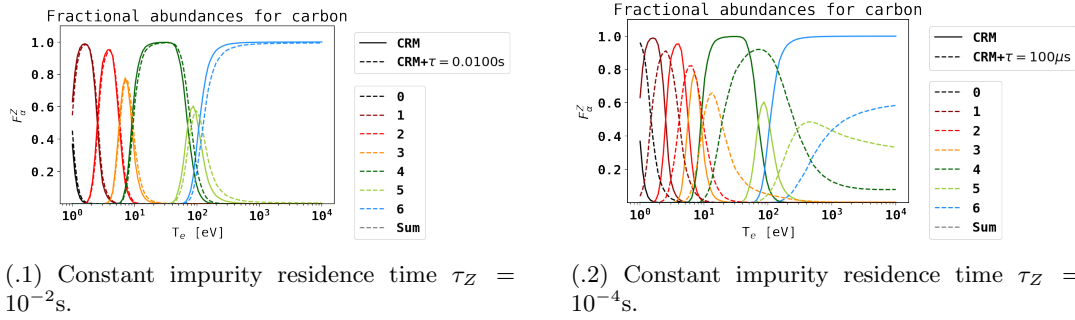
Figure 18: Fractional abundances of carbon against the electron temperature T_e. The lines represent the fractional abundances after relaxation to coronal equilibrium and the dashed lines the fractional abundances where the ionisation distribution is affected by transport assuming a constant impurity residence time τ_Z. The numbers in the legends represent the charge state Z.
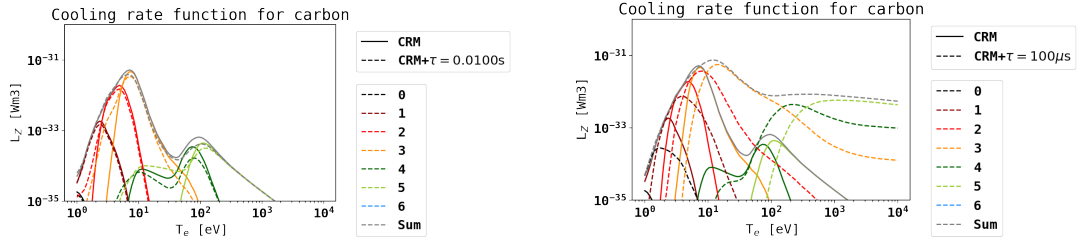
(.1) Constant impurity residence time $\tau_Z = 10^{-2}$s.

(.2) Constant impurity residence time $\tau_Z = 10^{-4}$s.

Figure 19: Radiation power loss function for all ionisation stages of carbon against the electron temperature T_e. The lines represent the radiation power loss functions after relaxation to equilibrium and the dashed lines the radiation power loss function where the ionisation distribution is affected by transport from lower to higher temperature regions assuming a constant impurity residence time τ_Z.

Generally the radiative power loss function L_Z is given by the the product of the equilibrium fractional abundances and sum of the the power coefficients PLT and PRB:

$$L_Z = \sum_{\sigma=0}^{M_Z}(PLT_\sigma^Z + PRB_\sigma^Z)F_{Z,\sigma}^{(\text{equil})} \tag{38}$$

The last term on the RHS of Eq. 38 $F_{Z,\sigma}^{(\text{equil})}$ is the fractional abundances for charge state Z in metastable state σ. The summation over σ up to M_Z refers to the summation over all meta-stables. Due to the plasma conditions in the SOL the recombination and the bremsstrahlung is assumed to be negligible. For carbon, the former can be argued from the temperature dependence of the PRB coefficients in Fig. 17. The PRB's only become significant, when seen in context with the temperature dependent fractional abundances, for temperatures which are mostly outside the SOL range of $10^0 - 10^3$eV. In Fig. 17 the significant coefficients are the ions in the two last ionisation stages for which the fractional abundances in the temperature region of significance ≈ 20eV is zero. Furthermore, the only metastables are assumed to be the ground states. Thus, the expression for the equilibrium radiated power loss function can be simplified to:

$$L_Z = PLT_Z F_{Z,\text{equil}}. \tag{39}$$

The difference in the radiated power loss function in Figs. 19.1 and 19.2 for residence times $\tau_Z = \{10^{-2}\text{s}, 10^{-4}\text{s}\}$, respectively, indicate that shorter residence times tends to broaden the radiation power loss function in the transport direction. The residence time was in these radiated power loss functions related to transport from lower to higher temperature regions. This effect will be discussed further in section 4.

2.2 Local energy balance

The local energy balance is introduced in section 1. It will in this subsection be described in further detail starting from the local energy balance given by Eq. 14. Furthermore, the integral along a field line including almost every term in the energy balance equation will be derived.

Eq. 14 needs to be simplified to decompose the divergence into gradients parallel and perpendicular to the magnetic field. This was done by accounting for the Jacobian $J = 1/B$ in Clebsch coordinates with the contravariant representation of $\boldsymbol{B}$ [24, 23]. For simplicity it is assumed that the variation of the magnetic field perpendicular to the field lines has a negligible effect on the cross-field heat flux density. However, the dilution from flux expansion or contraction of the parallel heat flux due to magnetic field strength variations along the flux tube is accounted for. Thus, the simplified

version of Eq. 14 is:

$$\vec{\nabla} \cdot \boldsymbol{q} = \frac{1}{J} \left[\nabla_{\parallel}(J\hat{b} \cdot \boldsymbol{q}) + \nabla_{\perp}(J\hat{n}_{\perp} \cdot \boldsymbol{q}) \right] = B(\nabla_{\parallel}(q_{\parallel}/B) + \nabla_{\perp}(q_{\perp}/B)) = S \rightarrow$$

$$B\nabla_{\parallel}\left(\frac{q_{\parallel}}{B}\right) + \nabla_{\perp}q_{\perp} = S, \tag{40}$$

where the decomposed operators:

$$\nabla_{\parallel} = (\hat{b} \cdot \nabla)\hat{b}$$
$$\nabla_{\perp} = \nabla - \nabla_{\parallel}$$
$$\hat{b} = \frac{\boldsymbol{B}}{B}.$$

The flux tube cross-sectional area $A_{\perp}$ is proportional to $1/B$ leading to a coupling with the parallel heat flux density as $q_{\parallel} = Q_{\parallel}/A_{\perp}$. The correction of the variation of the magnetic field strength in the direction perpendicular to the flux surfaces would be to include the term $B\nabla_{\perp}\left(\frac{q_{\perp}}{B}\right)$. This term was left out to be solved in the future. The suggested approach to solve for this correction is given in the outlook in section 5.

We can write the first term from the left on the LHS of Eq. 40 is:

$$B\nabla_{\parallel}\left(\frac{q_{\parallel}}{B}\right) = B\frac{B\nabla_{\parallel}q_{\parallel} - q_{\parallel}\nabla_{\parallel}B}{B^2} = \nabla_{\parallel}q_{\parallel} - \frac{q_{\parallel}\nabla_{\parallel}B}{B}. \tag{41}$$

and decompose using $q_{\parallel} = q_{\parallel,\text{cond,e}} + q_{\parallel,\text{cond,i}} + q_{\parallel,\text{conv,e}} + q_{\parallel,\text{conv,i}}$:

$$\nabla_{\parallel}q_{\parallel,\text{cond,e}} = S - \nabla_{\perp}q_{\perp} + \frac{q_{\parallel}\nabla_{\parallel}B}{B} - \nabla_{\parallel}q_{\parallel,\text{conv}} - \nabla_{\parallel}q_{\parallel,\text{cond,i}} \tag{42}$$

$$q_{\parallel,\text{cond,e}} = \kappa_{\parallel 0e}T_e^{5/2}\nabla_{\parallel}T_e. \tag{43}$$

We have chosen $q_{\parallel,\text{cond,e}}$ to be the only term on the LHS, making the analysis comparable to the Lengyel model. The physical interpretation of the Lengyel integral is how much power is lost from the parallel electron conductive channel due to radiation assuming that parallel electron transport is dominant. In the full energy trasnport model, the parallel conductive channels are not dominant. However, if a similar fraction of power is lost from the parallel electron conductive channel due to radiation as from the total power it can still be used to derive a relation between radiation losses and plasma parameters. The integral to be used as a baseline for assessing the assumptions in the Lengyel and Feng models can be derived by combining Eq. 42 and 43.

2.2.1 Derivation of field line integral

Now that the transport mechanisms have been described locally, we will look at the heat transport integrated along a field line. This integral is equivalent to the summed effect of all the contributions of the different energy transport mechanisms along (parallel heat flux density terms) and across (cross-field term, sinks and sources) the magnetic field. By combining Eqs. 42 and 43 the integral

from downstream to upstream can be derived:

$$(\nabla_\| q_{\|,\text{cond,e}})q_{\|,\text{cond,e}} = q_{\|,\text{cond,e}}\Big(S - \nabla_\perp q_\perp + \frac{q_\| \nabla_\| B}{B}$$
$$- \nabla_\| q_{\|,\text{conv}} - \nabla_\| q_{\|,\text{cond,i}}\Big)$$

$$\frac{1}{2}\nabla_\|(q_{\|,\text{cond,e}}^2) =$$
$$\frac{1}{2}\int_t^u \nabla_\|(q_{\|,\text{cond,e}}^2) = \int_t^u q_{\|,\text{cond,e}}\Big(S - \nabla_\perp q_\perp + \frac{q_\| \nabla_\| B}{B}$$
$$- \nabla_\| q_{\|,\text{conv}} - \nabla_\| q_{\|,\text{cond,i}}\Big)dl_\|$$

$$(q_{\|,\text{cond,e,u}}^2 - q_{\|,\text{cond,e,t}}^2)/2 = \int_t^u q_{\|,\text{cond,e}}\Big(S - \nabla_\perp q_\perp + \frac{q_\| \nabla_\| B}{B}$$
$$- \nabla_\| q_{\|,\text{conv}} - \nabla_\| q_{\|,\text{cond,i}}\Big)dl_\| \tag{44}$$

$$S = S_{\text{neutral}} + S_{\text{imp}}, \tag{45}$$

where $L_\alpha = \sum_{Z=1}^{Z_{0,\alpha}}$ which is the radiated power loss function summed over all ionisation stages of species α. The integral in Eq. 44 describes the contributions from every energy transport mechanism along a field line with arclength $l_\|$ from upstream to downstream. The source terms are given in Eq. 45. The power loss due to impurity radiation S_{imp} is assumed to be dominated by a primary radiator of species α. If the system is directly simulated all the quantities in Eq. 44 are available. Thus, the integral can be evaluated for the simulation data, and be used as a baseline for assessing simplifying assumptions. For readability the following definitions are made:

$$I_{\text{neutral}} = \int_t^u q_{\|,\text{cond,e}}S_{\text{neutral}}dl_\| \tag{46}$$

$$I_{\text{imp}} = \int_t^u q_{\|,\text{cond,e}}S_{\text{imp}}dl_\|$$

$$= -\int_t^u q_{\|,\text{cond,e}}n_e^2 c_\alpha L_\alpha dl_\| \tag{47}$$

$$I_\perp = \int_t^u q_{\|,\text{cond,e}}\nabla_\perp q_\perp dl_\| \tag{48}$$

$$I_B = \int_t^u q_{\|,\text{cond,e}}\frac{q_\| \nabla_\| B}{B}dl_\| \tag{49}$$

$$I_{\text{conv}} = \int_t^u q_{\|,\text{cond,e}}\nabla_\| q_{\|,\text{conv}}dl_\| \tag{50}$$

$$I_{\text{cond,i}} = \int_t^u q_{\|,\text{cond,e}}\nabla_\| q_{\|,\text{cond,i}}dl_\| \tag{51}$$

which gives the following compact expression for the integral in Eq. 44:

$$\frac{1}{2}(q_{\|,\text{cond,e,u}}^2 - q_{\|,\text{cond,e,t}}^2) = I_{\text{imp}} + I_{\text{neutral}} - I_\perp + I_B - I_{\text{conv}} - I_{\text{cond,i}}. \tag{52}$$

Eq. 52 is the complete picture of the power transferred from the parallel conductive heat flux density channel from upstream to downstream due to the transport mechanism on the RHS. The contribution of each of the terms will be assessed in section 4.

The impurity concentration using the complete model gives a measure to compare the impact of

imposing simplifying assumptions:

$$I_{\text{imp}} = \frac{1}{2}(q_{\parallel,\text{cond,e,u}}^2 - q_{\parallel,\text{cond,e,t}}^2) - I_{\text{neutral}} + I_\perp - I_B + I_{\text{conv}} + I_{\text{cond,i}}$$

$$\int_t^u \kappa_{\parallel 0\text{e}} T_e^{5/2} n_e^2 c_\alpha L_\alpha \nabla_\parallel T_e dl_\parallel \approx \langle c_\alpha \rangle_\text{t}^\text{u} \int_t^u \kappa_{\parallel 0\text{e}} T_e^{5/2} n_e^2 L_\alpha dT_e$$

$$\langle c_\alpha \rangle_\text{t}^\text{u} \approx \frac{\frac{1}{2}(q_{\parallel,\text{cond,e,u}}^2 - q_{\parallel,\text{cond,e,t}}^2) - I_{\text{neutral}} + I_\perp - I_B + I_{\text{conv}} + I_{\text{cond,i}}}{\int_t^u \kappa_{\parallel 0\text{e}} T_e^{5/2} n_e^2 L_\alpha dT_e}$$

$$(53)$$

where the impurity is assumed to be constant as the mean weighted by the impurity radiation profile from upstream to target $\langle c_\alpha \rangle_\text{t}^\text{u}$. The reason for weighting the the impurity concentration with the radiation profile is to avoid underestimation as the impurity concentration is lower in regions where the radiation level is low. Eq. 53 forms the baseline of assessing each assumption in the Lengyel and the Feng model. The results from removing each of the integral terms I_x for $x = \{\text{neutral}, \perp, \text{B}, \text{conv}, \text{cond}, \text{i}\}$ is used to conclude whether the effect of removing a term is insignificant or not. These results will be presented and assessed in the final part of section 4.

2.3 The physics of EMC3-EIRENE

The physics of EMC3-EIRENE is based on a two-fluid model for the plasma, a trace model for the impurities and a kinetic model for neutral gas which are self-consistently coupled. EMC3-EIRENE consists of two codes, EMC3 and EIRENE. The EMC3 code provides the background plasma required to compute the plasma-neutral interaction in the EIRENE code [40, 41]. Plasma-neutral interactions are included in this thesis's assessment of energy transport. However, EIRENE includes kinetic theory that is beyond the scope of the discussion of this thesis. Therefore, only the EMC3 model will be described in this subsection.

The continuity and momentum balance equations in the two-fluid model is given by:

$$\nabla \cdot \left(n_i v_{i,\parallel} \boldsymbol{b} - D\nabla_\perp n_i \right) = S_p \tag{54}$$

$$\nabla \cdot \left(m_i n_i v_{i,\parallel}^2 \boldsymbol{b} - \eta_\parallel \nabla_\parallel v_{i,\parallel} \boldsymbol{b} \right) + \nabla_\perp \cdot D\nabla(m_i n_i v_{i,\parallel}) = -\nabla_\parallel p + S_m, \tag{55}$$

where m_i is the ion mass, n_i the ion density and $v_{i,\parallel}$ is the ion fluid velocity. The unit magnetic field vector is denoted as $\boldsymbol{b}$ and the anomalous diffusion coefficient is given by D. The term on the RHS of Eq. 54 is the particle source S_p associated with neutrals. The first term on the RHS of Eq. 55 is the parallel pressure gradient and the second term the momentum source S_m associated with neutrals [41].

The energy transport equation is separated for ions and electrons:

$$\nabla \cdot \left(\frac{5}{2} n_e T_e v_{i,\parallel} \boldsymbol{b} - \kappa_e \nabla_\parallel T_e - \frac{5}{2} T_e D\nabla_\perp n_e - \chi_e n_e \nabla_\perp T_e \right) = -k_e(T_e - T_i) + S_{ee} + S_{imp} \tag{56}$$

$$\nabla \cdot \left(\frac{5}{2} n_i T_i v_{i,\parallel} \boldsymbol{b} - \kappa_i \nabla_\parallel T_i - \frac{5}{2} T_i D\nabla_\perp n_i - \chi_i n_i \nabla_\perp T_i \right) = k_e(T_e - T_i) + S_{ei} \tag{57}$$

where κ_e and κ_i are the parallel classical conductive transport parameters and the D, χ_e, χ_i are the cross-field anomalous transport coefficients which are free parameters in the code. Furthermore, EMC3 assumes that the plasma velocity equals the ion velocity. The source-terms S_{ee} and S_{ei} represent the plasma-neutral interactions calculated in the EIRENE part of the code. The impurity

radiation S_{imp} is computed by a trace-impurity model in EMC3 and is given by:

$$\nabla \cdot \left(n_\alpha^Z v_{\alpha,\parallel}^Z \boldsymbol{b} - D_\alpha^Z \nabla_\perp n_\alpha^Z \right) = S_{Z-1 \to Z} - S_{Z \to Z+1} + R_{Z+1 \to Z} - R_{Z \to Z-1} \tag{58}$$

$$U_{\alpha,\parallel}^Z \left(v_{\alpha,\parallel}^Z - v_{i,\parallel} \right) = -\boldsymbol{b} \cdot \nabla n_\alpha^Z T_\alpha^Z + n_\alpha^Z Z e E_\parallel + n_\alpha^Z Z^2 C_e \boldsymbol{b} \cdot \nabla T_e + n_\alpha^Z C_i \boldsymbol{b} \cdot \nabla T_i \tag{59}$$

$$0 = \boldsymbol{b} \cdot \nabla n_e T_e + n_e e E_\parallel + n_e C_e \boldsymbol{b} \cdot \nabla T_e \tag{60}$$

$$T_\alpha^Z = T_i. \tag{61}$$

The continuity equation for impurities is given in Eq. 58 where n_α^Z is the impurity ion density of species α and ionisation stage Z. The super- and subscripts were chosen to be different from previously in the thesis for readability. These super- and subscripts are consistent throughout the model for other quantities. The parallel impurity velocity is given by $v_{\alpha,\parallel}^Z$ and the impurity diffusion coefficient $D_{\alpha,\parallel}^Z$. On the RHS of Eq. 58 the first two terms denoted by S are the source and sink terms representing ionisation and last two terms denoted by R represent recombination. Intrinsic impurity particles are introduced to the simulation domain through a physical sputtering source [41]. Extrinsic impurities can be introduces as a volume source or as neutrals entering the plasma with an initial kinetic energy E_0 from a particle depot whose location is defined in the code. The total particle source for impurities is either determined by a constant impurity sputtering yield following the description in Stangeby et al. (2000) or by a total radiation boundary condition [8].

The momentum balance equation is given by equations Eq. 59 and 60. The LHS of Eq. 59 represents the friction force on the impurity ions moving with fluid parallel velocity $v_{\alpha,\parallel}^Z$ exerted by the background ions moving with fluid parallel velocity $v_{i,\parallel}$ where $U_{\alpha,\parallel}^Z = \rho_\alpha^Z / \tau_s$ for stopping time τ_s and mass density ρ_α^Z [8]. On the RHS the first term $-\boldsymbol{b} \cdot \nabla n_\alpha^Z T_\alpha^Z = -\boldsymbol{b} \cdot \nabla p_\alpha^Z$ represents the parallel pressure gradient and the second term $n_\alpha^Z Z e E_\parallel$ the electrostatic force. The third term from the left on the RHS $n_\alpha^Z Z^2 C_e \boldsymbol{b} \cdot \nabla T_e$ represents the electron temperature gradient force. The coefficient C_e is related to the Coulomb interaction between the electrons and the impurities. The last term in Eq. 59 $n_\alpha^Z C_i \boldsymbol{b} \cdot \nabla T_i$ represents the ion temperature gradient force where the coefficient C_i is related to the Coulomb interaction between the ions and the impurities. Both coefficients of the two last terms are related to the momentum transfer which decreases strongly with the relative velocity between the colliding particles, i.e., an inverse dependence on the electron and ion temperature $C_{e,i} \propto T_{e,i}^{-3/2}$, respectively. In effect the ions and electrons that strike the impurities from cold regions will transfer more momentum to the impurities than those from the warm regions [8]. Eq. 60 determines the $E_\parallel$ from the electron momentum balance which follows from the imposed quasi-neutrality. Furthermore, the energy balance in Eq. 61 assumes thermal equilibrium between the impurities and the other background ions. Thus, the temperatures of the impurities are equal to the ion temperature as stated in the energy balance of the model.

Conductivity coefficient

The parallel conductivity coefficients characterise the diffusive motion along magnetic field lines. The definition in the EMC3 code follows the definition given in the Braginskii fluid model [42]. The electron conductivity coefficient is defined as:

$$\kappa_{\parallel e} = 3.16 \frac{n_e T_e \tau_e}{m_e} \tag{62}$$

where the electron collision time τ_e is given by:

$$\tau_e = \frac{3\sqrt{m_e} T_e^{3/2}}{4\sqrt{2\pi} \lambda e^4 Z^2 n_i}. \tag{63}$$

The parallel conductivity coefficient for ions is given by:

$$\kappa_{\parallel i} = 3.9 \frac{n_i T_i \tau_i}{m_i} \tag{64}$$

where the ion collision time τ_i is given by:

$$\tau_i = \frac{3\sqrt{m_i}T_i^{3/2}}{4\sqrt{2\pi}\lambda e^4 Z^4 n_i},\tag{65}$$

and the Coulomb logarithm λ is given by:

$$\lambda = \begin{cases} 23.4 - 1.15\log n + 3.45\log T_e, & T_e < 50\text{eV} \\ 25.3 - 1.15\log n + 2.3\log T_e, & T_e > 50\text{eV} \end{cases}\tag{66}$$

2.3.1 Conductive cross-field energy transport

The cross field conductive terms given in Eq. 67:

$$q_{\perp,cond} = -\chi_e n\nabla_\perp T_e - \chi_i n\nabla_\perp T_i,\tag{67}$$

are driven by the the temperature gradients where the transport coefficients χ_e and χ_i are the anomalous energy transport coefficients characterised by turbulent transport [35, 36, 37]. However, in the code they are set as free parameter and can be chosen to be either spatially varying or constant throughout the computational domain.

2.3.2 Convective cross-field energy transport

The cross-field convective terms are given in Eq. 68:

$$q_{\perp,conv} = \frac{5}{2}D(T_e + T_i)\nabla_\perp n,\tag{68}$$

and are driven by the cross-field density gradients $\nabla_\perp n$ and characterised by the anomalous diffusion coefficient D. The diffusion coefficient is characterised by turbulent particle transport and is in the same sense as the anomalous energy transport coefficients a free parameter. In our simulations D, $\chi_{\perp,e}$ and $\chi_{\perp,i}$ are spatially constant.

2.3.3 Source terms

The source terms are given in Eq. 17 where S_{imp} is the power loss due to impurity radiation, and S_{ee} and S_{ei} are the sources and sinks associated plasma-neutral interaction. S_{ee} and S_{ei} includes excitation, ionisation, molecular dissociation and charge-exchange collisions. The total impurity radiation is given in the code by Eq. 12, and the target heat flux is:

$$q_t = n(\gamma_e T_e + \gamma_i T_i)c_s\boldsymbol{b}\tag{69}$$

which is coupled with the plasma-neutral interactions. The plasma-neutral interaction terms S_{ee} and S_{ei} are determined by self-consistently solving a coupled Boltzmann equation which is done in EIRENE [41]. The last term in Eq. 17 is the target heat flux corresponding to the target heat flux density given Eq. 69 where the Bohm boundary condition has been imposed where the plasma sound speed $c_s = \sqrt{(T_e + T_i)/(m_i + m_e)}$. The coefficients γ_e and γ_i are the sheath transmission coefficients for electrons and ions, respectively. The sheath is a microscopic region right in front of the targets. It determines how much power is deposited at the target for given plasma conditions [8]. It has other physical properties than the SOL, and is therefore not the focus of this thesis. It is discussed in further detail in Stangeby (2000) [8].

2.4 Numerical modeling of the fluid equations

The fluid equations in EMC3-EIRENE is equivalent to a stochastic process describing the discrete motion of individual particles. Edge Monte Carlo 3D (EMC3) is based on a Monte Carlo approach to solve the fluid equations [43, 40, 41, 44, 45]. The previously presented fluid equations can be cast in a general Fokker-Planck form:

$$\frac{\partial f(\boldsymbol{x},t)}{\partial t} = \left[-\sum_{i=1}^{N} \frac{\partial}{\partial x_i} D_i^{(1)}(\boldsymbol{x}) + \sum_{i,j=1}^{N} \frac{\partial^2}{\partial x_i \partial x_j} D_{ij}^{(2)}(\boldsymbol{x}) \right] f(\boldsymbol{x},t) \tag{70}$$

where $\boldsymbol{x}$ is the coordinate vector, t is the time, $D_i^{(1)}(\boldsymbol{x})$ the spatially dependent convection coefficient and $D_{ij}^{(2)}(\boldsymbol{x})$ the spatially dependent diffusion coefficient. The Fokker-Planck equation is equivalent with a *master equation* where the transition matrix is equivalent with the operator [·] in front of $f(\boldsymbol{x},t)$ on the RHS of Eq. 70. In other words the transition matrix describes the transition probabilities of an asymmetric random walk along and across the magnetic field lines [46]. The field $f(\boldsymbol{x},t)$ in Eq. 70 describes the spatially and temporally dependent particle distribution for which the statistical moments represent the fluid quantities of interest [46]. Thus, despite different boundary conditions for the fluid moments the generalization of the fluid equations by the Fokker-Planck equation enables the application of this general numerical method to determine $n, v_\parallel, T_e$ and T_i for arbitrary magnetic configurations [41]. To make the equation more interpretable in the case of a plasma immersed in a magnetic field the coefficients are divided into components parallel and perpendicular to the magnetic field:

$$\frac{\partial f(\boldsymbol{x},t)}{\partial t} = -\nabla_\parallel \cdot \left[\alpha_\parallel f(\boldsymbol{x},t) + \nabla_\parallel (\beta_\parallel f(\boldsymbol{x},t)) \right] - \nabla_\perp \cdot \left[\alpha_\perp f(\boldsymbol{x},t) + \nabla_\perp (\beta_\perp f(\boldsymbol{x},t)) \right] \tag{71}$$

where $D_i^{(1)}(\boldsymbol{x})$ from Eq. 70 was decomposed into a parallel and perpendicular component $\alpha_\parallel$ and $\alpha_\perp$ and $D_{ij}^{(2)}(\boldsymbol{x})$ into $\beta_\parallel$ and $\beta_\perp$.

Eq. 70 describes the conservation of the particle distribution, and thus its moments. Therefore, the fluid fields can be determined by simulating the motion of individual particles. Particles are randomly instantiated by a given source distribution, followed in small time steps Δt. So, the motion of the particles are simulated as a random walk in 3D where the step:

$$\Delta r = \sqrt{2\beta_\parallel \Delta t} \xi_\parallel + \alpha_\parallel \Delta t + \sqrt{4\beta_\perp \Delta t} \xi_\perp + \alpha \Delta t \tag{72}$$

where $\xi_\parallel$ and $\xi_\perp$ are random unit vectors from a uniform distribution parallel and perpendicular to the magnetic field, respectively. The terms including the coefficient β are associated with the diffusive transport and the terms including α are associated with convective transport in the direction parallel and perpendicular to the magnetic field denoted by the subscript $\parallel$ and $\perp$, respectively. Thus, a local orthogonal coordinate system is chosen where x_3 is along the magnetic field, and x_1 and x_2 is perpendicular to x_3. Furthermore, the unit base vectors $\{\boldsymbol{e}_i\}_{i=1}^3$ are chosen as:

$$\begin{aligned} \boldsymbol{e}_1 &= -\frac{(\boldsymbol{b} \cdot \nabla)\boldsymbol{b}}{|(\boldsymbol{b} \cdot \nabla)\boldsymbol{b}|} \\ \boldsymbol{e}_2 &= \boldsymbol{b} \times \boldsymbol{e}_1 \\ \boldsymbol{e}_3 &= \boldsymbol{b}, \end{aligned} \tag{73}$$

where $\boldsymbol{b}$ is the unit vector tangential to the magnetic field. Thus, by this choice of unit vector basis the diffusion tensor becomes:

$$\boldsymbol{D} = D_\perp \boldsymbol{e}_1 \boldsymbol{e}_1 + D_\perp \boldsymbol{e}_2 \boldsymbol{e}_2 + D_\parallel \boldsymbol{e}_3 \boldsymbol{e}_3 = (D_\parallel - D_\perp)\boldsymbol{b}\boldsymbol{b} + D_\perp \boldsymbol{I} \tag{74}$$

where $\boldsymbol{bb}$ is given in dyadic notation. The transport coefficient from Eq. 71, α and β, are related to the diffusion coefficient $\boldsymbol{D}$ as follows [44, 41]:

$$\alpha_\parallel = \boldsymbol{b} \cdot (\boldsymbol{V} + \nabla D_\parallel) - (D_\parallel - D_\perp)\nabla \cdot \boldsymbol{b} \tag{75}$$

$$\alpha_\perp = (\boldsymbol{e}_1 + \boldsymbol{e}_2) \cdot (\boldsymbol{V} + \nabla D_\perp) - (D_\parallel - D_\perp)|(\boldsymbol{b} \cdot \nabla)\boldsymbol{b}| \tag{76}$$

$$\beta_\parallel = D_\parallel \tag{77}$$

$$\beta_\perp = D_\perp \tag{78}$$

The fluid moments are computed by averaging over the distribution of particles at each cell in the computational domain. This is done by estimating the fluid moment:

$$f_j = \frac{1}{C_j} \sum_i w_i \frac{l_i}{v_i} = \frac{1}{C_j} \sum_i w_i \Delta t_i, \tag{79}$$

where f_j represents the fluid moment in cell j, C_j. The sum on the RHS of Eq. 79 is over all visits of the particles at cell j. The weight quantity of the particle, associated with the integrands of the moment, is given by w_i, the traced length l_i, the velocity of the particle v_i and the time spent in cell j, t_i [44].

2.4.1   Field line tracing and grid generation

The grid used for the simulation domain is generated through the same field line tracer used in this thesis's framework of the analysis. Thus, both will be described in this subsection. The field line tracing used in this thesis is a reversible field line mapping (RFLM) technique developed by Feng et al. [45]. It ensures a unique and continuous reconstruction of the field lines given a discretized field-aligned grid combining a reversible field line mapping technique and a bilinear interpolation scheme.
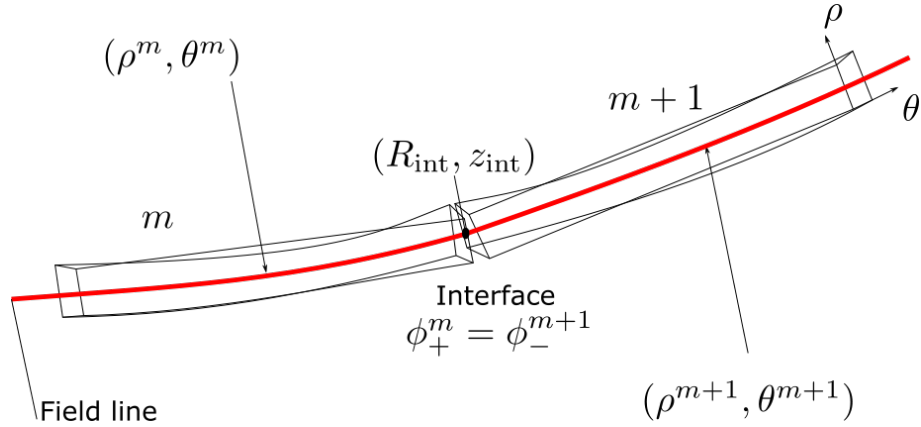
Figure 20: The field line illustrated in red has toroidal coordinates (ρ, θ, ϕ). The superscript m and $m + 1$ on the toroidal angle indicates that the coordinates are for consecutive cells m and $m + 1$. At the interface $\phi_+^m = \phi_-^{m+1}$, which is the equality of the toroidal angle at the interface of two consecutive grid cells m and $m + 1$.
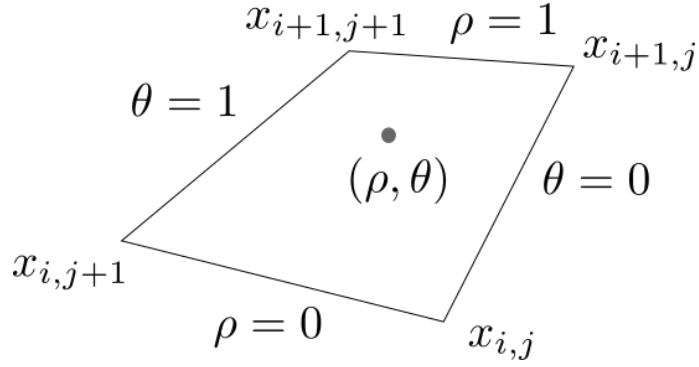
Figure 21: The local coordinates $\{x_{i,j}\}_{i=0,j=0}^{1,1}$ of the flux tube cross-section at the intermediate toroidal tracing coordinates ϕ_k is shown. The toroidal index k is omitted and the local field line coordinates (ρ, θ) are given by the grey dot representing the intersection between the cross-section and the field line.

The reversible field line mapping starts with dividing the computational domain into toroidal subdomains. A 2D radial-poloidal grid is defined for a constant toroidal angle $\phi_0^m = \text{const}$. The grid contours are closed and nested extending radially inwards within the LCFS to match SOL with the confined region. Fig. 20 shows two consecutive cells denoted by the toroidal subdomain m and $m+1$. The field line is integrated numerically in positive and negative field directions up to ϕ_+^m and ϕ_-^m, respectively. The coordinates of the field line are stored in intermediate toroidal positions $\phi_k \in [\phi_-^m, \phi_+^m]$. This is done for all cells in the 2D grid and the result is a 3D mesh defining a 2D set of finite flux tubes in the toroidal subdomain m. This process is continued for the next toroidal subdomain $m+1$ where the toroidal positions of the field line is $\phi_k \in [\phi_-^{m+1}, \phi_+^{m+1}]$ with $\phi_-^{m+1} = \phi_+^m$.

For W7-X the magnetic configuration exhibits stellarator symmetry:

$$B_R(R, z, \phi^\star) = -B_R(R, -z, -\phi^\star)$$
$$B_z(R, z, \phi^\star) = B_z(R, -z, -\phi^\star) \tag{80}$$
$$B_\phi(R, z, \phi^\star) = B_\phi(R, -z, -\phi^\star)$$

$$\tag{81}$$

where R is the major radius, z is the vertical distance over the midplane, and $\phi^\star = \phi - \phi_s$ where ϕ_s is the toroidal angle at an up-down symmetric poloidal cross-section. The toroidal range of the subdomains is bounded by the constraint on the deformation of the flux tubes in 3D, i.e. the cells has to be convex for the bilinear interpolation to work. Thus, the toroidal range of the subdomains depends on the magnetic shear, the curvature of the flux surface and the contours of the islands in the poloidal cross-section. A single subdomain was sufficient to satisfy the convexity constraint for W7-X [45]. Thus, the 3D grid cells are generalized hexahedra with every quadrilateral face satisfying the convexity constraint.

Any field line inside a finite flux tube shown in Fig. 20 has the local coordinates (ρ, θ) where $\rho, \theta \in [0, 1]$. At every intermediate toroidal position ϕ_k the cylindrical coordinates $x = (R, z)$ defining the mesh corners can be computed by a bilinear interpolation from the four corners of the flux tube cross-section, which are the stored values of the grid. The four corners of the flux tube cross-section at ϕ_k, $\{x_{ijk}\}_{i,j,k=0}^{1,1,1}$, are illustrated in Fig. 21. The real space coordinates $x = (R, z)$ as a function of the local coordinates (ρ, θ) is given by:

$$x(\rho, \theta, \phi_k) = x_{i,j,k} + (x_{i+1,j,k} - x_{i,j,k})\rho + (x_{i+1,j,k} - x_{i,j,k})\theta$$
$$+ (x_{i+1,j+1,k} - x_{i,j+1,k} - x_{i+1,j,k} + x_{i,j,k})\rho\theta \tag{82}$$
$$x = f(\xi, \{x_{ijk}\}_{i,j,k=0}^{1,1,1}) \tag{83}$$

where Eq. 83 is an abbreviation of Eq. 82, and $\xi \equiv (\rho, \theta)$. The mapping $x \leftrightarrow \xi$ is one-to-one for any point inside any finite flux tube as follows from the convexity property of the cell [45]. At the

interface ϕ_+^m a field line with flux-tube coordinates ξ^m in toroidal subdomain m has the real space coordinates:

$$x_{\text{int}} = f(\xi^m, \{x_{ij,+}^m\}_{i,j=0,+}^{1,1}). \tag{84}$$

The flux tube coordinates in toroidal subdomain $m + 1$ is obtained by inverting Eq. 84:

$$x_{\text{int}} = f(\xi^{m+1}, \{x_{ij,-}^{m+1}\}_{i,j=0,-}^{1,1}) \tag{85}$$

for a given set of real space coordinates x_{int}. Eq. 84 is equivalent to Eq. 85, except that the latter is applied to a flux tube enclosing the field line in the consecutive toroidal subdomain with common interface $\phi_+^m = \phi_-^{m+1}$. Combining Eqs.84 and 85 the mapping from local coordinates to real space coordinates can be expressed as a reversible mapping through the common interface:

$$f(\xi^m, \{x_{ij,+}^m\}_{i,j=0,+}^{1,1}) = x_{\text{int}} = f(\xi^{m+1}, \{x_{ij,-}^{m+1}\}_{i,j=0,-}^{1,1}). \tag{86}$$

Eq. 86 shows that the transfer of the field line from one toroidal subdomain to the consecutive toroidal subdomain through the interface does not change the real-space coordinates x_{int}. So, the mapping is therefore error free [45]. Thus, once a field line is traced in a given subdomain it extends continuously to the consecutive subdomain, where the trajectory of the field line is uniquely determined in all the subdomains regardless of the tracing direction. The reversibility property of the field line tracing is crucial to the numerical treatment of the fluid equations in the EMC3 code. Large cross-field numerical diffusion errors arising from fast parallel transport are avoided because of the reversibility property [45].

Since the mesh is grid aligned the flux-tube cross-section is deformed. Therefore, the bilinear interpolation of the field lines inside the flux tube introduces a second order error in the mesh size ΔL_{mesh}. The deformation increases with the toroidal extent of the flux tube, but if the flux tube is short enough it scales linearly with the flux-tube length $\Delta L_\parallel$:

$$\delta x = \mathcal{O}\left([\Delta L_{\text{mesh}}]^2\right) \Delta L_\parallel. \tag{87}$$

The computational domain used in this thesis consists of half modules extending $36°$ toroidally. Due to the up-down symmetry property of the W7-X the half modules can be put together forming a full module which extends $72°$ toroidally. Thus, the whole torus consist of 5 identical full modules and 10 half modules where every pair of half modules are up-down symmetric. Since the computational domain is divided into half modules the fluid fields must be mapped at the bounds of the computational domain when obtaining profiles of the fluid fields along the field lines.
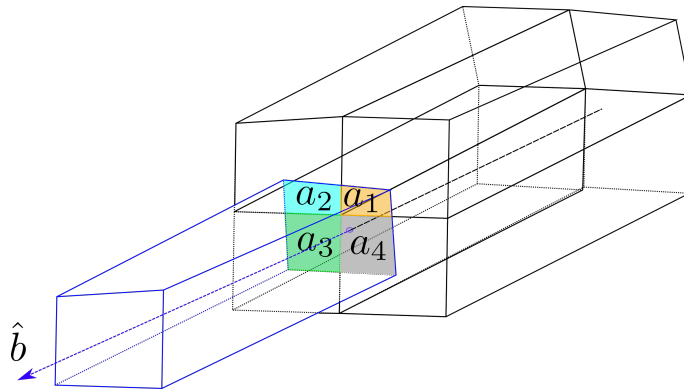
Figure 22: The mapping of fluid fields stored in the flux tubes. The overlap areas $\{a_i\}_{i=1}^4$ at the mapping surface weighs the fluid field from the previous flux tubes in black to the flux tube toroidally after the mapping surface. A field line is indicated by the black (before mapping) and blue (after mapping) dashed line.

Furthermore, the fluid profiles of the field lines are discontinuous due to the mapping surface at the bounds of the computational domain called the triangular cross-sections where $\phi = 36° + n72°; n \in$

[0, 4]. One flux tube cross-section is mapped to adjacent flux tubes with overlapping areas at the mapping surface as shown in Fig. 22. The fluid fields in the mapping procedure is weighted by the overlap area of adjacent flux tubes:

$$f_{\text{new}} = \sum_{i=1}^{4} f_i a_i / \sum_{i=1}^{4} a_i, \tag{88}$$

where f_{new} is the fluid field of the fluxed tube adjacent to the flux tubes toroidally before the mapping surface with fluid field values $\{f_i\}_{i=1}^{4}$. as shown in Fig 22. The displacement of the flux tubes at the mapping surface compensates for the field line motion towards the targets. If there was no displacement between adjacent flux tubes the parallel transport would not have a component in the radial direction of the grid. The grid was constructed such that the poloidal cross-sections at $\phi = 0° + n72°; n \in [0, 5]$ called the bean cross-section are identical when stellarator symmetry is imposed. So, the mapping from one bean cross-section to another does not involve any relative displacement of the adjacent flux tubes.

2.5 Field line energy analysis framework

The toroidal symmetry of tokamaks allows for a two-dimensional energy transport analysis whereas this is not the case for stellarators. Moulton et al. (2021) analyse the heat load limiting flux tube as introduced in section 3 [5]. In stellarators the simplification of analysing a flux tube is impossible since they are not axisymmetric. The framework for energy transport analysis introduced in this thesis builds upon the same idea as Moulton et al. (2021). However, it is directly related to transport along field lines, making the analysis three-dimensional. So, instead of looking at toroidal flux tubes, the field line intersecting the targets at the peaks of the heat flux distribution will be regarded as the main contribution to the target load.

The field line tracer described previously in this section requires an initial position and traces in both directions of the field. The initial position of the field line tracer is chosen to be at the peaks of the heat flux distribution at each target. The number of peaks is limited by setting a threshold α where all chosen points satisfies:

$$\{q_t\}^{\text{peaks}} \geq \alpha \|q_t\|_{\infty}; \quad \alpha \in [0, 1]. \tag{89}$$

where $\|q_t\|_{\infty}$ is the maximum of the heat flux distribution at each target individually. So, selection of points are chosen relative to the value of the peak heat flux at each target. The points were selected by setting $\alpha = 0.75$ and are shown in Fig. 23. The other points in purple are reference points to check for consistent behaviour of the energy transport along the field line for field lines that are not associated with the hot spots at the targets. The method used in this thesis for selecting initial positions for the field line tracer was intended to explore the physics of field lines that end up at every target.
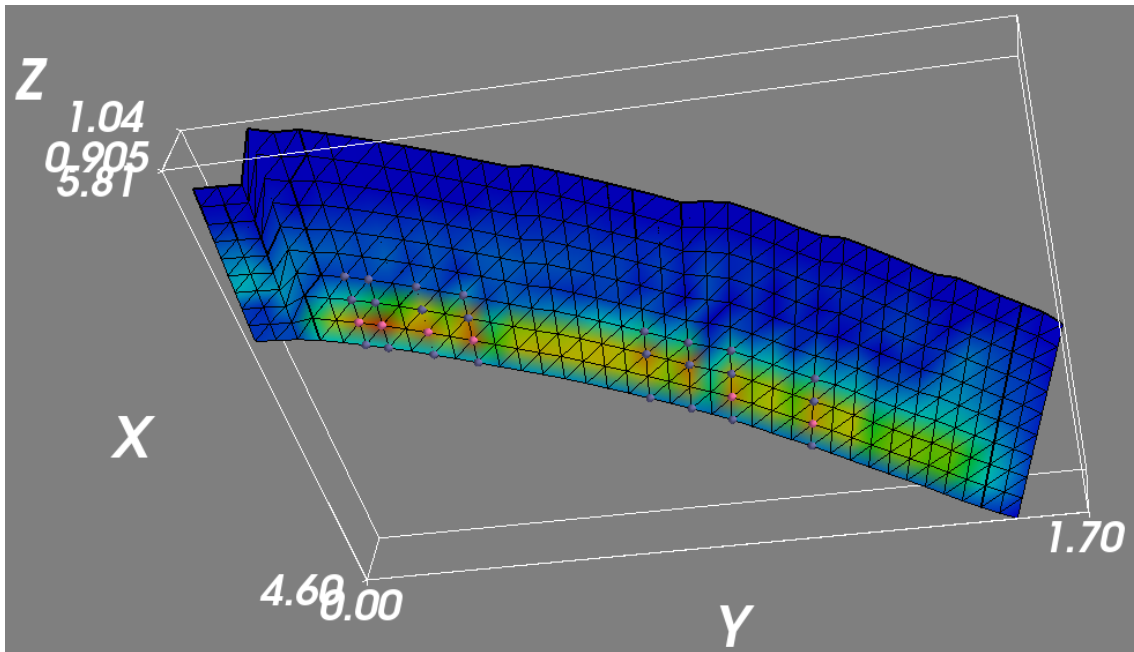
(.1) Upper horizontal target.
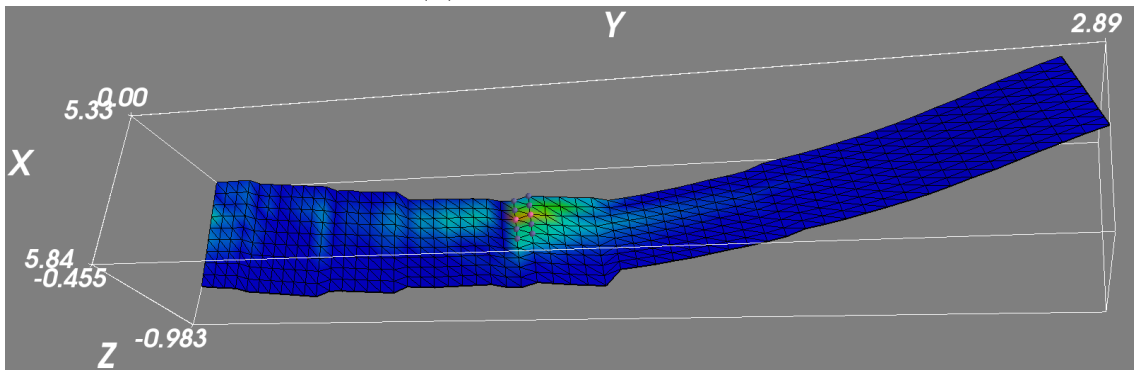
(.2) Lower horizontal target.
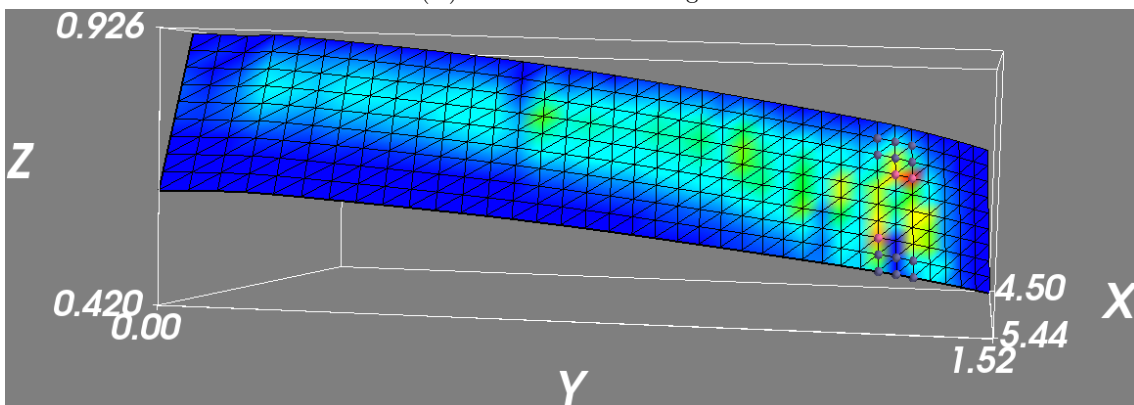
(.3) Upper vertical target.

Figure 23: Heat flux distribution on the divertor targets. Red indicates a large value of the heat flux density, and dark blue zero. The points in pink satisfies Eq. 89.

Each term in the local energy balance is given for each field line. Thus, the fields along field lines selected by the condition in Eq. 89 are evaluated by the integral in Eq. 52. The assumptions made in Feng's and Lengyel's models can be assessed by sequentially removing terms from the divertor impurity concentration given in Eq. 53 until the same form as given in the respective models is

obtained. In this thesis the only impurity considered was carbon, an intrinsic impurity in W7-X because the divertor targets are made of carbon-fiber composite [18]. Thus, carbon is an intrinsic impurity because it is introduced to the plasma via sputtering from the walls [8]. The assessment is done by the following steps:

1. Compute the impurity concentration in the divertor directly from the impurity densities for each ionisation stage of carbon:

$$c_{\rm C} = \sum_{Z=0}^{Z_0} c_Z/n_e. \tag{90}$$

This will be used as a baseline for assessing the validity of the assumption made in the Lengyel and Feng model.

2. The divertor impurity concentration is approximated by:

$$\langle c_{\rm C} \rangle_{\rm t}^{\rm u} \approx \frac{\frac{1}{2}(q_{\|,{\rm cond,e,u}}^2 - q_{\|,{\rm cond,e,t}}^2) - I_{\rm neutral} + I_\perp - I_{\rm B} + I_{\rm conv} + I_{\rm cond,i}}{\int_t^u \kappa_{\|0{\rm e}} T_e^{5/2} n_e^2 L_\alpha dT_e} \tag{91}$$

3. $I_{\rm cond,i}$ is assumed to be negligible:

$$\langle c_{\rm C} \rangle_{\rm t}^{\rm u} \approx \frac{\frac{1}{2}(q_{\|,{\rm cond,e,u}}^2 - q_{\|,{\rm cond,e,t}}^2) - I_{\rm neutral} + I_\perp - I_{\rm B} + I_{\rm conv}}{\int_t^u \kappa_{\|0{\rm e}} T_e^{5/2} n_e^2 L_\alpha dT_e} \tag{92}$$

4. $I_{\rm conv,e}$ is assumed to be negligible:

$$\langle c_{\rm C} \rangle_{\rm t}^{\rm u} \approx \frac{\frac{1}{2}(q_{\|,{\rm cond,e,u}}^2 - q_{\|,{\rm cond,e,t}}^2) - I_{\rm neutral} + I_\perp - I_{\rm B} + I_{\rm conv,i}}{\int_t^u \kappa_{\|0{\rm e}} T_e^{5/2} n_e^2 L_\alpha dT_e} \tag{93}$$

5. $I_{\rm conv,i}$ is assumed to be negligible:

$$\langle c_{\rm C} \rangle_{\rm t}^{\rm u} \approx \frac{\frac{1}{2}(q_{\|,{\rm cond,e,u}}^2 - q_{\|,{\rm cond,e,t}}^2) - I_{\rm neutral} + I_\perp - I_{\rm B}}{\int_t^u \kappa_{\|0{\rm e}} T_e^{5/2} n_e^2 L_\alpha dT_e} \tag{94}$$

6. $I_{\rm B}$ is assumed to be negligible:

$$\langle c_{\rm C} \rangle_{\rm t}^{\rm u} \approx \frac{\frac{1}{2}(q_{\|,{\rm cond,e,u}}^2 - q_{\|,{\rm cond,e,t}}^2) - I_{\rm neutral} + I_\perp}{\int_t^u \kappa_{\|0{\rm e}} T_e^{5/2} n_e^2 L_\alpha dT_e} \tag{95}$$

7. The transfer of power due to cross-field transport $I_\perp$ is assumed to be negligible:

$$\langle c_{\rm C} \rangle_{\rm t}^{\rm u} \approx \frac{\frac{1}{2}(q_{\|,{\rm cond,e,u}}^2 - q_{\|,{\rm cond,e,t}}^2) - I_{\rm neutral}}{\int_t^u \kappa_{\|0{\rm e}} T_e^{5/2} n_e^2 L_\alpha dT_e} \tag{96}$$

8. The plasma-neutral interaction loss $I_{\rm neutral}$ is assumed to be negligible:

$$\langle c_{\rm C} \rangle_{\rm t}^{\rm u} \approx \frac{\frac{1}{2}(q_{\|,{\rm cond,e,u}}^2 - q_{\|,{\rm cond,e,t}}^2)}{\int_t^u \kappa_{\|0{\rm e}} T_e^{5/2} n_e^2 L_\alpha dT_e} \tag{97}$$

9. The electron static pressure $p_e = n_e T_e$ is assumed constant and set to the upstream value $p_e = p_{e,{\rm up}}$:

$$\langle c_{\rm C} \rangle_{\rm t}^{\rm u} \approx \frac{\frac{1}{2}(q_{\|,{\rm cond,e,u}}^2 - q_{\|,{\rm cond,e,t}}^2)}{p_{e,{\rm up}}^2 \int_t^u \kappa_{\|0{\rm e}} T_e^{1/2} L_\alpha dT_e} \tag{98}$$

10. The temperature-independent parallel electron conductivity coefficient $\kappa_{\|0e}$ is assumed constant and set to the mean along the field line value from upstream to the target $\kappa_{\|0e} = \langle \kappa_{\|0e} \rangle_{\rm t}^{\rm u}$ and $q_{\|,{\rm cond,e,t}} = 0$:

$$\langle c_{\rm C} \rangle_{\rm t}^{\rm u} \approx \frac{\frac{1}{2}q_{\|,{\rm cond,e,u}}^2}{p_{e,{\rm up}}^2 \langle \kappa_{\|0e} \rangle_{\rm t}^{\rm u} \int_t^u T_e^{1/2} L_\alpha dT_e} \tag{99}$$

2.6 Global energy analysis

A global energy analysis was carried out to assess the consistency between the field line treatment of the contribution to the targets and the total target heat load. This analysis is similar to what was done in the paper by Feng [1].

2.6.1 Grid structure

The grid structure needs to be described to present the global energy balance analysis framework. The grid is constructed with cylindrical coordinates (R, z, ϕ) where R is the major radius, z is the vertical distance from the midplane and ϕ the toroidal angle given in radians. Furthermore, the grid is structured with dimensions (i_r, i_θ, i_ϕ) representing the grid's radial, poloidal and toroidal dimensions, respectively. In this thesis the grid has dimensions $(i_r, i_\theta, i_\phi) = (129, 398, 36)$. The structure of the cell is shown in Fig. 24. The scalar fields are cell-centred and uniquely defined for each radial, poloidal and toroidal grid cell.
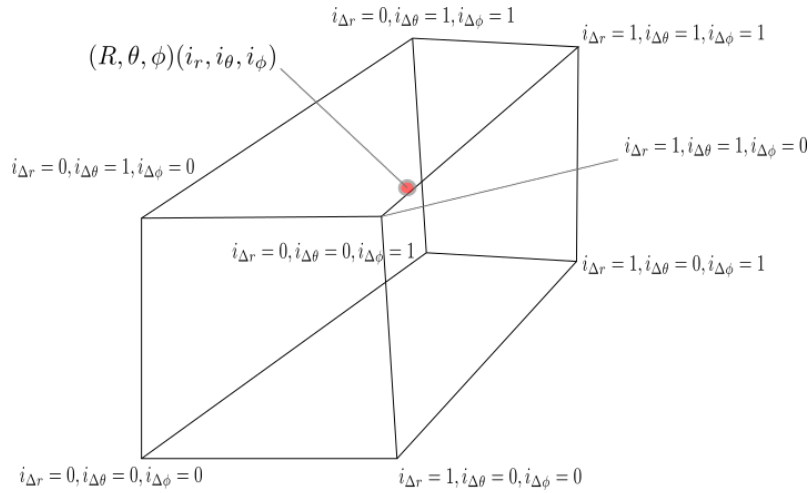
Figure 24: The structure of a grid cell is shown. The coordinates of the computational domain are defined at each corner of every grid cell. The corners of a grid cell is given by local radial, poloidal and toroidal indices $\{i_{\Delta r}, i_{\Delta \theta}, i_{\Delta \phi}\}$, respectively. The scalar field obtained in the simulations are defined at the center of mass of each grid cell shown as the red dot. All scalar field quantities are given for radial, poloidal and toroidal indices $\{i_r, i_\theta, i_\phi\}$.

2.6.2 Global energy balance

The global energy balance was computed by the volume integral over the local energy balance cumulatively up to a radius r given by Eq. 19. The radial integration was defined numerically by summing over a radial index i_r. The volume integral can be expressed as the cumulative sum:

$$P_{\text{SOL}} = \sum_{i'_r=20}^{i_r} \sum_{i_\theta=20}^{398} \sum_{i_\phi=20}^{36} (\nabla \cdot \boldsymbol{q} - S_{ee} - S_{ei} - S_{imp}) dV_{\text{cell}}(i'_r, i_\theta, i_\phi) - Q_t(i_r) \tag{100}$$

where the cross-field term on the LHS $\nabla \cdot \boldsymbol{q}_\perp dV(i_r = 20)$ was set to 4.5 MW as the heat entering the SOL from the core across the LCFS ($i_r = 20$) is through cross-field transport. The cell volumes $dV(i_r, i_\theta, i_\phi)$ was computed by subdividing the grid cells into tetrahedra. Then the volume of each tetrahedra wa computed and the volume of the grid cell was evaluated by summing over all the tetrahedra making up the grid cell. The subdivision was done such that the hexahedral cell was divided into the least amount of tetrahedra which was 5 [47].

2.6.3 Radial heat flux densities

The heat flux densities are computed as described in Eqs. 56 and 57. However, the radial displacement needed to compute the gradients is taken to be the distance along the radial index i_r with respect to cylindrical axis of the grid indicated by the black dot in Fig. 25. The cylindrical axis $\{R_0^j, z_0^j, \phi_0^j\}_{j=0}^{\max(i_\phi)}$ is taken as the poloidal mean of the inner radial boundary surface for each toroidal angle, and will thus change with the toroidal angle:

$$\{R_0^j, z_0^j, \phi_0^j\}_{j=0}^{\max(i_\phi)} = \langle (R, z, \phi^i) \rangle_{i_\theta, i_r=0, i_\phi=i_\phi^j} \tag{101}$$

where the superscript $\max(i_\phi)$ indicates the toroidal indices' maximum value. The toroidal angles ϕ in the set of coordinates centered at the cylindrical axis are identical to the original toroidal grid angles. Curly brackets $\{\cdot\}$ is used to indicate the set of a quantity where the sub- and superscript indicate the range of grid indices for which the set is selected.
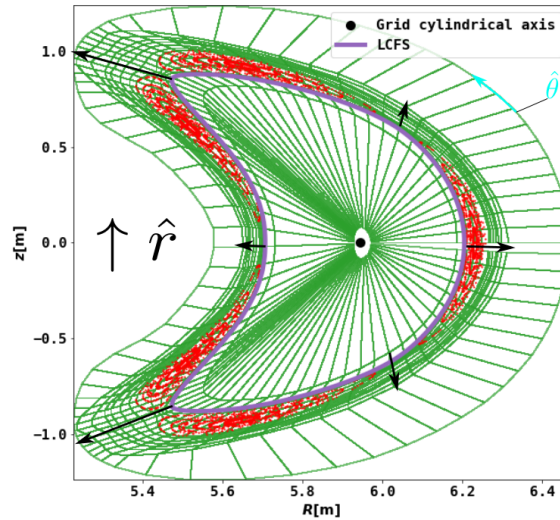
Figure 25: A coarse version of the EMC3 grid is plotted for a poloidal cross-section with green edges at $\phi = 0°$ for every 10th radial and 5th poloidal index. The radial and poloidal directions are indicated by the black and cyan arrows, respectively. The purple line represents the LCFS and the magnetic islands are shown as a Poincaré section in red. The black dot is the cylindrical axis of the grid computed by the poloidal mean of the inner radial surface of the poloidal cross-section where the coordinates $\{R_0^j, z_0^j, \phi_0^j\}_{j=0}^{\max(i_\phi)}$ of the cylindrical axis are dependent on the toroidal angle.

In order to illustrate how the grid resolves the magnetic islands the island are plotted as a Poincaré section over the grid. The coordinates (r_c, z_c) centered at the cylindrical axis is defined as:

$$\{r_c\}_{j=0}^{\max(i_\phi)} = \{R\}_{j=0}^{\max(i_\phi)} - \{R_0\}_{j=0}^{\max(i_\phi)} \tag{102}$$

$$\{z_c\}_{j=0}^{\max(i_\phi)} = \{z\}_{j=0}^{\max(i_\phi)} - \{z_0\}_{j=0}^{\max(i_\phi)}. \tag{103}$$

The radial gradients of the density and temperature fields $\{T_e, n_e\}$ was computed as follows:

$$\nabla_{r_c} \{T_e, n_e\}(i_\theta, i_\phi) = \frac{\{T_e, n_e\}(i_r + 1, i_\theta, i_\phi) - \{T_e, n_e\}(i_r, i_\theta, i_\phi)}{|\boldsymbol{r}_c(i_r + 1, i_\theta, i_\phi) - \boldsymbol{r}_c(i_r, i_\theta, i_\phi)|} \tag{104}$$

where the derivative was computed for any poloidal and toroidal grid index i_θ and i_ϕ, respectively, between radial surfaces defined at radial indices $i_r + 1$ and i_r. The region of interest for these gradients were defined from the LCFS ($i_r = 20$).

2.6.4 Poincaré map

For magnetic field lines a Poincaré map is defined by the tracing the points along a field line that intersect a 2D cross-section. The equation for a magnetic field line is [48, 49]:

$$\frac{d\boldsymbol{r}(s)}{ds} = \frac{\boldsymbol{B}}{|\boldsymbol{B}|} \tag{105}$$

where $\boldsymbol{r}(s)$ is the coordinates of a point on the field line dependent on the field line arclength s. Specifically for the field line tracer used to make the Poincaré map Eq. 105 is solved with the initial condition $\boldsymbol{r}(0)$ and the magnetic filed computed with Biot-Savart's law for a given set of coils and coil currents [48]. In this thesis the coil configuration and coil currents used for making the Poincaré map corresponds to the standard magnetic field configuration in the W7-X. For a cylindrical coordinate system with coordinates (R, z, ϕ) the field line equations is given by:

$$\frac{1}{R}\frac{dz}{d\phi} = \frac{B_z}{B_\phi} \tag{106}$$

$$\frac{1}{R}\frac{dR}{d\phi} = \frac{B_R}{B_\phi} \tag{107}$$

where the magnetic field components $\boldsymbol{B} = B_R\hat{R} + B_z\hat{z} + B_\phi\hat{\phi}$ can be determined by the vector potential $\boldsymbol{A}$ through the equation $\boldsymbol{B} = \nabla \times \boldsymbol{A}$.

The cylindrical coordinates are related to the toroidal coordinates through:

$$R = R_0 + r\cos\theta \tag{108}$$

$$z = r\sin\theta \tag{109}$$

where R_0 is the major radius of the torus and r the minor radial coordinate. In the thesis the Poincaré plots were made by using the web services field line tracer [48].

2.7 Simulation cases

The most important parameters chosen for the EMC3 simulations carried out for this thesis is shown in Table 2.

f_{rad}[%]	n_u[m^{-3}]	P_{IBS}[MW]	$D_\perp$[m^{2}s^{-1}]	$\chi_{\perp,\text{e,i}}$[m^{2}s^{-1}]
20	3.5×10^{19}	4.5	0.25	0.75
80	3.5×10^{19}	4.5	0.25	0.75

Table 2: Key parameters of EMC3 simulation cases where $f_{rad} = \{0.2, 0.8\}$.

For both cases the SOL input power P_{IBS} was chosen as 4.5MW and distributed in such a way that the plasma temperature T_e was constant over the inner boundary surface (IBS) defined at radial index $i_r = 9$. The upstream density $n_u = 3.5 \times 10^{19}$m^{-3} constant over the radial surface corresponding to the LCFS. Moreover, a constant diffusion coefficient $D = 0.25$m^{2}s^{-1} and cross-field conductivity coefficients $\chi_e = \chi_i = 3 \cdot D = 0.75$m^{2}s^{-1} was chosen throughout the computational domain where the linear relation between the diffusive and the conductivity coefficient is based on experimental estimations from density scans [20]. For both simulations a radiation boundary condition was chosen as a fraction of the SOL input power. In other words the total energy loss fraction $f_{\text{rad}} = P_{\text{rad}}/P_{\text{IBS}}$ due to impurity radiation was chosen represent a low $f_{\text{rad}} = 20\%$ and high radiation scenario $f_{\text{rad}} = 80\%$. A low and high radiation scenario was chosen to determine the consistency of the energy transport properties with respect to the radiated fraction as well as representing an attached and detached plasma. Furthermore, for the high radiation case $f_{\text{rad}} = 80\%$ was chosen to represent phase I of the two detachment phases described in Feng et al. (2021) [1].

3 Simplified SOL energy transport models

The energy balance can be simplified when removing terms from Eq. 14 gives approximately equal values on both sides of the equation. Lengyel, Post, Stangeby, and Feng have derived simplified models for energy transport in the SOL [6, 7, 8, 38, 4]. Most importantly, they all assume that the impurity radiation dominates the energy sink and source terms implying that plasma-neutral interaction sources and sinks S_{neutral} are insignificant. Regardless of divertor configuration, the parallel electron conductive heat flux density is much larger than the cross-field heat flux density, i.e., $q_\perp/q_\parallel \ll 1$. However, for the heat flux in the direction of the radial distance from the last closed flux surface this is not necessarily the case [4, 1]. The radial projection of the parallel terms are much smaller than their total magnitude $q_\parallel \hat{b} \cdot \hat{r}/|q_\parallel| \ll 1$. The field line pitch Θ is introduced by Feng as the radial projection parameter of the parallel transport. The magnitude of Θ determines the parallel and perpendicular transport ratio. This ratio is important to establish before deriving a scaling law because it determines which terms need to be included in the model. The two models presented in the following subsections are simplified models for the energy balance in the SOL of magnetically confined plasmas.

3.1 Lengyel model

In 1981 Lengyel wrote a report on the stability and equilibrium properties of radiating plasma boundary layers [6]. His objective was to obtain information about the properties of the radiation layers with respect to the magnitude of the energy flux that can be removed from the plasma by the impurity radiation while the impurity content is kept at a tolerable level with respect to the radiation loss in the core [6]. Lengyel assumes time-independence is for the local energy balance. Thus, the simplified version of the time-independent energy balance and transport equations given in Eqs. 42 and 43 describing the transport along magnetic field lines (Eq. 111) and the loss due to impurity radiation (Eq. 110) is :

$$\nabla_\parallel q_\parallel = -n_e^2 c_\alpha L_Z(T_e) \tag{110}$$

$$q_\parallel = -\kappa_{0,e} T_e^{5/2} \nabla_\parallel T_e \tag{111}$$

where $L_Z(T_e)$ the electron temperature dependent radiated power loss function for equilibrium fractional abundances [6, 50]. The ionisation distribution is given by the density of the ionisation stages of the impurities with respect to the temperature. Eq. 110 is a simplified version of the local energy balance. Lengyel made the following assumptions in order to reduce the equation to the form given in Eqs. 110 and 111:

1. Parallel conductive electron energy transport is dominant.

2. Sources and sinks due to plasma-neutral interactions are insignificant. All dissipation is due to impurity radiation.

3. The effect of the impurity transport on the fractional abundances can be included by using a single constant residence time for the impurities [5, 51]. Thus, the radiation power loss function only depends on the electron temperature.

By combining the pair of equations Eq. 110 and 111, and dividing by the temperature gradient along a field line, we get an expression for the square of the heat flux density and the temperature profile [6, 7]:

$$\frac{\partial q_\parallel^2}{\partial T} = \kappa_{0,e} T_e^{5/2} n_e^2 c_\alpha L_Z(T). \tag{112}$$

Eq. 112 can be solved with respect to the temperature dependent heat flux density for a given temperature profile:

$$\int_{q_{\parallel,\text{t}}}^{q_{\parallel,\text{up}}} dq_\parallel^2 = \int_{T_0}^{T} \kappa_{0,e} T_e'^{5/2} n_e^2 c_\alpha L_Z(T_e') dT_e' \tag{113}$$

where the RHS is integrated along the temperature profile from the inner boundary temperature T_0. The RHS represents the losses due to impurity radiation. *Upstream* can be considered as the maximum temperature along a field line going from target to target, and downstream the position where the field line ends up at the target. Integrating from downstream to upstream conditions Eq. 113 becomes:

$$q_{\parallel,\text{up}}^2 - q_{\parallel,\text{t}}^2 = p_e^2 c_\alpha \int_{T_\text{t}}^{T_\text{up}} \kappa_{0e} T_e'^{1/2} L_Z(T_e') dT_e' \tag{114}$$

where the static electron static pressure p_e and the impurity concentration c_α is assumed constant along the field line. p_e was set to the upstream value $p_e = p_{e,\text{up}}$. The value of the impurity concentration is given by the average of the impurity concentration $\langle c_\alpha \rangle_{T_e^\text{SOL}}$ over the temperature range of the SOL indicated by the subscript T_e^SOL of the averaging brackets. Furthermore, the equation can be rewritten as the ratio between the heat flux densities at the targets and the entrance of the SOL:

$$\frac{q_{\parallel,\text{t}}}{q_{\parallel,\text{up}}} = \left[1 - \frac{p_{e,\text{up}}^2 c_\alpha \int_{T_\text{t}}^{T_\text{up}} \kappa_{0,e} T_e'^{1/2} L_Z(T_e') dT_e'}{q_\parallel^2(T_\text{t})} \right]^{1/2}. \tag{115}$$

By defining the radiated power fraction $f_\text{rad} \equiv 1 - q_{\parallel,\text{t}}/q_{\parallel,\text{up}}$ the equation can be rewritten:

$$1 - f_\text{rad} = \left[1 - \frac{p_{e,\text{up}}^2 c_\alpha \int_{T_t}^{T_{up}} \kappa_{0,e} T_e'^{1/2} L_Z(T_e') dT_e'}{q_\parallel^2(T_t)} \right]^{1/2}$$

$$f_\text{rad} = 1 - \left[1 - \frac{p_{e,\text{up}}^2 c_\alpha \int_{T_t}^{T_{up}} \kappa_{0,e} T_e'^{1/2} L_Z(T_e') dT_e'}{q_\parallel^2(T_t)} \right]^{1/2} \tag{116}$$

which makes the LHS comparable to experimental values as the total radiated power P_rad can be measured by a bolometer and $f_\text{rad} = P_\text{rad}/P_\text{in}$.

3.2 Including cross-field transport - Feng model

Correcting for the effect of the field line pitch in the ID requires the cross-field terms to be included. Assuming that transport still is conduction dominated, Feng expresses the energy transport equation with both parallel and cross-field transport terms projected in the radial direction x from the LCFS [4]:

$$\frac{\partial q}{\partial x} = -n_e^2 c_\alpha L_Z(T_e) \tag{117}$$

$$q = D_\perp \frac{\partial T_e}{\partial x} \tag{118}$$

$$D_\perp = \kappa_{0,e} T_e^{5/2} \Theta^2 + \chi_e n_e \tag{119}$$

where $D_\perp$ is the effective radial conductive diffusion coefficient and Θ is the divertor relevant field line pitch. From here on out, it will be referred to as just the field line pitch. To give a rigorous definition of Θ is difficult, but this thesis will use the definition as given in section 1. This is expressed mathematically as:

$$\Theta = \frac{\Delta x_{\hat{n} \times \hat{b}}}{\Delta L_c}, \tag{120}$$

where $\Delta x_{\hat{n} \times \hat{b}}$ is the binormal displacement between two intersections of consecutive revolutions around the torus with arclength ΔL_c where the sum $\sum_{i=1}^N \Delta L_c^{(i)} = L_c$ is taken up to the number of revolutions N of the field line from target to target. If the field line is normal to the poloidal

cross-sectional surface, the contribution from the parallel component of the heat flux in the radial direction is exactly zero. However, if the field line has a small angle from the normal of the poloidal cross-section the radial component of the parallel transport is small. So, the corresponding radial component of the cross-field transport needs to be included because the magnitudes could be comparable.

Each island has a slightly different pitch angle with respect to the poloidal cross section. Therefore, the definition of Θ is an approximation to simplify the analysis and the interpretation of the results. Feng makes additional approximations for simplification:

1. The field line pitch is spatially varying, but the variation is small enough to be approximated as constant, so $\Theta \approx$ const.

2. The anomalous conductive transport represented by the transport coefficient χ_e is assumed to be constant.

3. The binormal transport is continuous.

Dividing the transport coefficients in front of the temperature gradient from Eq. 119 gives the following condition for dominant parallel transport:

$$\frac{\chi_e n_e}{\kappa_{0,e} T_e^{5/2} \Theta^2} < 1$$

$$T_e > \left(\frac{\chi_e n_e}{\kappa_{0,e} \Theta^2} \right)^{2/5} \tag{121}$$

which means that for low-temperature regions the cross-field transport will compete or even dominate the radial transport [4]. The condition captures the transport properties of the SOL region close to the targets. Consequently, the SOL should be split up in regions where parallel transport dominates, parallel and perpendicular transport is competing and perpendicular transport dominates [52].

The condition on transport regime can also be expressed for the field line pitch Θ:

$$\Theta > \left(\frac{\chi_e n_e}{\kappa_{0,e} T_e^{5/2}} \right)^{1/2}, \tag{122}$$

assuming that the field line pitch is spatially varying. This condition indicates which magnetic field configuration that belongs to which transport regime. Ideally, this condition can be used as a measure for choosing a magnetic configuration that enforces a transport regime with desired energy transport properties as it determines the L_c footprint on the targets.

3.3   Validity of Lengyel model based on SOLPS simulations

Two SOL energy transport models have been introduced in the previous subsections. This subsection will present a framework for assessing the validity of the assumptions made in the Lengyel model. The analysis done in this thesis is based on the framework presented by Moulton.

Moulton et al. (2019) compares the Lengyel model to SOL plasma solver (SOLPS) simulations for a physics gain factor $Q = (P_{\text{out}} - P_{\text{in}})/P_{\text{in}} = 10$ ITER scenario with neon-seeded plasmas [9, 5]. Thus, this simulation mimics the behaviour of operating a plasma that gains 10 times more energy than put in, and that extrinsic impurity radiation is obtained by injecting neon. The paper introduces a new framework for validating the Lengyel model for predicting impurity concentration needed for detachment, roughly at the temperature for which the target ion flux rolls over. Their framework is based on evaluating the heat flux equation along flux tubes, referred to as flux rings in the paper, which they argue are of most importance to the radiative volume. The flux ring is chosen based on conditions in the outer divertor as this is the limiting region with respect to the

target heat load. This corresponds to the flux ring extending up to the power width of the SOL λ_q, also known as the width of the heat flux channel [53, 54, 55]. Thus, the analysis for a flux ring of width λ_q at the rollover condition for target particle flux defining detachment onset. This definition of detachment onset corresponds to a target temperature $T_{e,\text{t}} \sim 1\text{eV}$.

The SOLPS simulations solves the following equations for the parallel heat flux density [5]:

$$B\frac{d}{ds}\left(\frac{q_\parallel}{B}\right) = \underbrace{n_e^2 c_\alpha L_\alpha^{\text{SOLPS}}}_{S_{\text{Q}_\alpha}} + S_{\text{Q}_{\text{other}}} \tag{123}$$

$$q_\parallel = \underbrace{\kappa_{e,\parallel 0,\text{FL}} T_e^{5/2} \frac{dT_e}{ds}}_{q_{\parallel,e,\text{cond}}} + q_{\parallel,\text{other}} \tag{124}$$

$$q_{\parallel,\text{other}} = q_{\parallel,e,\text{conv}} + q_{\parallel,i,\text{cond}} + q_{\parallel,i,\text{conv}} \tag{125}$$

$$S_{\text{Q}_\alpha} = n_e^2 \sum_{Z=0}^{Z_{0,\alpha}} \frac{n_{\alpha_Z}}{n_e} L_\alpha^{\text{SOLPS}} \tag{126}$$

$$L_\alpha^{\text{SOLPS}} = \sum_{Z=0}^{Z_{0,\alpha}} F_{\alpha_Z}^{\text{SOLPS}} \eta_{\alpha_Z}^{\text{STRAHL}} \tag{127}$$

$$F_{\alpha_Z}^{\text{SOLPS}} = \frac{n_{\alpha_Z}}{\sum_{Z=0}^{Z_{0,\alpha}} n_{\alpha_Z}} \tag{128}$$

$$S_{\text{Q}_{\text{other}}} = S_{\text{Q}_{\text{neut}}} + S_{\text{Q}_{\text{RT}}} \tag{129}$$

$$\tag{130}$$

Eq. 123 is the full SOLPS equation for the parallel heat flux density and describes the balance between the heat flux density on the LHS and the sources and sinks on the RHS. The LHS accounts for dilution due to flux expansion in the parallel direction. The first term on the RHS is the energy loss due to impurity radiation and the second term represents the loss due to all other energy loss mechanisms. Eq. 124 represents all the parallel heat flux density terms, and is divided into the electron conductive transport and the other terms given in Eq. 125. The subscript FL of the conductivity coefficient stand for flux-limiting which limits the conductive heat flux to convective free-streaming electrons at sound speed c_s. The impurity radiation loss is assumed to come from a primary impurity radiator of species α. The concentration of the primary impurity radiator $c_\alpha = \sum_{Z=0}^{Z_{0,\alpha}} n_{\alpha_Z}/n_e$ in Eq. 126. The sum is over all charge states Z of species α up to the charge state where the ion is stripped of electrons $Z_{0,\alpha}$. The radiated power loss function function from SOLPS is defined in Eq. 127 where $F_{\alpha_Z}^{\text{SOLPS}}$ is the fractional abundance of α_Z defined in Eq. 128 which includes transport effects. $\eta_{\alpha_Z}^{\text{STRAHL}}$ is the cooling rate coefficient for α_Z, from the STRAHL dataset, including line radiation , recombination, bremsstrahlung and ionisation cost [56]. The second term in Eq. 123 defined in Eq. 129 represents the energy loss due to interaction between the plasma and the deuterium neutrals $S_{\text{Q}_{\text{neut}}}$ and net radial energy flux out of the considered flux tube $S_{\text{Q}_{\text{RT}}}$ (RT - radial transport).

3.3.1 Integral terms

After establishing the terms included in the local energy balance Eq. 123 and 124 are combined and integrated to obtain an expression for the heat flux density at the end of the flux tube by the same treatment as Lengyel has done in Eq. 113:

$$q_{\parallel,\text{t}} = \left(q_{\parallel,\text{u}}^2 - 2\int_t^u \kappa_{e,\parallel 0,\text{FL}} T_e^{5/2} n_e^2 c_\alpha L_\alpha^{\text{SOLPS}} dT_e + 2t_B - 2t_{\text{other}}\right)^{1/2} \tag{131}$$

$$t_B = \int_t^u B\frac{d}{ds}\left(\frac{q_\parallel}{B}\right) - \int_t^u q_\parallel dq_\parallel \tag{132}$$

$$t_{\text{other}} = \int_t^u B q_{\parallel,\text{other}} d\left(\frac{q_\parallel}{B}\right) + \int_t^u \kappa_{e,\parallel 0,\text{FL}} T_e^{5/2} S_{\text{Q}_{\text{other}}} dT_e \tag{133}$$

Eq. 131 is the solution of the Lengyel integral from target to upstream conditions expressed in terms of the heat flux density at the target end of the flux tube. Eq. 132 accounts for the variation in the magnetic field strength along the field line where $t_B = 0$ if $B = \text{const}$. Eq. 133 accounts for the energy loss other than Ne radiation along the flux tube, which is net radial transport and plasma-neutral interaction, parallel convective and ion conductive transport.

3.3.2 Lengyel model solution in Moulton analysis

The following set of equations gives a self-contained solution of the integral along the flux tube from upstream u to target t:

$$q_{\parallel,\text{t}} = \left(q_{\parallel,\text{u}}^2 - 2\kappa_{\text{e},\parallel 0,\text{FL}} n_{\text{e},\text{u}}^2 T_{\text{e},\text{u}}^2 c_\alpha \int_t^u T_e^{1/2} L_\alpha^{n_e \tau} dT_e \right)^{1/2} \tag{134}$$

$$q_{\parallel,\text{t}} = \gamma (n_{\text{e},\text{u}} T_{\text{e},\text{u}}/2)\sqrt{2T_{\text{e},\text{t}}/m_i} \tag{135}$$

$$L_\parallel = \kappa_{\text{e},\parallel 0,\text{FL}} \int_t^u T_e^{5/2} q_\parallel(T_e) dT_e \tag{136}$$

where γ is the sheath transmission coefficient [8]. The following assumptions have been made for Eq. 134-136:

1. $\kappa_{\text{e},\parallel 0,\text{FL}}, B$, and c_α are constant along the flux tube. A constant B along the flux tube means no energy dilution because the variation of the magnetic field strength along the flux tube is zero. The temperature-independent conductivity $\kappa_{\text{e},\parallel 0,\text{FL}}$ can be assumed constant as it does not change much along the divertor leg. Assuming constant impurity concentration c_α means that the variation is so small that using the exact impurity concentration will have no impact on the result of the integral. Thus, the conductivity coefficient and the impurity concentration can be put outside the integral in 134.

2. The electron pressure $n_e T_e$ is assumed to be constant in the radiation region, meaning it can be put outside the integral of Eq. 134 and given by the upstream value.

3. L_α^{SOLPS} represents the baseline of they radiated power loss function for which the electron cooling coefficients $\eta_{\alpha z}^{\text{STRAHL}}$ ignores electron impact deexcitation due to sufficiently low electron density. The impurity transport is approximated by calculating the fractional abundances from an ionisation balance for a population of impurity atoms exposed to a plasma at fixed n_e and T_e for a constant impurity residence time τ. This makes the radiated power loss function $L_\alpha^{n_e \tau}(T_e)$ only dependent on the electron temperature avoiding resolving the expression for coupled quantities.

4. The net radial transport and energy loss due to plasma-neutral interaction is negligible, so $q_{\parallel,\text{other}} = 0$ and $S_{\text{other}} = 0$.

5. The ion and electron temperatures at the target are equal $T_{i,\text{t}} = T_{e,\text{t}}$.

6. The heat flux density at the target is transmitted through the sheath with transmission coefficient γ as given in the Bohm criterion [8].

3.3.3 Framework for comparison with the Lengyel model

The focus of the paper by Moulton et al. (2021) is to review how the simplification of the SOL physics model, required to derive a scaling of the radiation, affects the quality of the prediction of the impurity concentration needed for detachment. Starting with the complex model given by the SOLPS equations the validity of the assumptions used in the Lengyel model is investigated by sequentially removing terms according to the following steps:

1. The integral is evaluated for quantities computed using the complete SOLPS model which is to be used as a baseline for comparison with simplified expressions.

2. The impurity concentration is approximated by the average impurity concentration in the divertor $\langle c_\alpha \rangle_{\text{div}}$ at detachment given by:

$$\langle c_\alpha \rangle_{\text{div}} \approx \frac{\frac{1}{2}(q_{\parallel,\text{u}}^2 - q_{\parallel,\text{t}}^2) + t_B - t_{\text{other}}}{\int_t^u \kappa_{\text{e},\parallel 0,\text{FL}} T_e^{5/2} n_e^2 L_\alpha^{\text{SOLPS}} dT_e} \tag{137}$$

3. The terms related to other heat flux mechanisms (convective and ion conduction) as well as other energy losses other than impurity radiation (net radial transport + plasma-neutral interactions) given by t_{other} is removed:

$$\langle c_\alpha \rangle_{\text{div}} \approx \frac{\frac{1}{2}(q_{\parallel,\text{u}}^2 - q_{\parallel,\text{t}}^2) + t_B}{\int_t^u \kappa_{\text{e},\parallel 0,\text{FL}} T_e^{5/2} n_e^2 L_\alpha^{\text{SOLPS}} dT_e}. \tag{138}$$

4. The energy loss due to variation in the magnetic field strength given by t_B is removed because the magnetic field strength along the divertor leg is approximately constant:

$$\langle c_\alpha \rangle_{\text{div}} \approx \frac{\frac{1}{2}(q_{\parallel,\text{u}}^2 - q_{\parallel,\text{t}}^2)}{\int_t^u \kappa_{\text{e},\parallel 0,\text{FL}} T_e^{5/2} n_e^2 L_\alpha^{\text{SOLPS}} dT_e}. \tag{139}$$

5. The static pressure $p_e = n_e T_e$ is assumed constant over the integration domain and brought outside the integral:

$$\langle c_\alpha \rangle_{\text{div}} \approx \frac{\frac{1}{2}(q_{\parallel,\text{u}}^2 - q_{\parallel,\text{t}}^2)}{n_{e,\text{u}}^2 T_{e,\text{u}}^2 \int_t^u \kappa_{\text{e},\parallel 0,\text{FL}} L_\alpha^{\text{SOLPS}} dT_e}. \tag{140}$$

6. The SOLPS radiated power loss function L_Z^{SOLPS} is replaced with $L_Z^{n_e \tau}$ assuming constant $n_e \tau$. Thus, the radiation power loss function only depends on the electron temperature T_e:

$$\langle c_\alpha \rangle_{\text{div}} \approx \frac{\frac{1}{2}(q_{\parallel,\text{u}}^2 - q_{\parallel,\text{t}}^2)}{n_{\text{e},\text{u}}^2 T_{\text{e},\text{u}}^2 \int_t^u \kappa_{\text{e},\parallel 0,\text{FL}} L_\alpha^{n_e \tau}(T_e) dT_e}. \tag{141}$$

7. The simplified Lengyel model is applied where the upper electron temperature boundary is approximated by the two-point model (2PM) and the lower boundary is set to zero [8]. The electron conduction coefficient $\kappa_{\text{e},\parallel 0,\text{FL}}$ is approximated as constant and taken to be the average value over the divertor leg. Thus, the set of equations with boundary conditions from the 2PM are:

$$c_{\text{Ne}} = \frac{q_{\parallel,\text{u}}^2/2}{\langle \kappa_{\text{e},\parallel 0,\text{FL}} \rangle n_{\text{e},\text{u}}^2 T_{\text{e},\text{u}}^2 \int_0^u L_\alpha^{n_e \tau} \sqrt{T_e} dT_e} \tag{142}$$

$$T_{\text{e},\text{u}} = T_{\text{e},\text{u}}^{2PM} = \frac{7}{2}\left(\frac{q_{\parallel,\text{u}} L_\parallel}{\langle \kappa_{\text{e},\parallel 0,\text{FL}} \rangle}\right)^{2/7}, \tag{143}$$

where Eq. 143 is the 2PM upstream temperature for zero target temperature $T_{e,\text{t}} = 0$ eV.

3.3.4 Relevant results and conclusions
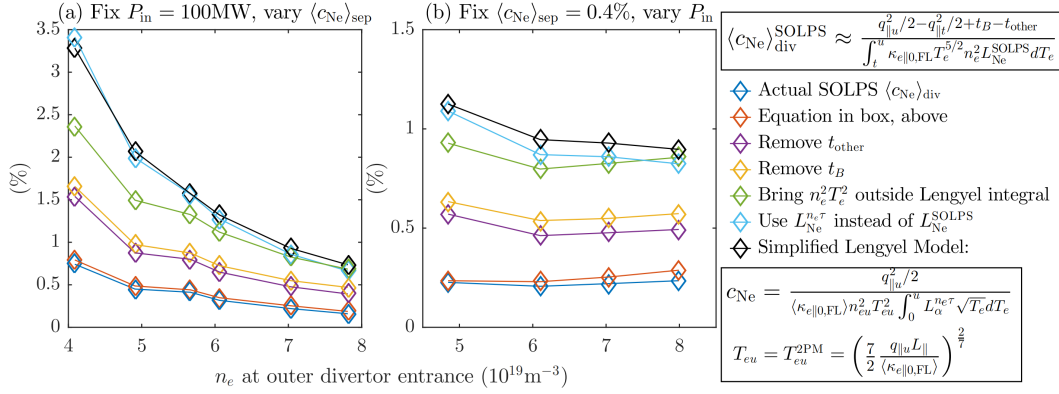
Figure 26: Then main result of the paper following the sequential removal of terms given in framework of Moulton et al. (2019). Source: [5].

The paper's main result is shown in Fig. 26 where the sequential removal of terms as described in the framework have been applied in the prediction of the impurity concentration in the divertor needed for detachment. The simplified Lengyel model is consistently conservative in predicting the impurity concentration needed for detachment. The following is worth noting for comparison with the results later on in the thesis:

1. The difference between the actual SOLPS simulation of the average divertor concentration (average taken along the flux ring) is minimal with respect to the approximation given in Eq. 137.

2. Removing the term representing the energy loss along the flux tube due to net radial transport and plasma-neutral interactions predict to increase by a factor of 2.

3. The concentration prediction almost doubles when constant pressure along the flux tube is assumed.

4. For the flux ring of interest the approximation of constant impurity residence time τ barely affects the concentration prediction.

Thus, the results tell us that the assumption of constant pressure along a flux tube and negligible net radial transport and energy loss due to plasma-neutral interaction needs further investigation as it indicates that the assumptions are invalid. Furthermore, the assumptions on negligible energy loss due to variation in the magnetic field strength and constant residence time for the impurity transport modeling seem to be valid. For the latter, it is the integral $\int_t^u \sqrt{T_e} L_Z(T_e) dT_e$ that is important. Thus, the local differences between the radiation loss profiles computed by SOLPS and the one assuming constant residence time are of less concern for the contribution to the heat load on the target as long as the local variations are cancelled out by integration. This means that this assumption can capture the integrated tendency of the radiative power loss, but cannot be used for local analysis.

3.4 Global energy transport analysis in W7-X

Feng et al. (2021) describes the behaviour of the island divertor in W7-X at detachment based on simulation results from EMC3-EIRENE [40, 38, 4, 1]. The simulation cases were made to match discharges for which validated experimental data exists. In the paper, a global analysis of the energy transport has been carried out with respect to the total heat load on the target and the unloading due to impurity radiation at detachment. The results of the simulations for high

total radiated power fraction f_{rad} cases show a homogeneously thermal unloading of the targets by impurity line radiation. The radiation is distributed over a broad poloidal surface area and is helically continuous. This results in a cooling layer at the edge with large area coverage supporting the discovery of the homogeneity of the thermal unloading of the targets. Furthermore, the heat flux mechanisms are studied in detail. It is shown that both classical heat conduction and cross-field transport play a significant role in the energy transport from the LCFS radially outwards to the targets.

3.4.1 Supportive experimental results
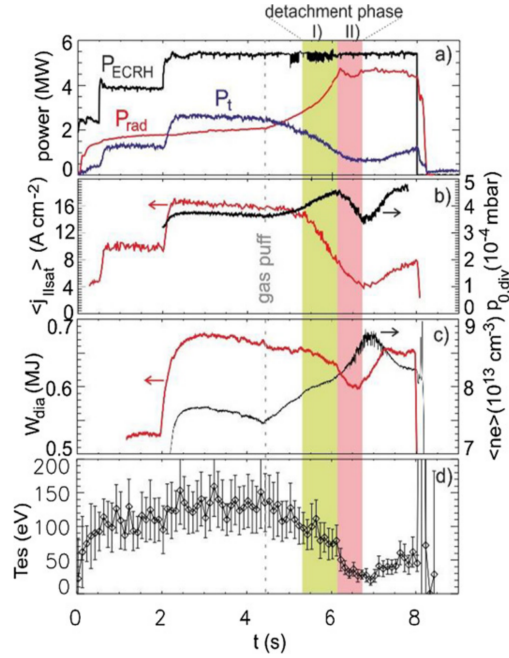
Figure 27: The main experimental results that is used to set the parameters of the simulation cases in Feng et al. (2021). Source: [1].

Fig. 27 shows a typical experiment of a detached scenario with the W7-X island divertor in the standard configuration. The detachment window corresponding to the yellow and red shaded areas in Fig. 27 can be divided into two phases. In phase I the total radiative power P_{rad} builds up and after the gas puff the total target heat flux drops by an order of magnitude. The change in core-related parameters like the edge electron temperature T_{es}, the line averaged density $\langle n_e \rangle$ and the plasma stored energy W_{dia} for $f_{\mathrm{rad}} \geq 0.8$ can be associated with radiated power levels beyond a critical level. Critical radiation levels in the core eventually leads to the breakdown of the stored energy in the plasma. This event is outside the scope of this thesis. Thus, the rest of the description of the plasma from Feng et al. (2021) given in this thesis will only concern phase I.

3.4.2 Energy transport equations

The local energy balance used for the energy transport in Feng's paper is the equations used in the EMC3 code given by Eqs. 56 and 57. Integrating the equations over the SOL volume gives the radial 1D power balance in the SOL given in Eq. 19. However, for the computational domain used in in the EMC3-EIRENE simulations the radially dependent heat flux terms are defined as

follows:

$$Q_{\perp,\text{cond}}(r) = \iint_r (-\chi_e n \nabla_\perp T_e - \chi_i n \nabla_\perp T_i) \cdot d\boldsymbol{s} \tag{144}$$

$$Q_{\parallel,\text{cond}}(r) = \iint_\phi \left(-\kappa_e T_e^{5/2} \nabla_\parallel T_e - \kappa_i T_i^{5/2} \nabla_\parallel T_i \right) \cdot d\boldsymbol{s} \tag{145}$$

$$Q_{\text{conv}}(r) = \iint_\phi \left[\frac{5}{2} n(T_e + T_i) v_{\parallel,i} \right] \boldsymbol{b} \cdot d\boldsymbol{s} - \iint_r \left[\frac{5}{2} D_\perp (T_e + T_i) \nabla_\perp n \right] \cdot d\boldsymbol{s} \tag{146}$$

$$Q_{\text{imp}}(r) = \iiint_r R_{\text{imp}} dV \tag{147}$$

$$Q_{\text{neutral}}(r) = - \iiint_r (S_{\text{ee}} + S_{\text{ei}}) dV \tag{148}$$

$$Q_t(r) = \iint_t n(\gamma_e T_e + \gamma_i T_i) c_s \boldsymbol{b} \cdot d\boldsymbol{s} \tag{149}$$

where $\iint_r (\cdot) \cdot d\boldsymbol{s}$ means integration over a radially-oriented surface. The integration $\iint_\phi (\cdot) \cdot d\boldsymbol{s}$ is over a toroidally oriented surface of the radially projected parallel term $(\cdot)$. The volume integral $\iiint_r (\cdot) dV$ and $\iint_t (\cdot) \cdot d\boldsymbol{s}$ means the integration over the target surface. All radially dependent heat flux terms are integrated cumulatively up to r. Feng has a different grid than the one used for the simulations in this thesis. The main difference is that Feng's grid does not resolve the X-points, but consists of nested surfaces as described in 2 that is more aligned with the flux surfaces of the confined region. Feng's grid gives a radial direction from the grid surfaces that varies less than the grid used in this thesis. Feng's choice of shape of the grid surfaces simplifies the interpretation and computation of the global energy transport. However, it comes at the cost of not resolving the transport in the region around the X-points.

$Q_{\perp,\text{cond}}$ is the total perpendicular conductive heat flux of electrons and ions going out from grid surfaces oriented in the radial direction. Q_{conv} is the total convective heat flux including both perpendicular and parallel terms. The radial component of the parallel term is computed similarly to the parallel conductive heat flux. Q_{neutral} is the cumulative radially dependent energy loss due to plasma-neutral interaction that includes the contribution of the ionization potential energy released during surface recombination processes. Q_{imp} is the cumulative radially dependent energy loss due to impurity radiation, and Q_t is the cumulative radially dependent power loss to the target.

3.4.3 Results of detachment simulations
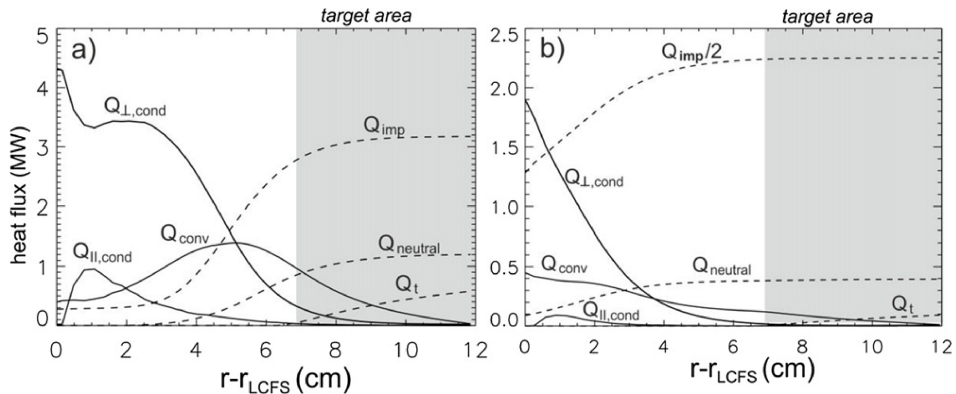
Figure 28: Radially depending heat flux for simulations with a) $f_{\text{imp}} = 0.64$ and b) $f_{\text{rad}} = 0.9$. Note that the scale is reduced in b) and that the heat flux from the impurity radiation Q_{rad} is divided by 2. Fort both plots the sum of all terms corresponds to the SOL input power $P_{\text{SOL}} = 5[\text{MW}]$. Source: [1].

The results of Feng's simulations show the following:

1. The homogeneity of the unloading of the target heat loads is increased because the radiation is better distributed for higher radiative powers. At high radiated power fraction the radiation is well distributed poloidally and toroidally, making a continuous surface resulting in homogeneous unloading of the targets.

2. Parallel conduction is a small contribution to the total energy balance throughout the SOL.

3. Perpendicular conductive transport is significant out to a distance from the LCFS where convective transport becomes largest.

4. The convective transport peaks close to the ionization front of the hydrogen neutrals. As the neutral penetration depth increase with higher radiated power fraction the peak of the convective flow moves inwards towards the LCFS.

5. For increasingly high radiative power fractions the radiation front moves inwards almost towards the LCFS as shown in Fig. 29. The tendency agrees with the experimental data shown in Fig. 27 where the slope of the stored energy and edge temperature suddenly drops when the radiative power saturates for which the radiation front has passed the LCFS.
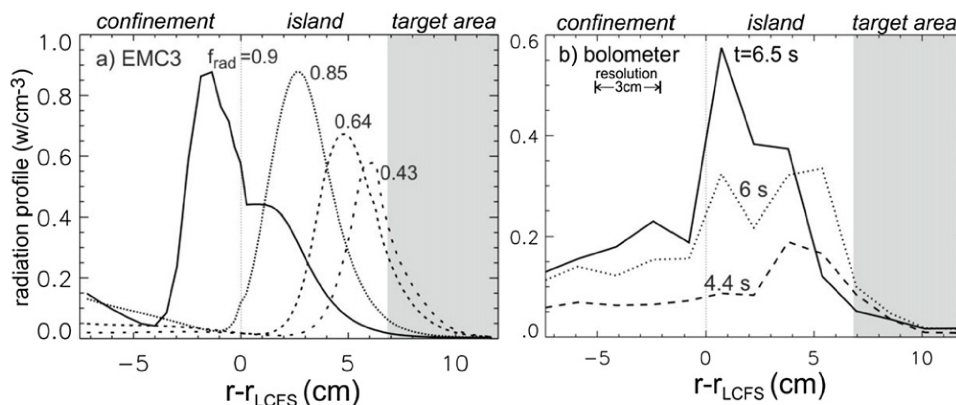
Figure 29: The calculated a) and reconstructed (from the bolometer measurement of the discharge shown in Fig. 27) b) radiation distribution during detachment is shown for cases with different total radiative power fraction f_{rad}. The effective radius is shown on the horizontal axis where the effective radius in a) has been approximated as the cylindrical average of each radial surface in the computational mesh and the effective radius in b) denotes the closed surfaces linearly extrapolated from the LCFS in a triangular cross-section. The top horizontal axes indicate the different regions (confinement, SOL, target area). Source: [1].

Items 4 and 5 in the list of Feng's results are not shown explicitly in the Feng et al. (2021 [1]), but are spread across many papers [38, 57, 4]. The results from the simulations only motivate their validity within the frames of the physics model of the code. Since the target unloading is observed to be homogeneous, the field lines in this thesis's analysis can be chosen to be traced from the same locations at the target regardless of the radiated power boundary condition. Furthermore, the shown insignificance of the parallel electron conductive heat flux density already indicate the invalid assumption in Lengyel's model. However, this can be locally dependent and needs to be confirmed for profiles along the field line. Feng's results indicate that the power loss from cross-field transport and to the convective channels is significant. The convective transport can be very important for large radiated power fractions as it peaks at the ionisation front, correlated with the radiation front's location.

In this section the simplified models for the energy transport in the SOL was presented. Furthermore, Moulton et al. did a validity assessment of the Lengyel model for SOLPS $Q = 10$ neon seeded simulations, giving insight into the most severe assumptions about the energy transport at detachment onset [5]. The results of the EMC3-EIRENE simulations of the energy transport in the island divertor SOL will be presented and discussed in the next section.

4 Assessment of Lengyel model in stellarator ID

In this section the result of the analysis of the EMC3 simulations will be shown first for the global energy balance as defined in 2 in Eq. 19 complemented with the radial projection of the cross-field heat flux density terms. This demonstrates consistency with the previous work by Feng [38, 57, 4, 52, 1].

Second, the field line profiles of the terms in the field line integral from Eq. 52 and the contributions from each integral term given in Eqs. 46-51 for each field line will be computed and discussed. *Since most of the heat load in the standard configuration is deposited on the upper horizontal target, and to limit the discussion, the results presented in this thesis are only associated with the upper horizontal target (low iota target).* The analysis intends to compare the ratio of the magnitude of the transport integral terms with respect to the results from Moulton et al. (2021) [5]. The ratio between parallel and perpendicular transport terms is crucial to establish before simplifying the LHS of Eq. 14 by making an assumption on the heat flux density terms.

Third, the impurity concentration was predicted following the list of imposed assumptions given in Eqs. 91-99 using Eq. 90 as a baseline. The impurity concentration profiles and their upstream to target average for each field line will be shown for comparison with the predictions by Eqs. 91-99. This will indicate whether the concentration prediction can be used as a conservative estimate of the required concentration for a desired f_{rad}.

4.1 Global energy transport analysis

The global power balance is given in Fig. 30 and 31 for cases with radiative power fraction $f_{\mathrm{rad}} = 0.2$ and $f_{\mathrm{rad}} = 0.8$, respectively. The heat flux terms have been computed as described in section 2. All components have been plotted in of Fig. 30 along with the sum of all the terms. The grey dashed lines in Figs. 30 and 31 represents the approximate radial distance from the LCFS to the X-points as described in section 2 and the poloidal and toroidal averaged temperature at the radial grid surface intersecting the X-points, respectively. The location of the lines indicating the X-points were determined by averaging a radial grid surface over the poloidal and toroidal indices. The radial index was chosen by inspection of the location of the grid surface with respect to the X-points. The dashed black line represents the region where the plasma starts interacting with the targets. The location of the black line was chosen by inspection at the first intersection between the grid surface at a constant radial grid index and the divertor targets in the first poloidal cross section the targets and the grid surface cross.
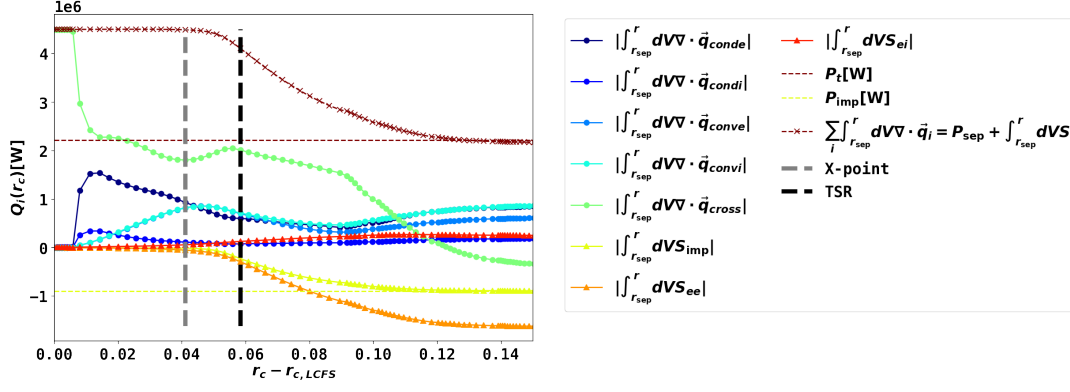
(.1) The global power balance is shown for radiative power fraction $f_{\rm rad} = 0.2$
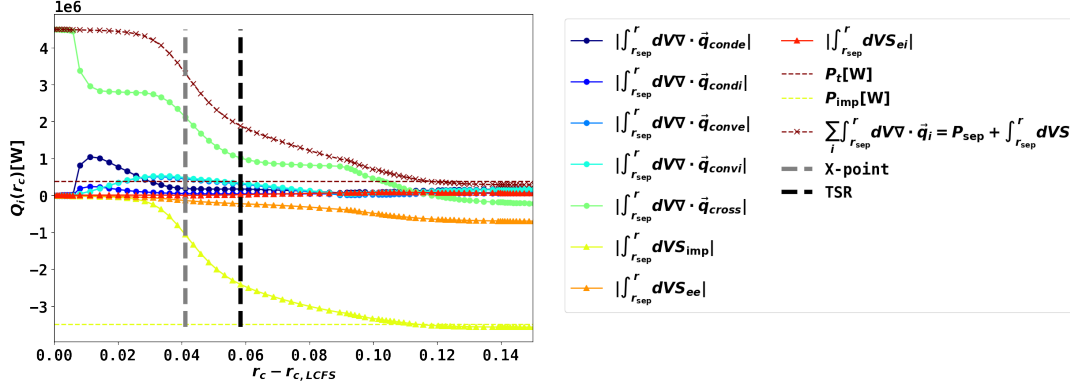
(.2) The global power balance is shown for radiative power fraction $f_{\rm rad} = 0.8$.

Figure 30: The global power balance is shown as the integrated heat flux cumulatively up to radial index i_r. The sum of all the terms $\sum_i \int_{r_{\rm sep}}^{r} dV \nabla \cdot \vec{q}_i = P_{\rm sep} + \int_{r_{\rm sep}}^{r} dV S$ relaxes to the value of the target heat flux. The symbol for impurity radiation intensity is $S_{\rm imp}$ and the total impurity radiation is $P_{\rm imp}$. The plasma-neutral interaction sources and sinks due to electron impact is given by $S_{\rm ee}$ and ion impact by $S_{\rm ei}$. The symbol for total power loss to the target is P_t.

The interpretation of the integrals shown in Figs. 30 and 31 is the cumulative sum from the grid surface representing the LCFS up to a surface at a given i_r of the heat flux difference $dQ(i_r) = [\sum_i \nabla \cdot \boldsymbol{q}_i dV](i_r)$ between the inner and outer radial surface of a toroidal shell of volume $\sum_{i_\theta, i_\phi} dV(i_r, i_\theta, i_\phi)$ defined at a radial grid index i_r. It is clear from Figs. 30 and 31 that there is global power balance for both simulation cases. This is shown by the convergence of the sum of all the heat flux terms to the target heat flux. The sum of the heat flux terms is equivalent with the sum of the power at separatrix $P_{\rm sep}$ and the effective energy loss $\int_{r_{\rm sep}}^{r} dV S$ which is Eq. 19 expressed in terms of the heat flux for a given radius $Q(r)$. Furthermore, the total radiation loss $P_{\rm imp} = \int_{r_{\rm sep}}^{r} dV S_{\rm imp}$ converges to the value given in radiation boundary condition as it is supposed to.
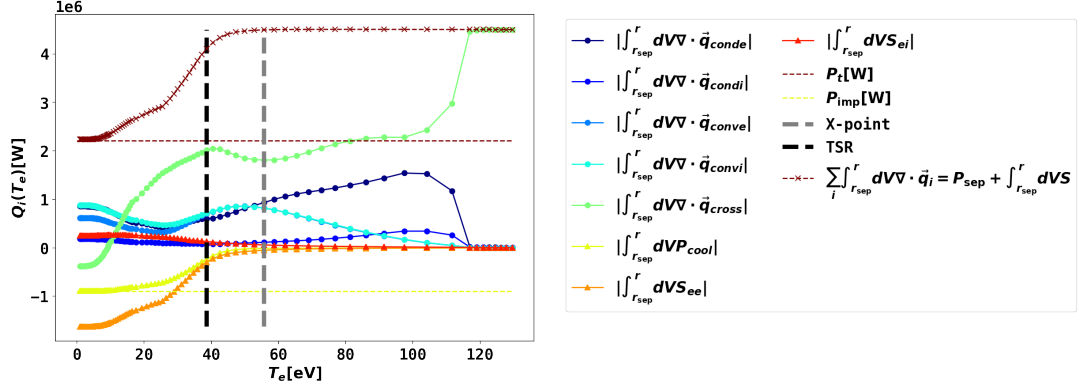
Legend:
- $|\int_{r_{\mathrm{sep}}}^{r} dV \nabla \cdot \vec{q}_{conde}|$
- $|\int_{r_{\mathrm{sep}}}^{r} dV \nabla \cdot \vec{q}_{condi}|$
- $|\int_{r_{\mathrm{sep}}}^{r} dV \nabla \cdot \vec{q}_{conve}|$
- $|\int_{r_{\mathrm{sep}}}^{r} dV \nabla \cdot \vec{q}_{convi}|$
- $|\int_{r_{\mathrm{sep}}}^{r} dV \nabla \cdot \vec{q}_{cross}|$
- $|\int_{r_{\mathrm{sep}}}^{r} dV P_{cool}|$
- $|\int_{r_{\mathrm{sep}}}^{r} dV S_{ee}|$
- $|\int_{r_{\mathrm{sep}}}^{r} dV S_{ei}|$
- P_t[W]
- P_{imp}[W]
- X-point
- TSR
- $\sum_i \int_{r_{\mathrm{sep}}}^{r} dV \nabla \cdot \vec{q}_i = P_{\mathrm{sep}} + \int_{r_{\mathrm{sep}}}^{r} dVS$

(.1) The global power balance is shown for radiative power fraction $f_{\mathrm{rad}} = 0.2$
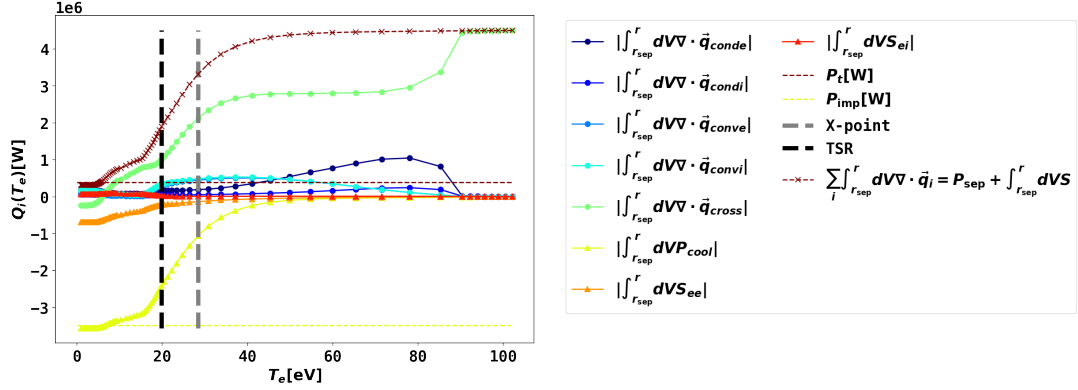
(.2) The global power balance is shown for radiative power fraction $f_{\mathrm{rad}} = 0.8$.

Figure 31: The global power balance is shown as the cumulative integral of the net heat flux of a radial shell up to radial index i_r. The sum of all the terms is $\sum_i \int_{r_{\mathrm{sep}}}^{r} dV \nabla \cdot \vec{q}_i = P_{\mathrm{sep}} + \int_{r_{\mathrm{sep}}}^{r} dVS$. The horizontal axis is represented by the electron temperature T_e in eV. The symbol for impurity radiation intensity is S_{imp} and the total impurity radiation is P_{imp}. The plasma-neutral interaction sources and sinks due to electron impact is given by S_{ee} and ion impact by S_{ei}. The symbol for total power loss to the target is P_t.

The tendencies of the global power balance agrees with the corresponding results presented in Feng et al. (2021) [1]. In both cases the cross-field transport dominates. Furthermore, the region from the X-points to the target region shows a larger change in the cross-field transport and parallel electron conductive transport for $f_{\mathrm{rad}} = 0.8$ compared to the $f_{\mathrm{rad}} = 0.2$ case due to a stronger drop in the temperature. The temperature drops more in the high radiation case because increased radiation implies a stronger temperature reduction in the radiative volume. Due to the inwards movement of the ionization front the parallel convective term overtakes the parallel electron conductive term before crossing the X-points. Furthermore, the parallel convective heat flux for ions and electrons have approximately the same magnitude. Moreover, in the low radiation case the energy losses are dominated by the neutral interactions due to electron impact, but the role changes with the radiation losses when the radiated power fraction is increased to $f_{\mathrm{rad}} = 0.8$. This implies that there is a transition at some radiated power fraction between $f_{\mathrm{rad}} = 0.2$ and $f_{\mathrm{rad}} = 0.8$ where the impurity radiation loss becomes greater than the neutral losses. In both cases the observed energy loss from the neutral interactions due to ion impact and the parallel ion conductive transport is insignificant. The latter is expected as the electron conductivity is larger than the ion conductivity due to the $m_i^{-1/2}$ dependence of the conductivity coefficient [42, 8].

4.1.1 Radial projection of cross-field conductive heat flux densities

The radial projection of the conductive cross-field heat flux densities was computed as described in section 2. The targets and the island structure are included in Figs. 32 and 33 by black lines and a red Poincaré plot in grid index space (i_r, i_θ), respectively. The conductive cross-field heat flux densities are plotted against the radial and poloidal grid indices for interpretation because they are homogeneously distributed. The cross-field heat flux densities starts at the LCFS given by the same radial index as the inner boundary for the global power balance ($i_r = 20$). Note that the cross-field heat flux densities are approximated by the radial gradients of the density and the temperature fields. The magnitude of the approximated cross-field heat flux densities agrees with the magnitude of experimental measurements [35].
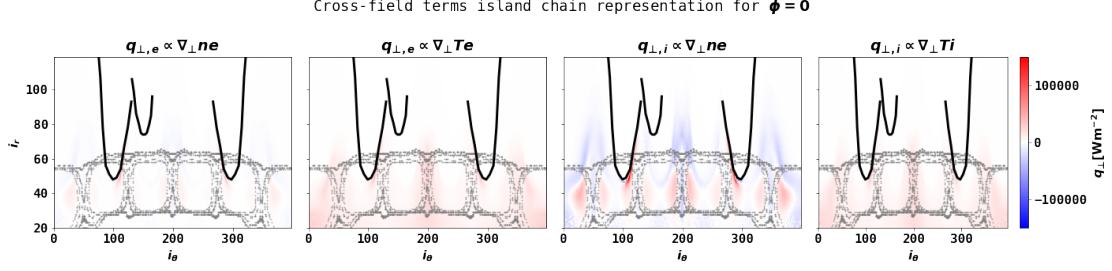
(.1) The radial projection of the decomposed cross-field heat flux densities at $\phi = 0°$.
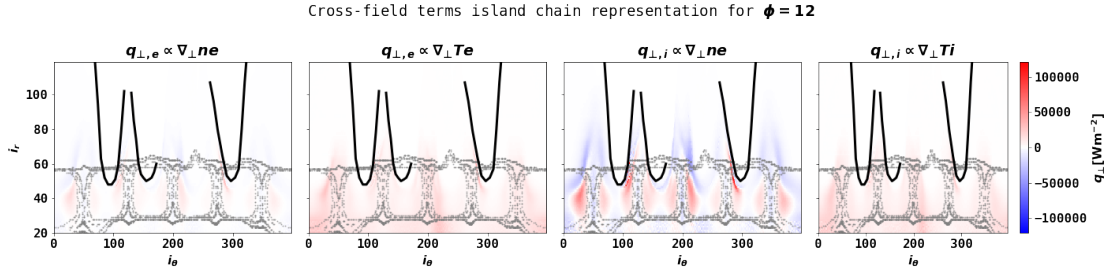
(.2) The radial projection of the decomposed cross-field heat flux densities at $\phi = 12°$.
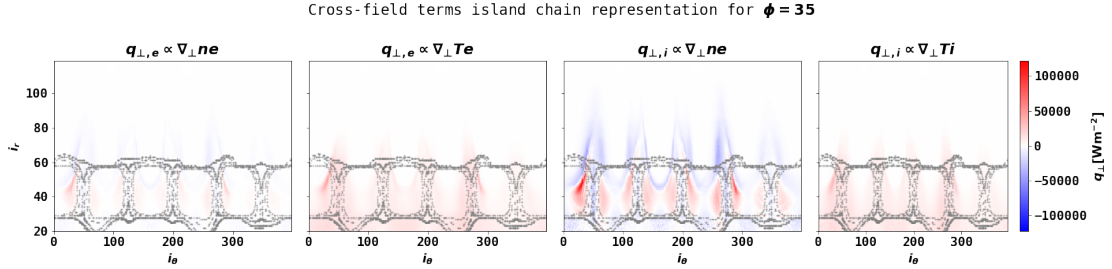
(.3) The radial projection of the decomposed cross-field heat flux densities at $\phi = 35°$.

Figure 32: The radial projection of the cross field heat flux densities at toroidal angles $\phi = \{0°, 12°, 35°\}$ for the $f_{\text{rad}} = 0.2$ case. The islands structure is indicate by the grey Poincaré plot and the targets by the black lines. The horizontal axis is given by the poloidal grid indices i_θ and and the vertical axis is given by the radial grid indices i_r.

The plots in Fig. 32 shows the conductive cross-field heat flux density components for the low radiation case with $f_{\text{rad}} = 0.2$. It exhibits a clear structure with transport towards the targets (positive) strongly localised at the X-points. For the convective term this is closely followed by transport in the opposite direction (negative) located inside the island, and between the X-points and the targets. The negative transport is due to a local maximum in the density correlated with the ionization front. The correlation between the convective transport and the ionisation front will be emphasized in the next subsection on the analysis of the field line ensemble. Thus, below the X-points heat is transported back towards the confined region via cross-field convective transport.

The negative parallel convection agrees with the negative values for the cross-field term seen in the global energy balance for the low temperature region $T_e \sim 0 - 10\text{eV}$.
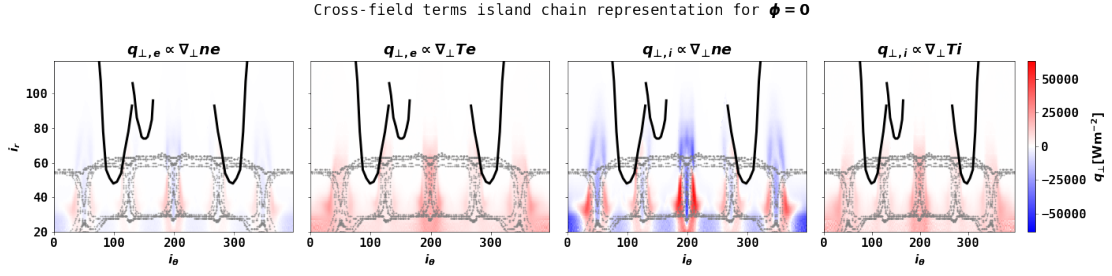
(.1) The radial projection of the decomposed cross-field heat flux densities at $\phi = 0°$.
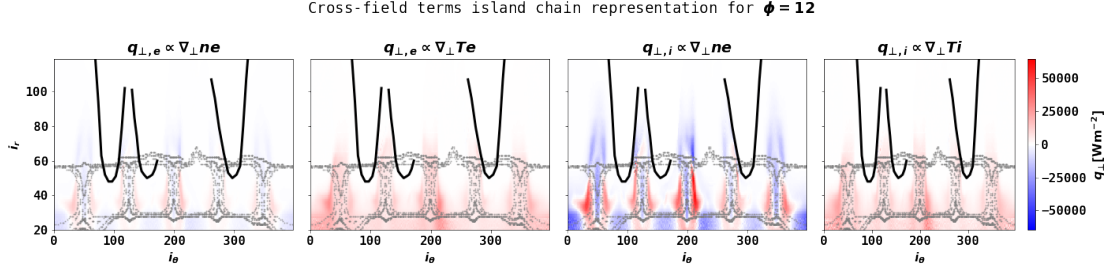
(.2) The radial projection of the decomposed cross-field heat flux densities at $\phi = 12°$.
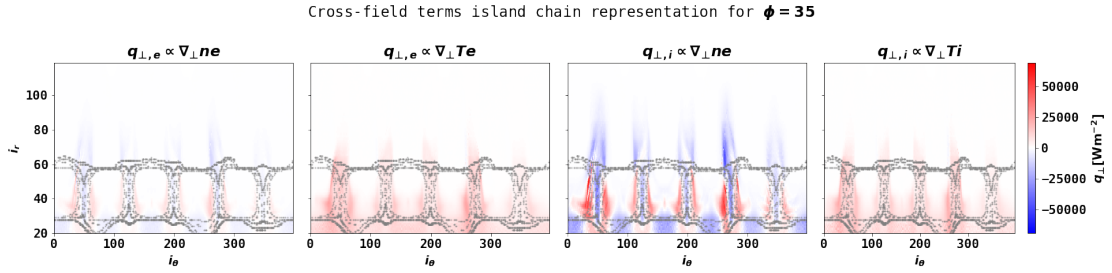
(.3) The radial projection of the decomposed cross-field heat flux densities at $\phi = 35°$.

Figure 33: The radial projection of the cross field heat flux densities at toroidal angles $\phi = \{0, 12, 35\}$ for the $f_{\text{rad}} = 0.8$ case. The islands structure is indicated by the grey Poincaré plot. The horizontal axis is given by the poloidal grid indices i_θ and and the vertical axis is given by the radial grid indices i_r.

The plots in Fig. 33 show the cross-field heat flux density components of the high radiation case with $f_{\text{rad}} = 0.8$. In both the $f_{\text{rad}} = 0.2$ and $f_{\text{rad}} = 0.8$ case the ion and electron temperature decrease from the LCFS to the targets, so the cross-field conductive terms are positive, as expected. The localisation of the heat flux densities at the X-points implies that the PFR is important. Furthermore, the concentration is larger around some X-points than others. This implies that the distribution of power to the PFR is asymmetric. An asymmetry in the power distribution around the X-points implies an asymmetry in the heat deposition on the walls. So, if the variation of the power at the X-points is large enough, the region of strongest cross-field transport will be critical to consider. The heat flux density is concentrated at the X-points around the poloidal index $i_\theta = 20$ and $i_\theta = 200$. This feature is more profound for $f_{\text{rad}} = 0.8$ than $f_{\text{rad}} = 0.2$ which can be correlated to the inwards movement of the radiation front towards the X-points. The X-point at poloidal index $i_\theta = 20$ is associated with the X-point poloidally before the island intersecting the upper horizontal target. The island around $i_\theta = 200$ is the island on the inboard side. The coloured Poincaré plot in Fig. 34 indicates the total cross-field heat flux density and the island locations.
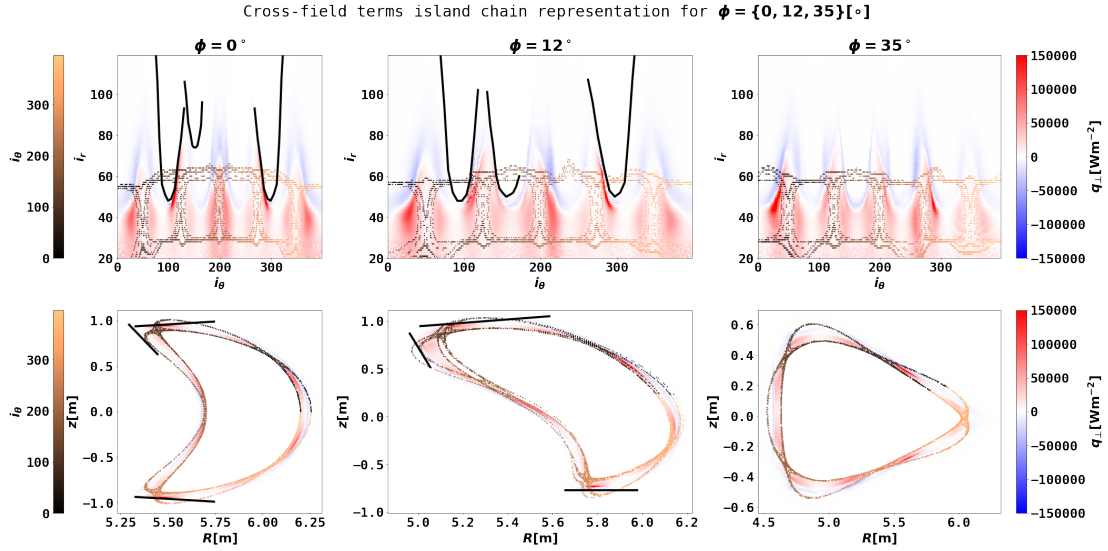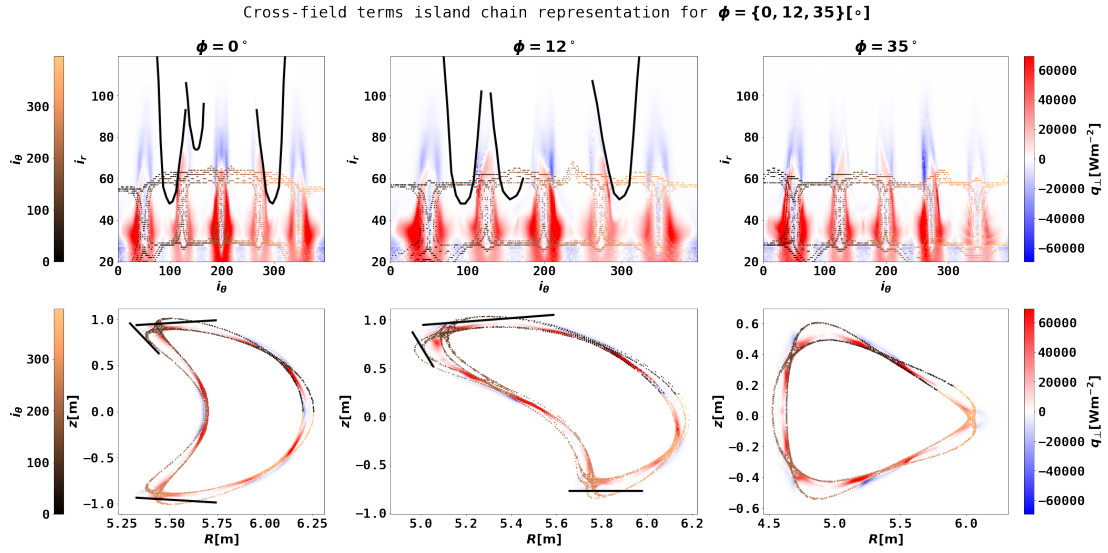
Figure 34: The total cross-field heat flux density for $f_{\rm rad} = 0.2$ and $f_{\rm rad} = 0.8$ at $\phi = \{0°, 12°, 35°\}$. The upper plots show the heat flux densities in grid index space (i_r, i_θ) and the lower plot shows the corresponding poloidal cross section. The horizontal colourbar indicates the poloidal index i_θ so that the islands in the plots above can be associated with their real space coordinates (R, z) in the plot below. The divertor targets are shown by the black lines.

A key observation is that the dominance of the cross-field convection in Fig. 34 does not appear to be in immediate agreement with Feng's results for the cross-field heat flux where cross-field conduction is larger than the cross-field convection as shown in Fig. 28. However, the approximated convective cross-field heat flux densities in Figs. 32 and 33 have significant negative values. Thus, the positive regions are reduced by the negative regions in the volume integral such that the cross-field conductive heat flux might be larger than the cross-field convective heat flux.

4.2   Local energy transport

In this subsection profiles along field lines will be presented such that the local behaviour of the plasma in the ID can be discussed and compared with the behaviour presented in sections 1 and

2. Furthermore, it intends to demonstrate the consistency between the integral terms in the impurity concentration prediction given in Eqs. 91-99 and the results from Feng et al. (2021) [1]. The stepwise simplification of the impurity concentration equation presented in section 2 will be evaluated in this subsection.

4.2.1 Ensemble of field lines in the SOL

To show the tendency of the local behaviour all field lines in the SOL in both simulation cases are shown in the same plot. The spatial location of each field line with respect to a poloidal cross-section for a toroidal angle $\phi = 2°$ is shown in Fig. 35. The magnetic islands are plotted as a Poincaré plot in grey. The profiles of the scalar and vector fields along the field lines are shown against a normalised arclength $l_\parallel / \|l_\parallel\|_\infty$.
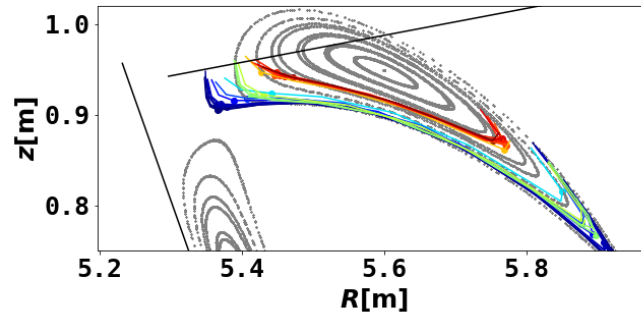
Figure 35: The field lines are projected onto the poloidal cross-section for toroidal angle $\phi = 2°$ such that the field lines can be related to their location in the island. The colour of the field line intersections are the same as used for the field lines profiles. The scatter points shows the location of the approximated X-points and are given as dashed vertical lines in the profiles along the field lines. These points were approximated by taking the index of the intersections closest to 20% and 80% of the maximum index of the intersections between the field lines and the poloidal plane at $\phi = 2°$.

To distinguish between what is referred to as the left and right part of the field line, the two parts are shown for a poloidal cross-section at $\phi = 2°$ and the $q_{\parallel\mathrm{cond},e}$-profile for $q_{\parallel\mathrm{cond},e}$ where the intersections between the field line and the poloidal plane are the white to black dots in Fig. 36
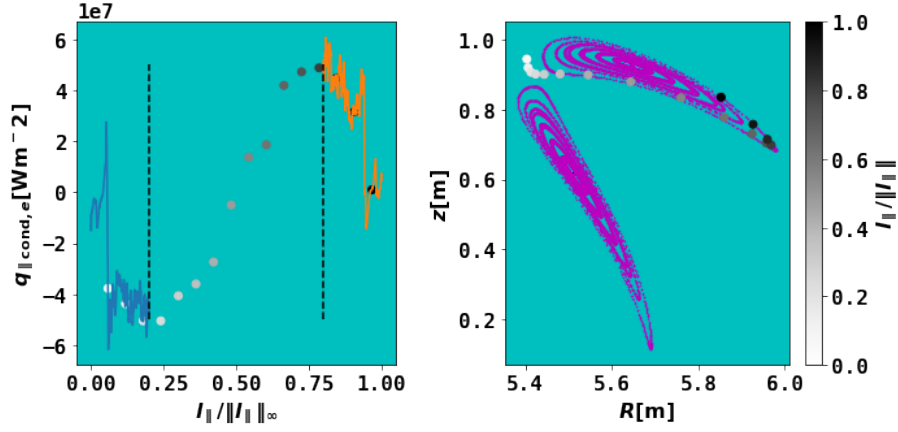
Figure 36: How the field line is split into a left ($0 \leq l_\parallel/\|l_\parallel\|_\infty \leq 0.5$) and right part ($0.5 \leq l_\parallel/\|l_\parallel\|_\infty \leq 1$) at the upstream location indicated by the dashed black line is shown. The two parts are shown for a poloidal cross-section at $\phi = 2°$ in the right plot and the corresponding split in the $q_{\parallel\mathrm{cond},e}$-profile in the left plot. The intersections between the field line and the poloidal plane are shown in both plots where the shades of grey and the horizontal axis in the left plot represents the normalised arclength $l_\parallel/\|l_\parallel\|_\infty$.

Density, temperature and pressure profiles

The electron density n_e, electron and ion temperature T_e, T_i and static pressure p_e, p_i, and the Mach number M profiles along the field lines associated with the upper horizontal target are plotted in Fig. 37 for the $f_{\mathrm{rad}} = 0.2$ and $f_{\mathrm{rad}} = 0.8$ case in the left and right column, respectively. These are the relevant profiles for discussing the parallel heat flux density terms as they are the only quantities they depend on. The middle of the profiles are indicated by the grey dashed line as a reference when distinguishing between the left and the right part of the field line as shown in Fig. 36. Furthermore, the black dashed line in the field line profiles is a reference line at $l_\parallel/\|l_\parallel\|_\infty = 0.25$ and $l_\parallel/\|l_\parallel\|_\infty = 0.75$ for the coloured dashed lines representing the X-points.
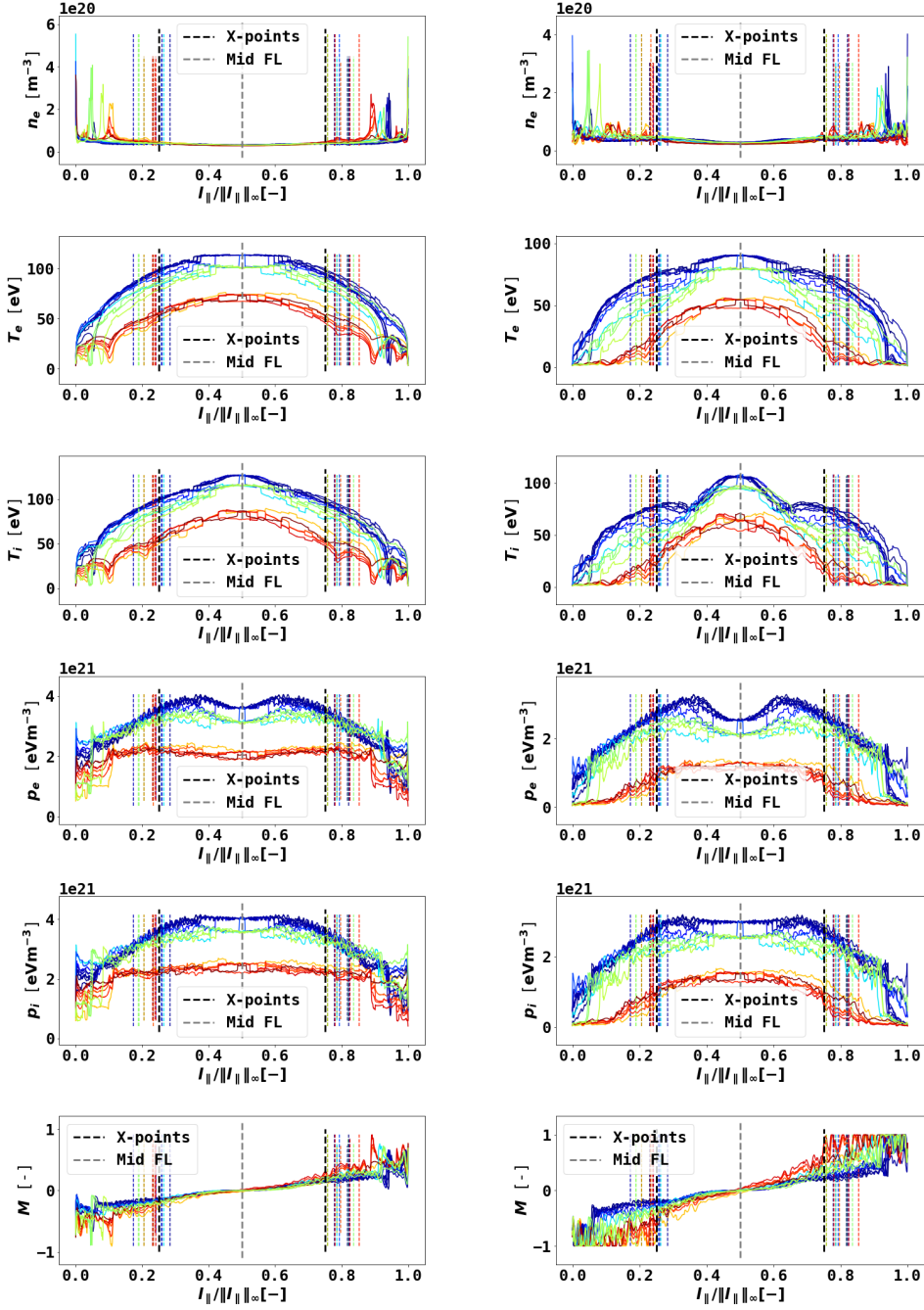
(.1) $f_{\text{rad}} = 0.2$.   (.2) $f_{\text{rad}} = 0.8$.

Figure 37: The field line profiles of ion and electron density, temperature, pressure and Mach number along the normalised arclength $l_{\parallel}/\|l_{\parallel}\|_{\infty}$ are shown for $f_{\text{rad}} = 0.2$ and $f_{\text{rad}} = 0.8$ in 37.1 and 37.2, respectively. The colour of the lines indicate the same field lines as in Fig. 35. The X-points locations for each field line are approximated by taking the index of the set of intersections between the field lines and the poloidal plane at $\phi = 2°$ closest to 20% and 80% of the maximum index of the intersections. These selected points correspond to the vertical dashed lines with respect to both location and colour. The black dashed lines labeled X-points at $l_{\parallel}/\|l_{\parallel}\|_{\infty} = 0.25$ and $l_{\parallel}/\|l_{\parallel}\|_{\infty} = 0.75$ are given as a reference for the X-points.

(.1) $f_{\rm rad} = 0.2$ (.2) $f_{\rm rad} = 0.8$
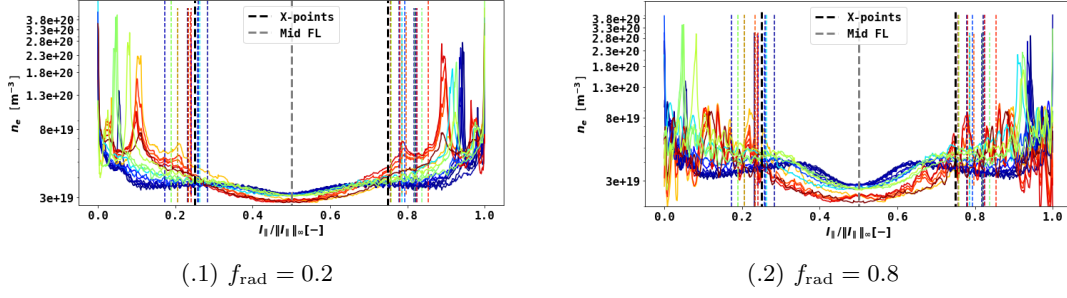
Figure 38: The logscaled electron density in the SOL.

The density profiles for both cases tend to increase by around 25% from the middle of the field line where they have a minima as seen in Fig. 38 to around $l_\parallel / \|l_\parallel\|_\infty = 0.1$ where they exhibit a maximum. In the same region the temperature has a strong gradient towards the targets followed by a positive gradient forming a local minima in the temperature profile. The spike in the density profile agrees with the change in signs of the cross-field convective terms in Figs. 32 and 33. Furthermore, the density profiles for field lines closer to the O-point have a steeper slope than the field lines closer to the outer flux surface of the island. This explains why the slope of the pressure profiles increases with the radial distance in the island reference frame as the temperature profiles seem to be independent of location in the island.

The electron temperature profiles also show a clear tendency. In the range where the normalized field line arclength $l_\parallel / \|l_\parallel\|_\infty \in [0.4, 0.6]$ the electron temperature almost constant. Then it starts to decrease to around $l_\parallel / \|l_\parallel\|_\infty \sim 0.1, 0.9$ for the left part and right part, respectively, where it exhibits a local minima meaning the parallel electron conduction will change directions before T_e continues to decay towards the target. The decay is approximately linear for $f_{\rm rad} = 0.2$ implying parallel electron conduction $q_{\parallel{\rm cond},e} \sim T_e^{5/2}$ since $\nabla_\parallel T_e \sim$ const. This was not the case for $f_{\rm rad} = 0.8$ where the temperature profile does not have clear local minima at $l_\parallel / \|l_\parallel\|_\infty \sim 0.1, 0.9$. Furthermore, the local minima is correlated to the location of the ionisation and radiation front as the temperature decreases in the region where the plasma-neutral interaction and impurity radiation sinks are active. The ion temperature profiles have similar features, but it peaks around the middle of the field line region where the electron temperature is approximately constant, and does not have local minima at $l_\parallel / \|l_\parallel\|_\infty \sim 0.1, 0.9$.

Since, quasi-neutrality is assumed and the electron density has a minimum at the middle of the field line the ion pressure profile is flat at the middle as opposed to the electron pressure which exhibits a local minima. The width of the kink in the pressure profiles at around $l_\parallel / \|l_\parallel\|_\infty \sim 0.1, 0.9$ for $f_{\rm rad} = 0.2$ is increased for $f_{\rm rad} = 0.8$. Furthermore, this feature resembles a stepwise drop in the pressure for $f_{\rm rad} = 0.2$ compared to a continuous transition in $f_{\rm rad} = 0.8$. Overall the ion and electron temperature profiles exhibit similar properties causing the ion and electron pressure profiles to have the same general tendency. They vary little in the range $l_\parallel / \|l_\parallel\|_\infty \in [0.3, 0.7]$ and then decay approximately linearly towards the target.

(.1) $f_{\rm rad} = 0.2$ (.2) $f_{\rm rad} = 0.8$
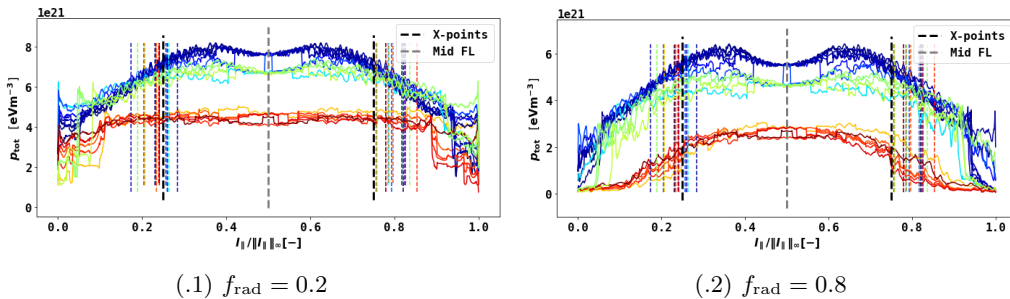
Figure 39: The total pressure $p_{\rm tot}$ in the SOL.

The static pressures and the Mach number are seem to be coupled, which is expected as the static

and dynamic pressure is coupled. Total pressure is not preserved as shown in Fig. 39 since other energy sources and sinks are present, but the plasma velocity is increased when the static pressure decrease. Furthermore, the slope of the static pressure profiles are linear, and since $p_{\mathrm{static}} \propto v^2$ the response will be $\propto \sqrt{p}$ in the Mach profile as the plasma velocity $v = c_s M$. The response in the pressure and flow profiles for $f_{\mathrm{rad}} = 0.8$ compared to $f_{\mathrm{rad}} = 0.2$ supports this supports the correlation between increasing velocity for decreasing pressure as the slope of both profiles are steeper at $f_{\mathrm{rad}} = 0.8$.
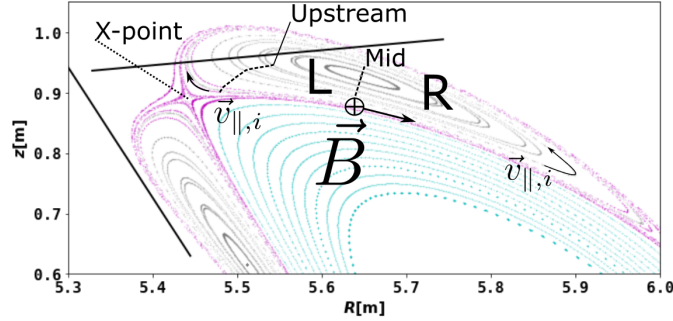
Figure 40: A schematic illustration of the flow picture of the island with respect to the left and right part of the field line indicated by L and R, respectively. Furthermore, the upstream is defined at the black dashed line above the X-point and the targets are given by the black lines. The direction of the magnetic field is indicated by $\otimes$ representing the toroidal direction and the black arrow representing the component of the velocity vector in the poloidal cross-section. The flow direction in the poloidal cross-section is indicated by the black arrow attached to $\vec{v}_{\parallel,i}$.

The profiles of the Mach number $M = v_{\parallel,i}/c_s$ where c_s is the sound speed, show that the plasma flow increases below the X-points and is negative for the left and positive for the right part of the field line. The direction of the magnetic field is positive in the direction of increasing arclength. So, the negative value of the left part of the field line indicate that flow goes from upstream to the targets, i.e. in the opposite direction of the magnetic field which agrees with the study of the plasma flow in the W7-X ID done by Perseo et al. (2021) [58]. The observed tendency is that the electron and ion parallel temperature gradients $\nabla_\parallel T_e$ and $\nabla_\parallel T_i$, respectively, are negative in the direction from upstream to the targets. This implies that the parallel conduction goes against the magnetic field in the left part and along the field in the right part of the field line. The flow is also negative for the left part of the field line, meaning it goes against the magnetic field, and vice versa for the right part of the field line. The Mach number increases below the X-points at the inverse cusp in the temperature and spike in the density profiles at the ends of both parts of the field lines close to the targets. Since the local minima in the temperature profiles are associated with the ionisation front, this implies that the increase in plasma flow correlates with the location of the ionization front.

There are clear differences between the high and low radiation case. The decay in the temperature profiles is more profound for $f_{\mathrm{rad}} = 0.8$ compared to $f_{\mathrm{rad}} = 0.2$, as expected from the larger radiation loss. Furthermore, the initial decay in the ion temperature is stronger close to the middle of the field line and the electron temperature has a stronger decay below the X-points for the $f_{\mathrm{rad}} = 0.8$ case. This agrees well with the effect of the inward movement of the radiation and ionization front discussed in section 2 observed by Feng [1]. The ion temperature profiles for $f_{\mathrm{rad}} = 0.8$ case also exhibit saddle at $l_\parallel / \|l_\parallel\|_\infty \approx 0.4, 0.6$. The flattening can be due to longer neutral penetration depths as the temperature was reduced due to larger radiation loss causing the temperature to decay further upstream. The latter is due to the inward movement of the radiation front when the radiated power fraction is increased. The inward movement is shown in section 1 in Fig. 12. This implies that the parallel conduction is small as the region's temperature gradients are close to zero. Thus, the pressure profiles for the $f_{\mathrm{rad}} = 0.8$ case show a larger pressure drop that starts further upstream, especially for the field lines closer to the O-points for which the temperature profiles starts to decay at the middle of the field line. *This implies that the assumptions of constant pressure is invalid, especially for $f_{\mathrm{rad}} = 0.8$ as the pressure drops around*

or above an order of magnitude from upstream to target.

4.2.2 Field line integrand terms

The field line profiles for the parallel heat flux densities, the sources and the sinks, the divergence of the cross-field heat flux density and the parallel gradients of the parallel heat flux densities are shown for the low radiation case in Fig. 41 and the high radiation case in Fig. 42. The plots use the same colours for the profiles and the dashed lines as Fig. 37. The colours of the profiles are consistent with the lines in Fig. 35 and the dashed lines close to the X-points correspond to the dots on the lines in Fig. 35. This is to indicate the approximate location of the X-points with respect to the fraction of the connection length $l_\parallel/\|l_\parallel\|_\infty$.
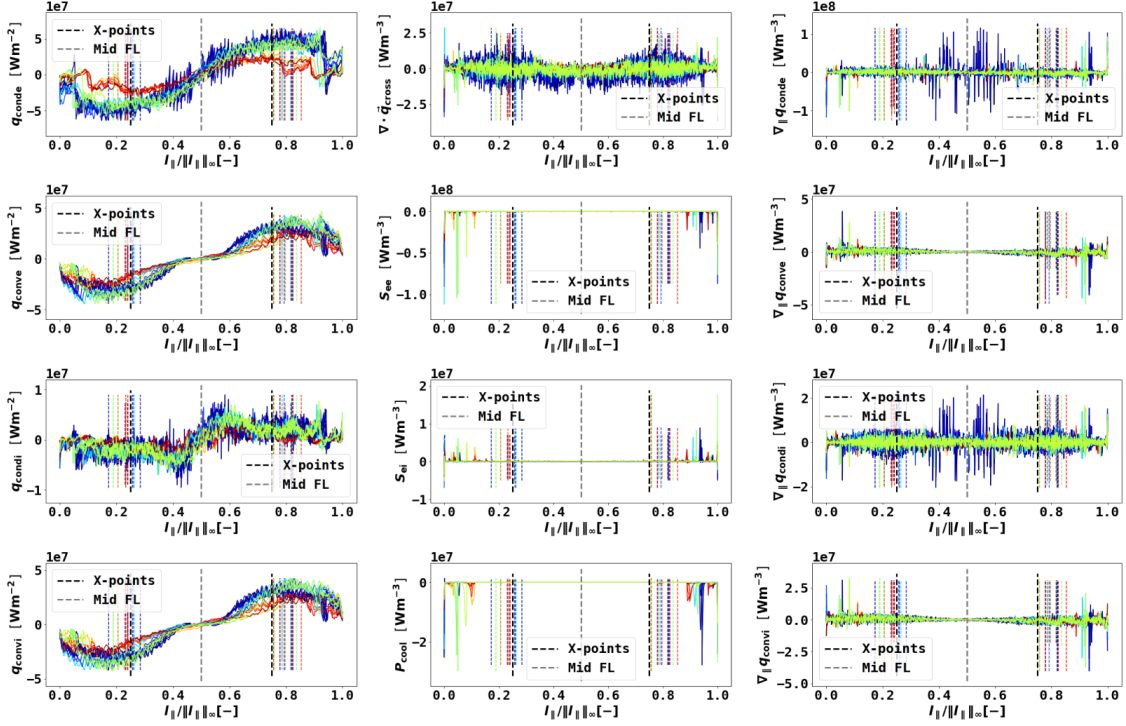
Figure 41: In the left column the profiles of the parallel ion and electron heat flux density along field lines against normalised arclength are shown. The middle column shows the cross-field heat flux density divergence and the sources and sinks. The right column shows the parallel gradient of the heat flux density profiles from the left. All profiles are shown for the low radiation case where $f_{\rm rad} = 0.2$. The lines' colour and the dashed lines' locations are equivalent to the field lines in Fig. 35.

Parallel heat flux densities

The parallel heat flux densities associated with the field lines ending up at the upper horizontal target are shown in the left column of Figs. 41 and 42. The most important observation is that the parallel convective terms are on the same order of magnitude as the parallel electron conductive term. *This invalidates the assumption of dominant parallel electron heat conduction.* Another important observation related to the significance of the transport terms is that the ion conductive heat flux density is approximately an order of magnitude lower than the other terms for both the low and high radiation case. This indicates that the assumption of negligible parallel ion conduction is valid and consistent for $f_{\rm rad} \in \{0.2, 0.8\}$. Furthermore, the parallel conductive electron heat flux density strongly decreases at the X-point in the high radiation case. This is expected from the effect on the temperature profiles as the radiation is stronger and located further upstream [2, 1]. In the same region for the high radiative case the convective transport peaks and kept approximately

constant over 10% of the connection length. This agrees well with the increase in the Mach number profile and the decrease in the pressure profiles below and right above the X-points for the low and high radiation case, respectively.
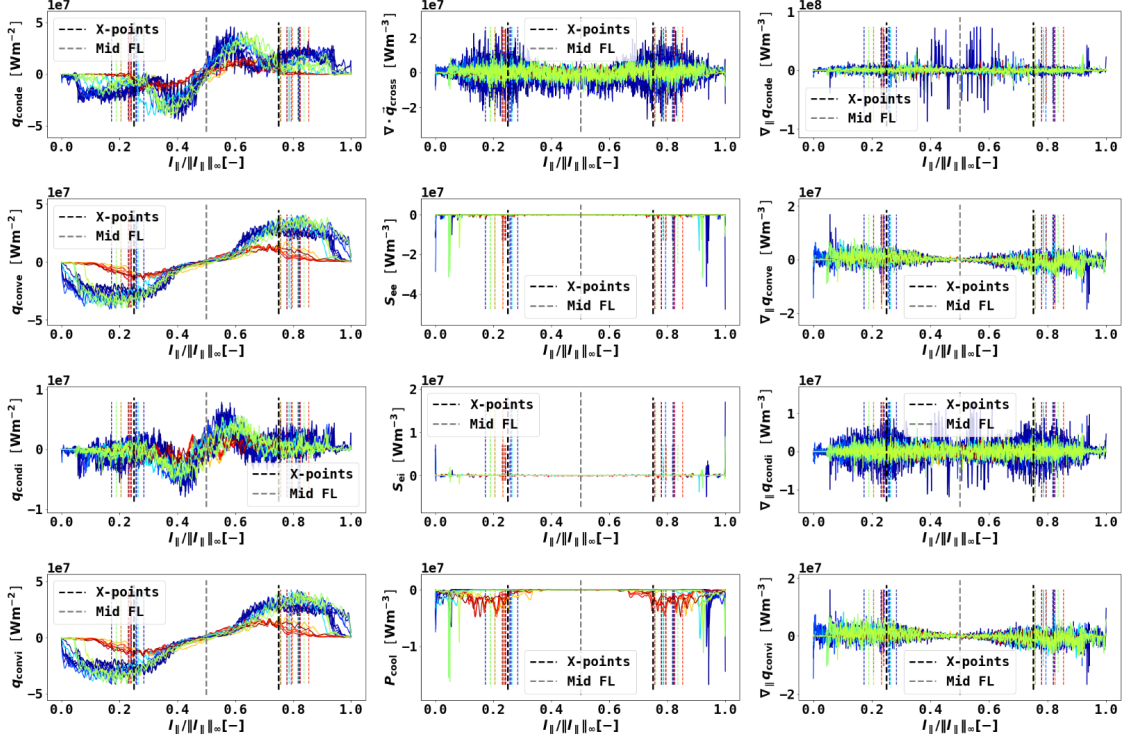
Figure 42: Equivalent to Fig. 41 for $f_{\text{rad}} = 0.8$.

The profiles for the parallel heat flux densities for field lines in the SOL at the outer island flux surfaces are steeper and larger in magnitude than the profiles closer to the O-point. This is consistent with the property that the field lines closer to the O-points are more affected by cross-field transport as described in section 1. More power in the cross-field channel implies less power in the parallel channels. Furthermore, it seems that this happens at the X-point for $f_{\text{rad}} = 0.2$. For the field lines closest to the O-points the parallel electron conductive channel builds up power above the X-point and then decays after passing the X-point. One explanation of the observed decay can be that power is lost at the ionisation and radiation front because it is radially localised in the island reference frame as shown in Fig. 12. Thus, it does not affect the field lines further away from the O-point. However, in the high radiation case all the parallel electron conductive channel profiles show a significant power loss at the X-points due to a broader radiation distribution featured in Fig. 12.2. This agrees with Feng's observation of a helically continuous distribution of the radiation volume for high radiated power fractions. The ratio between parallel conduction and convection is shown in Fig. 43 where the parallel conduction is larger at the spikes close to the targets and an order of magnitude larger only in a narrow region around the middle of the field line. Everywhere else, the parallel convection and conduction have the same order of magnitude or the parallel convection is larger. *Thus, the assumption of dominant parallel electron conduction is invalid, and if assumed higher radiated power fractions will give larger errors.*

(.1) $f_{\rm rad} = 0.2$ (.2) $f_{\rm rad} = 0.8$
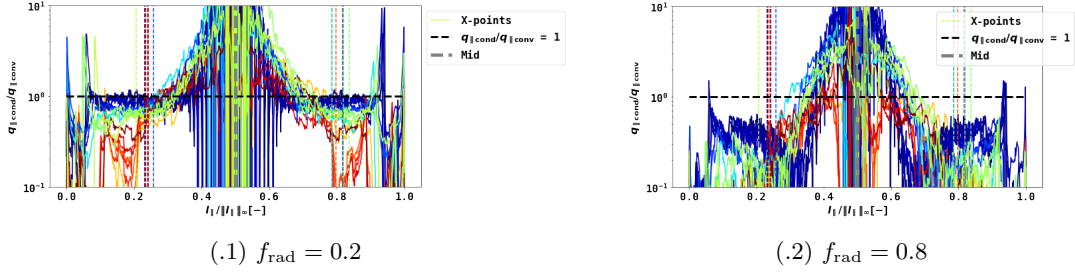
Figure 43: The ratio of between the parallel conduction and parallel convection in the SOL.

The magnitude of the parallel convective terms is a factor of ~ 5 larger than the parallel electron conduction and an order of magnitude larger than the parallel ion conduction for $f_{\rm rad} = 0.8$ from the X-points to the targets where most of the sources, sinks and cross-field transport is active. Furthermore, the relative importance of parallel convection increase for field lines closer to the O-points for both $f_{\rm rad} = 0.2$ and $f_{\rm rad} = 0.8$. For $f_{\rm rad} = 0.8$ the convection is almost an order of magnitude larger than conduction in the region from $l_\parallel / \|l_\parallel\|_\infty \in \{0.3, 0.7\}$ to the targets. The only exception is a spike in the conduction for the field lines at the outer island flux surface implying some intermediate transfer of power to the parallel ion conduction channel indicated by the spikes in the $q_{\parallel {\rm cond},i}$-profile at $l_\parallel / \|l_\parallel\|_\infty \in \{0.1, 0.9\}$. *Thus, for $f_{\rm rad} = 0.8$ the total convective flow could be assumed dominant.*

The computation of the divertor-relevant field line pitch was left out for future work, but can be assumed constant following the arguments of Feng where $\Theta \sim 10^{-3}$ [4, 52]. This implies that the parallel heat flux terms are on the order of $10^4\ {\rm Wm^{-2}}$ except the parallel conductive ion term which is an order of magnitude lower. From the previous subsection it was observed that the radial projection of the total cross-field heat flux density was on the order of $10^5\ {\rm Wm^{-2}}$. This implies that the cross-field transport is significant and might be dominant in some regions. These observations agree with the suggested importance of the cross-field transport in Feng et al. (2006) [4]. However, it is unclear if it can be assumed to dominate over parallel transport throughout the SOL because the cross-field heat flux density is observed as being strongly localised around the X-points. Furthermore, the cross-field convective transport is observed to be negative below the X-points and the parallel convection is positive with respect to the direction towards targets. Thus, the general tendency of the net heat transport due to the convective channel in the PFR is not clear when convection is decomposed. The negative region of the cross-field convection are on the order of $10^4\ {\rm Wm^{-2}}$ which is the same order as the projected parallel heat flux densities. However, the convective cross-field heat flux density still appears to be the dominant term in the SOL. *Thus, it is clear that in the SOL the ion convective cross-field heat flux density is significantly larger than the other cross-field terms as it contributes to most of the total cross-field heat flux density ($\sim 50\%$). So, according to the observations made in this thesis the energy transport cannot be assumed to be conduction dominated. This conclusion agrees with the trend of the ratio between the parallel convection and the parallel conduction as shown in Fig. 43, but disagrees with Feng's assumption of dominant conductive transport in Feng et al. (2006) [4].*

Neutral sources and sinks, and radiative power loss in the SOL

The profiles for the sources and sinks along the field lines are shown in the center column in Figs. 41 and 42 for the low and high radiation case, respectively. For $f_{\rm rad} = 0.2$ the plasma-neutral interaction due to ion impact appears as a power source below the X-point except at the target where it alternates. The plasma-neutral interaction due to electron impact appears as a sink throughout the field line and the spikes in the profiles indicate the ionization front which starts at around $l_\parallel / \|l_\parallel\|_\infty = 0.1$ and $l_\parallel / \|l_\parallel\|_\infty = 0.9$. The plasma-neutral interaction sources and sinks in the low radiation case are located in the same region as the low temperature impurity radiation. This implies that most ionisation loss happens in the same region where the low Z charge states ionise. Furthermore, the magnitude of the neutral losses is significantly reduced in the high radiation case where more energy is lost due to radiation than ionisation shown in Fig. 44. Furthermore, the log-scale makes the separation between the radiation distribution for field lines close to the O-point and field lines close to the outer flux surface of the island visible. This has to

be seen in context of the radiation distribution in the whole SOL shown in Fig. 12 considering that the field line visits all islands from target to target. The radiation is not equally distributed in each island, but vary with respect to the radial distance from the O-point in the island reference frame. The dependency seems beneficial for the field lines closer to the O-points as the radiation intensity is generally larger for the field lines close to the O-point than close to the outer flux surface of the island.

(.1) $f_{\mathrm{rad}} = 0.2$.

(.2) $f_{\mathrm{rad}} = 0.8$.
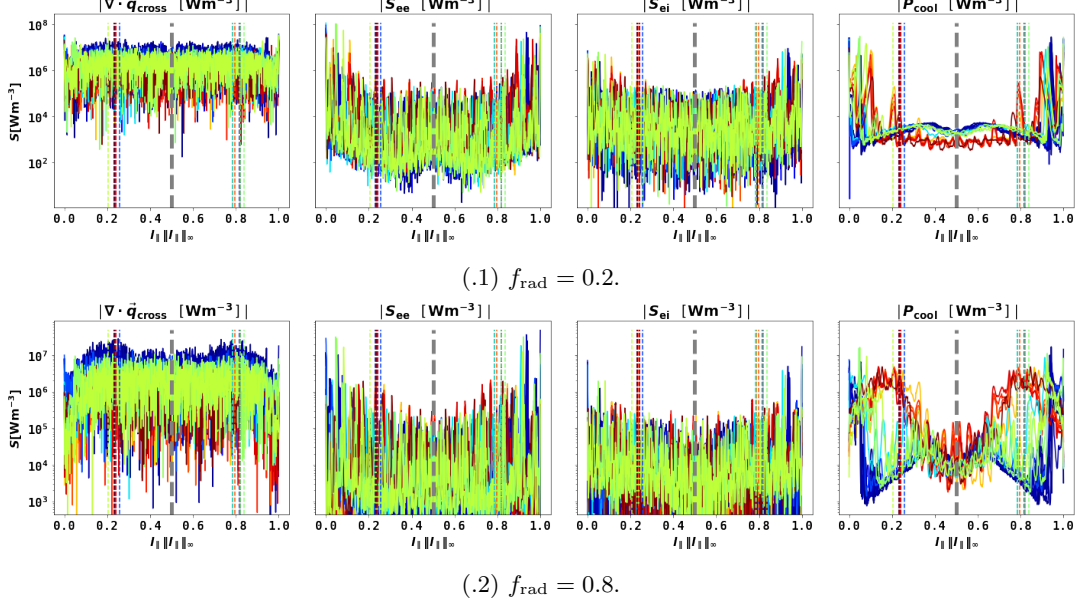
Figure 44: The absolute value sources and sinks, and the divergence of the cross-field heat flux density in the SOL have been plotted with a log-scaled y-axis.

The radiation profile show that the the radiation front has moved further upstream and is broader distributed along the field line for $f_{\mathrm{rad}} = 0.8$, as expected. The parallel conduction and convection increase simultaneously for $f_{\mathrm{rad}} = 0.2$ in the region from the middle of the field line to the X-points, implying that the convective and conductive channel receives power from other channels. The neutral sources are inactive in this region implying that the power supplied to the parallel channels comes from the cross-field channel. Furthermore, the spikes at both ends of the $\nabla \cdot \boldsymbol{q}_{\mathrm{cross}}$-profile have been significantly reduced at $f_{\mathrm{rad}} = 0.8$ as shown in Fig. 44 compared to $f_{\mathrm{rad}} = 0.2$. The reduction of the spikes indicates that the cross-field transport right in front of the target is suppressed for higher radiated power fractions, which agrees with the cross-field heat flux density reduction seen in the 2D profiles shown in Figs. 32 and 33. This is because increased radiated power loss is followed by broadening of the radiation distribution which effectively flattens out the temperature and density gradients close to the target.

Parallel gradient of the parallel heat flux density terms

The field line profiles of the parallel gradient of the parallel heat flux density is shown in the right column Figs. 41 and 42 for the low and high radiation case, respectively.
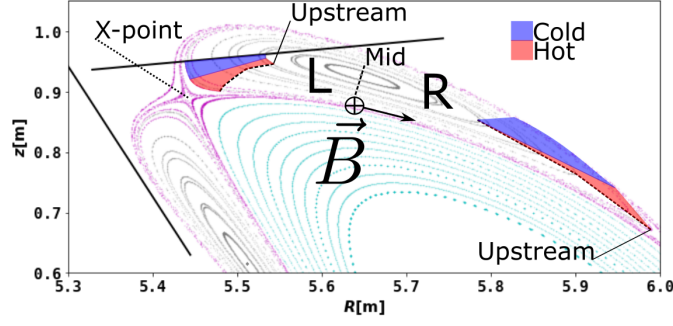
Figure 45: An illustration of the hot and cold parts of the region between upstream represented by the dashed black line and the target. The intention with this illustration is to show the regions of the general tendency of the $\nabla_\parallel q_{\mathrm{conv}}$ terms with respect to the left and right part of the field line. For the left part of the field line denoted L $\nabla_\parallel q_{\mathrm{conv}} > 0$ for the hot region and $\nabla_\parallel q_{\mathrm{conv}} < 0$ for the cold region. For the right part of the field line denoted R $\nabla_\parallel q_{\mathrm{conv}} > 0$ for the hot region and $\nabla_\parallel q_{\mathrm{conv}} < 0$ for the cold region. This agrees with the parallel heat flux density profiles in Figs. 41 and 42.

The trends in the parallel gradient of the parallel convection profiles are schematically illustrated in Fig. 45 where the sign of the gradients are associated with the cold and hot part of the target to upstream region. For some of the field lines there are spikes at $l_\parallel / \|l_\parallel\|_\infty = 0.1$ and $l_\parallel / \|l_\parallel\|_\infty = 0.9$ to the target. Note that the spikes for the parallel gradient of the parallel convective heat flux density terms tends to be positive and negative for the conductive heat flux density terms for the left part of the field line and vice versa for the right part of the field line. There seem to be a correlation between the location where power is lost from the conductive channel and the location where the convective channel receives power. Furthermore, the spikes are in the same region as the radiation and neutral sources and sinks have spikes. This indicates that the parallel conductive's power loss and the parallel convective channel's gain come from ionisation and radiation. However, the temperature dependence of the parallel convective channel reduces the transport significantly from $l_\parallel / \|l_\parallel\|_\infty = 0.1$ and $l_\parallel / \|l_\parallel\|_\infty = 0.9$ to the target.

4.2.3 Radiative power loss function

The assumption of constant residence time for the impurities was compared with the transport implemented in EMC3-EIRENE. The constant residence time assumption mimics the transport by a constant transport term n_Z / τ of charge states from their equilibrium temperature region to lower or higher temperature regions. The residence time is referred to as τ in this section because it is modeled to be independent of charge state Z. Previously it was referred to as τ_Z to avoid confusion with other τ-parameters when discussing characteristic times for impurity transport. The fractional abundances are shown in Fig. 46 where the fractional abundances computed with the EMC3 simulations are compared with an assumed constant residence time of $\tau = 10^{-3}$s and electron density $n_e = 10^{20}\mathrm{m}^{-3}$ mimicking transport from lower to higher regions for the low radiation case. This was computed using data from ADAS ADF11 iso-nuclear files [33].
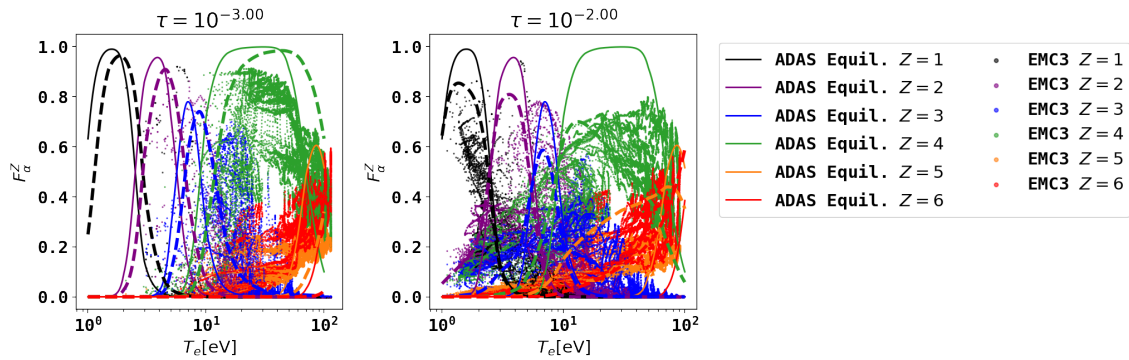
Figure 46: The fractional abundances is shown in the left plot for the EMC3 simulations compared with the ADAS fractional abundances for $\tau = 10^{-3}$s and constant electron density $n_e = 10^{20}$m^{-3} for the $f_{\rm rad} = 0.2$ case for transport from lower to higher temperature regions. The corresponding plot to the right is for the $f_{\rm rad} = 0.8$ case for transport with $\tau = 10^{-2}$s from higher to lower temperature regions. The different colours indicate different ionisation stages Z of Carbon. The same colour is used in EMC3 and ADAS computations for each ionisation stage.

A smaller τ means that the charge state spend less time in a lower temperature region before being transported to a higher temperature region. This is shown for $f_{\rm rad} = 0.2$ in the left plot of Fig. 46. The interpretation of the τ parameter when mimicking transport of charge states from higher to lower temperature regions is similar, but the transport direction is reversed. Then, a small τ means that the charge state will spend less time in the high temperature region before it is transported to a lower temperature region. This is shown for $f_{\rm rad} = 0.8$ in the right plot of Fig. 46.

In the case of the EMC3 simulations it seems like the charge states are "squeezed" from both ends of the temperature range. Lower charge states seem to be transported towards higher temperature regions and higher charge states are transported to lower temperature regions when compared with the equilibrium fractional abundances. The observation implies that the fractional abundances are best resolved for an assumed constant transport by combining transport from lower to higher temperature for lower charge states and vice versa.

Since the curve representing the assumption of constant $n_e\tau$ does not fit the fractional abundances well, the radiative power loss function will be weighted accordingly. The effect on transport of charge states from lower to higher temperature regions on the radiative power loss function L_α is shown in Fig. 47. The effective radiative power loss function from the EMC3 simulations $L_\alpha^{\rm EMC3}$ shown in Fig. 47 for the field lines in the SOL and are compared to a set of $n_e\tau$ parameters, equilibrium radiative power loss function and the radiative power loss function for an assumed penetration depth $\lambda_{\rm neutral}$ of the neutrals where $\lambda_{\rm neutral} = 0.13$ m which includes transport due to charge-exchange. This was included to demonstrate that the result would not be very different if charge-exchange was included in the modeling.

(.1) The radiative power loss functions for $f_{\text{rad}} = 0.2$

(.2) The radiative power loss functions for $f_{\text{rad}} = 0.8$.
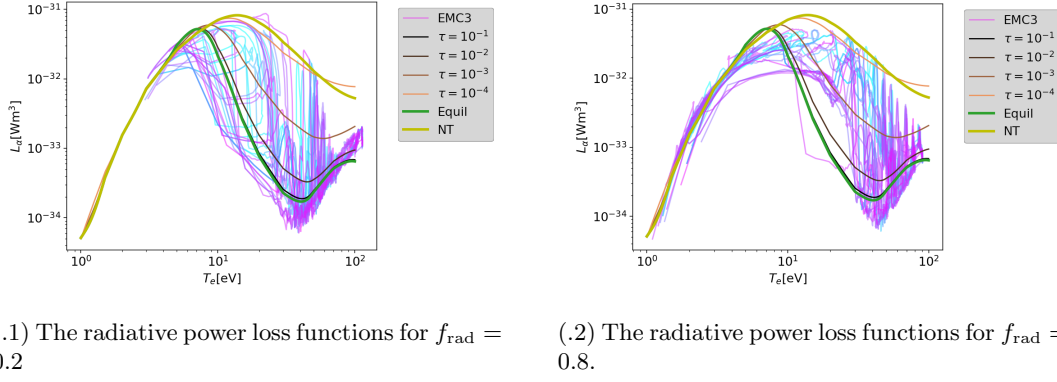
Figure 47: The radiative power loss functions for various parameters of τ for a constant density $n_e = 10^{20} m^{-3}$ are shown in lines in black to orange, and for the effective radiative loss function for field lines in the SOL in colours from pink to cyan. The equilibrium radiative power loss function is represented by the green line and the radiative power loss function assuming a neutral penetration depth $\lambda = 0.13$m is represented by the yellow line.

Even though the radiative power loss function using the ADAS data does not fit L_α^{EMC3} well locally it is the integrated value as given in Eq. 47 in section 2 which is important. The temperature weighted radiative power loss function $L_\alpha \sqrt{T_e}$ is shown in Fig. 48 which is the term that appears in the Lengyel integrand given by Eq. 114. Note that this assessment is related to the assumption of constant residence time, static electron pressure, and impurity concentration. Compared to the plots in Fig. 47 the tendency is that the temperature weighting seems to flatten out the curve and increasing the transport broadens the $L_\alpha \sqrt{T_e}$ profile. However, the impact on the integrated and temperature weighted value $\int_t^u dT_e L_\alpha \sqrt{T_e}$ is not clear just by looking at the profiles.

(.1) The integrand $L_\alpha \sqrt{T_e}$ for $f_{\text{rad}} = 0.2$

(.2) The integrand $L_\alpha \sqrt{T_e}$ for $f_{\text{rad}} = 0.8$.

Figure 48: The integrand $L_\alpha \sqrt{T_e}$ are shown for various parameters of $n_e \tau$ where the electron density was approximated to be $n_e = 10^{20} \text{m}^{-3}$. The residence time τ represents transport from lower to higher temperature regions. The Lengyel integrand is also shown for the EMC3 cases, including the impurity transport. The labeling and colouring is the same as in Fig. 47. The dashed horizontal lines represents the integral from target to upstream $\int_t^u L_\alpha \sqrt{T_e} dT_e$.

Therefore, the $L_\alpha \sqrt{T_e}$ profile was integrated from target to the middle of the field line to have a consistent definition of upstream for the approximated and the effective radiated power loss function. The dashed lines in Fig. 48 represent the integral from target to upstream. Furthermore, the integral was only computed for the left part of the field line, i.e. from $l_\parallel / \|l_\parallel\|_\infty = 0$ to $l_\parallel / \|l_\parallel\|_\infty = 0.5$. For the low radiation case the assumption of constant transport with $\tau \in [10^{-2}, 10^{-1}]$ captures most of the radiation losses. However, it does not capture the field lines with significantly lower radiation loss. Furthermore, for $f_{\text{rad}} = 0.2$ the integral seem to be characterised by transport from higher to lower temperature regions which is shown in Fig. 49.

(.1) The integrand $L_\alpha\sqrt{T_e}$ for $f_{\mathrm{rad}} = 0.2$ (.2) The integrand $L_\alpha\sqrt{T_e}$ for $f_{\mathrm{rad}} = 0.8$.

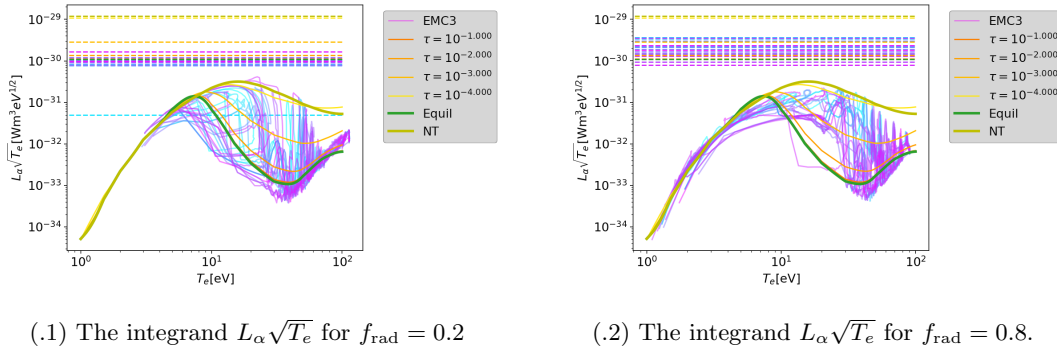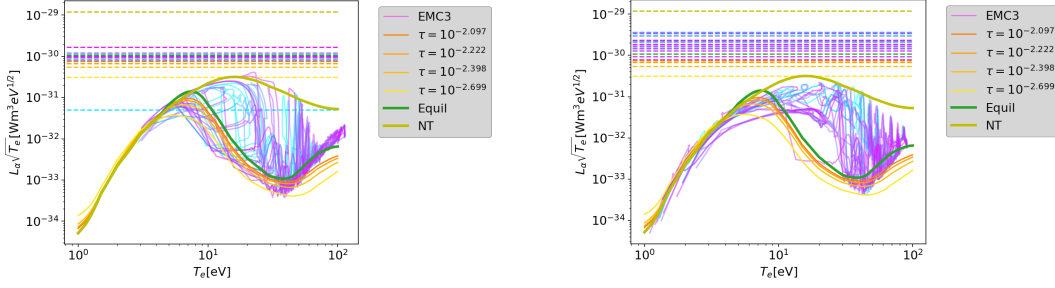Figure 49: The integrand $L_\alpha\sqrt{T_e}$ are shown for various parameters of $n_e\tau$ where the electron density was approximated to be $n_e = 10^{20}\mathrm{m}^{-3}$. The residence time τ represents transport from higher to lower temperature regions. The Lengyel integrand is also shown for the EMC3 cases which include the impurity transport. The labeling and colouring is the same as in Fig. 47. The dashed horizontal lines represents the integral from target to upstream $\int_t^u L_\alpha\sqrt{T_e}dT_e$.

The radiation distribution for $f_{\mathrm{rad}} = 0.2$ is characterised by transport from higher to lower temperature regions and vice versa indicated by the effective power loss functions lying on both sides of the equilibrium profile. The integral values indicates that the best fit is between equilibrium radiation loss function and transport with $\tau \approx 10^{-2}$ for transport from higher to lower temperature regions. On the other hand, for $f_{\mathrm{rad}} = 0.8$ the power loss function profiles and the Lengyel integrand, and the integral values are better fitted by transport from lower to higher temperature regions indicated by both the profiles and the integral values. This is consistent with the inward movement of the radiation front as the radiation distribution for $f_{\mathrm{rad}} = 0.8$ is moved to a region with relatively larger temperature compared to $f_{\mathrm{rad}} = 0.2$. *Thus, $f_{\mathrm{rad}} = 0.2$ involve complicated impurity transport leading to a complex impurity radiation distribution. However, the assumption of constant impurity residence time looks promising for transport from higher to lower temperature regions for $f_{\mathrm{rad}} = 0.2$ as indicated by the integral values in Fig. 49.1 for $n_e\tau \approx 10^{18}\mathrm{m}^{-3}$s and lower to higher temperature regions for $f_{\mathrm{rad}} = 0.8$ as indicated by Fig. 48.2 for $n_e\tau \in [10^{17}, 10^{18}]\mathrm{m}^{-3}$s.*

4.2.4   Field line integral terms

The integral terms on the RHS of Eq. 52 was computed for each field line associated with the upper horizontal target. All terms were normalised to $(q_{\|\mathrm{cond},e,\mathrm{u}}/2)^2$ and the absolute values of the terms are shown in the bar plots in Fig. 50. The symbols in the legend of the plots are the same as in Eq. 46-51. Furthermore, the upstream location is defined as at the maximum of the parallel electron conductive heat flux density of both parts of the field line when dividing it at the middle. The location of upstream in the left part is at the arclength $l_\| = l_\|\left(\left\|q_{\|\mathrm{cond},e}^{(\mathrm{left})}\right\|_\infty\right)$. The upstream location of the right part is $l_\| = l_\|\left(\left\|q_{\|\mathrm{cond},e}^{(\mathrm{left})}\right\|_\infty\right)$. In the expressions the arclength has been expressed as a function of the parallel electron conductive heat flux density, and evaluated at the maximum of $q_{\|\mathrm{cond},e}$ for the left and right part indicated by the superscripts.

(.1) $f_{\mathrm{rad}} = 0.2$.

(.2) $f_{\mathrm{rad}} = 0.8$.
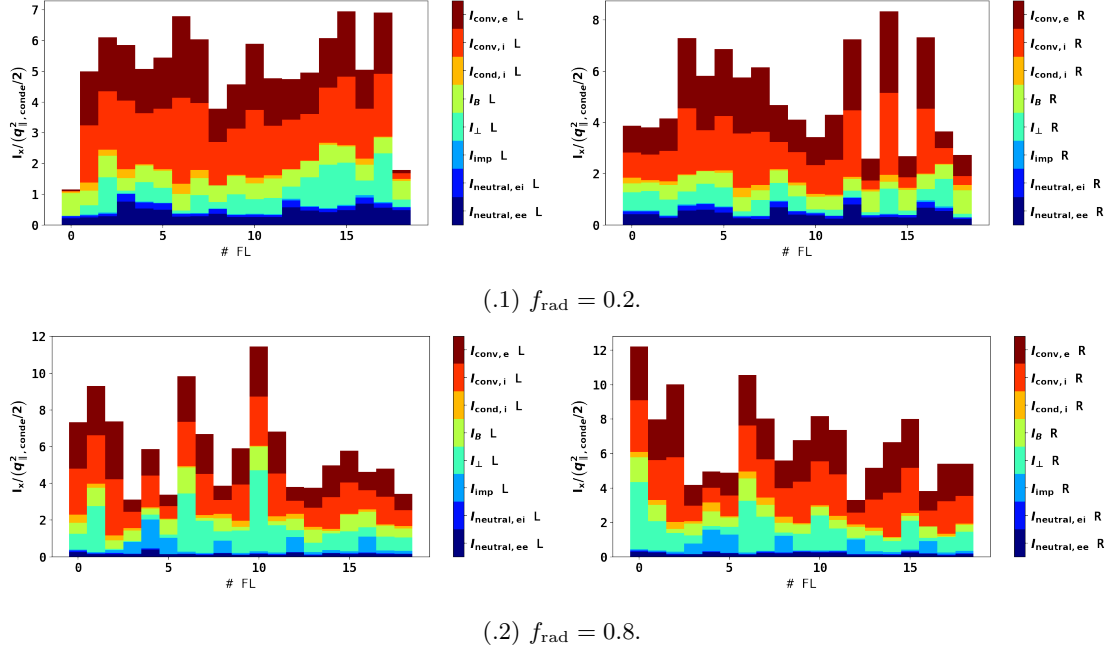
Figure 50: The integral terms from Eqs. 46-51 from Eq. 52 are shown for each field line whose number # FL is represented by the horizontal axes. Each term is shown with a unique colour. The field lines are split at the upstream location into a left and right part. The left part of the field line starts at arclength $l_\parallel = 0$ and ends at $l_\parallel = l_\parallel \left(\left\| q_{\parallel\mathrm{cond},e}^{(\mathrm{left})} \right\|_\infty \right)$, and the right part starts at $l_\parallel = l_\parallel \left(\left\| q_{\parallel\mathrm{cond},e}^{(\mathrm{left})} \right\|_\infty \right)$ and ends up at $l_\parallel = L_c$. This is done to compute the integral from target to upstream.

The plots in Fig. 50 intends to show the transfer of power from or to the parallel conductive channel to or from the sources, sinks and the divergence of the cross-field heat flux density. After the normalisation to $(q_{\parallel\mathrm{cond},e}/2)^2$ the LHS of Eq. 52 reads $1 - q_{\parallel\mathrm{cond},e,\mathrm{t}}^2 / q_{\parallel\mathrm{cond},e,\mathrm{u}}^2$. Thus, the LHS represents how much power the parallel conductive heat flux channel has effectively lost to other channels from upstream to target due to all the sources and sinks given by the terms on the RHS. The connection length are associated with the field line number # FL in Fig. 51. The cross-field term $I_\perp$ in Fig. 50 is large for field lines that have long connection lengths, for instance #FL $= 1, 2, 6, 7, 9, 10, 11$ which is either seen on the contribution of the left or the right part of the field line.
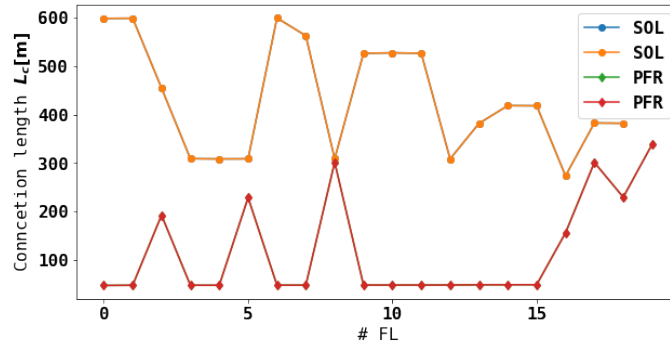
Figure 51: The connection length L_c against the field line number # FL for both cases and for field lines in the SOL and PFR.

To convince the reader about the interpretation of the integral along the field line the Lengyel model is examplified. The integral given in Eq. 114 represents the power loss due to radiation

along a field line assuming dominant parallel electron conductive transport. This is the same as power being lost from the parallel conductive channel. The power is lost because the plasma is assumed to be optically thin so the radiation escapes the plasma and is deposited on the wall components. In a general situation where every energy transport mechanism is considered power is not necessarily just lost to the wall components, but can be transferred from one channel to another. For example at the ionization front the power can be lost from the conductive to the convective channel. Another example is the transfer of power between field lines via cross-field transport where one of the parallel channels carries the power that the field line receives from the cross-field channel. The exchange of power from the cross-field channel to the parallel channel continues until the heat is deposited at the wall components.
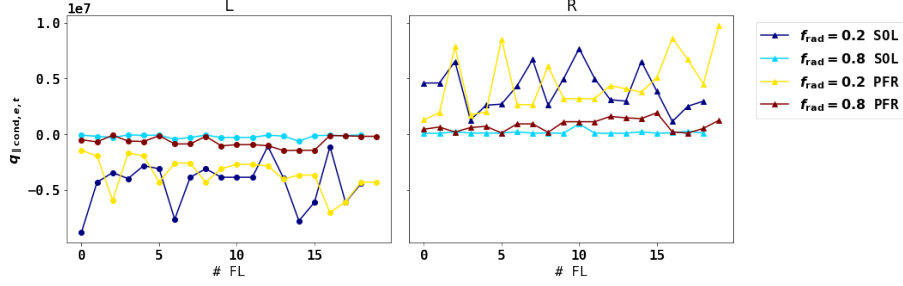
Figure 52: The target parallel electron heat flux density $q_{\parallel \text{cond},e,\text{t}}$ with respect to the field line number # FL.

In the terms of the integrals on the RHS of Eq. 52 the upstream parallel conductive heat flux $q_{\parallel \text{cond},e,\text{u}}$ is compared with the parallel conductive heat flux at the target $q_{\parallel \text{cond},e,\text{t}}$ shown in Fig. 52 for the respective field line number # FL. The parallel electron conductive heat flux $q_{\parallel \text{cond},e,\text{t}} < q_{\parallel \text{cond},e,\text{u}}$ by definition. The values of $q_{\parallel \text{cond},e,\text{t}}$ indicates a maximum target heat flux density at $\sim 10 \text{MWm}^{-2}$ and a significant decrease for $f_{\text{rad}} = 0.8$ for all field lines in the SOL and the PFR.

The absolute value of each integral term is represented by the bar plot to demonstrate the magnitude of each transport mechanism's contribution effective power loss of the parallel electron conduction channel. For higher radiated power the contribution from the impurity radiation integral is higher as expected, but compared to the magnitude of other terms it is unexpectedly small. The parallel conductive ion transport contribution is negligible as expected from the field line profiles. The parallel convective terms are dominating both cases. Furthermore, the cross-field term is significant in both cases, and increase for $f_{\text{rad}} = 0.8$. However, the neutral losses are larger for $f_{\text{rad}} = 0.2$ and decrease for $f_{\text{rad}} = 0.8$. Furthermore, the neutral loss due to electron impact is significantly larger than the neutral losses due to ion impact. This agrees well with the relative magnitudes of the field line profiles.
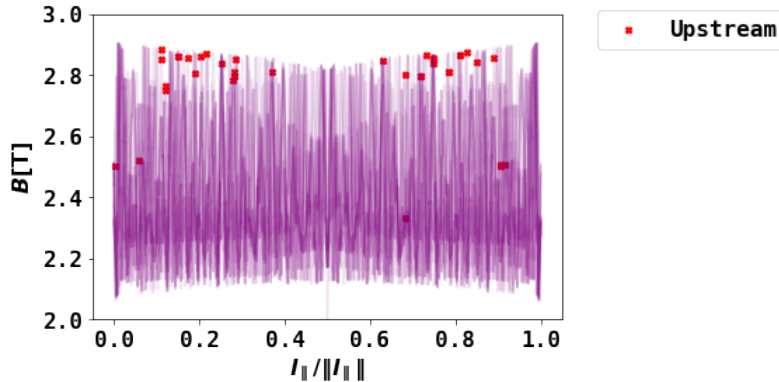
Figure 53: The magnetic field strength along the traced field lines is represented by the purple lines and the upstream locations by the red crosses. Almost all upstream locations is at or close the peak of the magnetic field strength.

Another significant contribution is from the dilution due to the variation of the magnetic field strength along the field line I_B. It is important to note that the term in this analysis represents the worst case as the upstream location is chosen at the peak of the parallel electron conductive heat flux density. Thus, the upstream location is defined at the peak of the magnetic field strength since $q_{\parallel,\text{cond},e} \propto B$. The same magnetic field configuration was used for both simulation cases and the same field lines were traced for comparison. The upstream location with respect to the magnetic field strength is shown in Fig. 53. *Thus, for a different definition of the upstream location the magnetic field strength is either equal or smaller at the upstream location which means that the I_B term will either be equal or smaller. However, based on the observed magnitude of I_B in Fig. 50 we cannot exclude that it is valid to neglect this term.*

Now that the SOL field lines have been analysed the key results of from the field lines in the PFR will be included for completeness. Considering the approximated cross-field heat flux density which is concentrated around the X-point the field lines in the PFR might be crucial for the power exhaust in the ID.

4.2.5 PFR field line analysis

The PFR integral terms were included because the radial heat flux densities were observed to be concentrated around the X-points. This implies that a significant amount of power is transported into the PFR across the X-point via the cross-field transport. Therefore, the same analysis was carried out on the field lines in the PFR as the field lines in the SOL to check for consistencies in the transport properties between the PFR and the SOL.
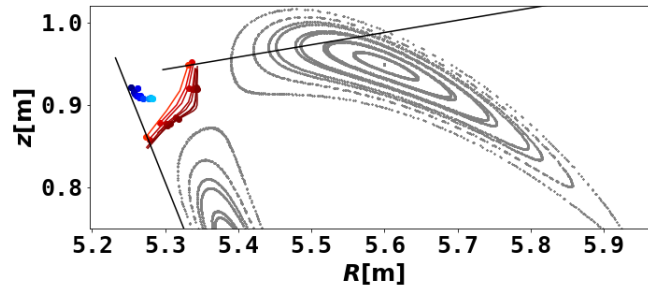
Figure 54: The field lines in the PFR are shown with respect to the magnetic field geometry for a poloidal cross-section at $\phi = 2°$.

The are some characteristic differences between the PFR profiles shown in Fig. 55 and 37. The general shape of the static electron pressure profiles does not exhibit a minimum at the middle of the field line due to approximately constant density profiles as shown in Fig. 56, but have a spike due to the maximum in the density at around $l_{\parallel}/\|l_{\parallel}\|_{\infty} = 0.15$ and $l_{\parallel}/\|l_{\parallel}\|_{\infty} = 0.85$. The density increase can explain the spike due to the ionization of neutrals entering the PFR. Furthermore, the magnitude of the ion temperature profiles have been reduced by $\sim 25\text{eV}$ for increased radiated power fraction. Moreover, the sudden increase in the Mach number close to the target $l_{\parallel}/\|l_{\parallel}\|_{\infty} \approx 0.2, 0.8$ implies the increase in flow due to ion conservation as ions are being born in the region below the dashed lines. In the PFR the dashed lines does not represent the X-points, but is used as a point of reference. The flow increase is stronger for $f_{\text{rad}} = 0.8$ than $f_{\text{rad}} = 0.2$. The middle of the field lines in the PFR is closest to the X-points indicated by the locations of the field lines with respect to the islands shown in Fig. 54.
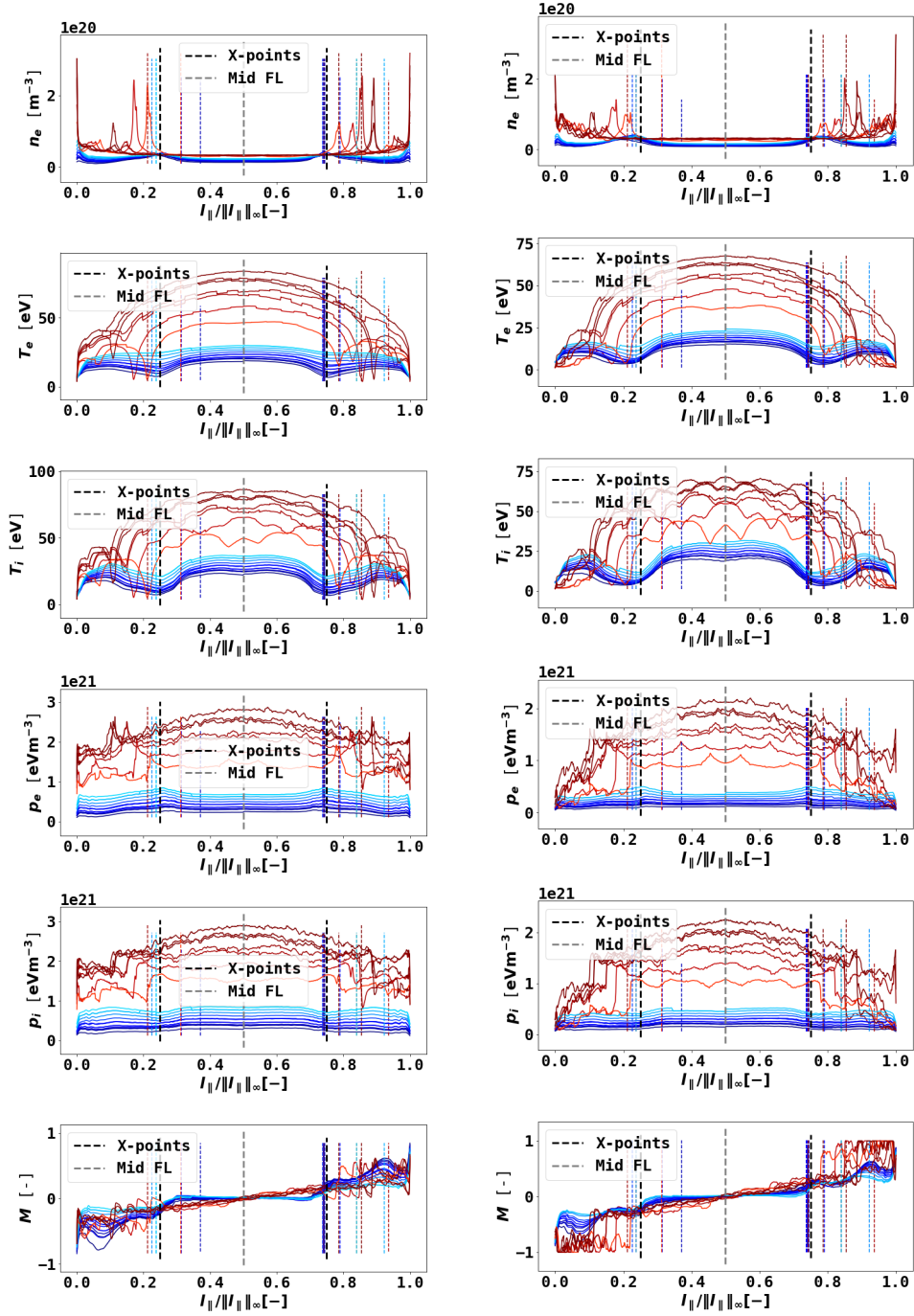
(.1) $f_{\mathrm{rad}} = 0.2$.

(.2) $f_{\mathrm{rad}} = 0.8$.

Figure 55: The ion and electron density, temperature and pressure field line profiles against temperature are shown for the two cases. The colour of the lines indicate the same field lines as in Fig. 54. The dashed lines correspond to the arclength selected by the index closest to 20% and 80% of the maximum index of the intersections between the field lines and the poloidal plane at $\phi = 2°$. These selected points are shown as the dots in Fig. 54. The black dashed lines labeled X-points at $l_{\parallel}/\|l_{\parallel}\|_{\infty} = 0.25$ and $l_{\parallel}/\|l_{\parallel}\|_{\infty} = 0.75$ are given as a reference.

(.1) $f_{\rm rad} = 0.2$ (.2) $f_{\rm rad} = 0.8$
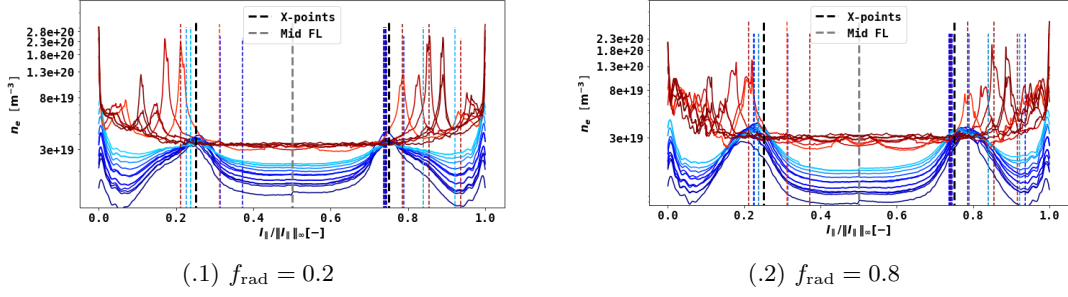
Figure 56: The logscaled electron density in the PFR.
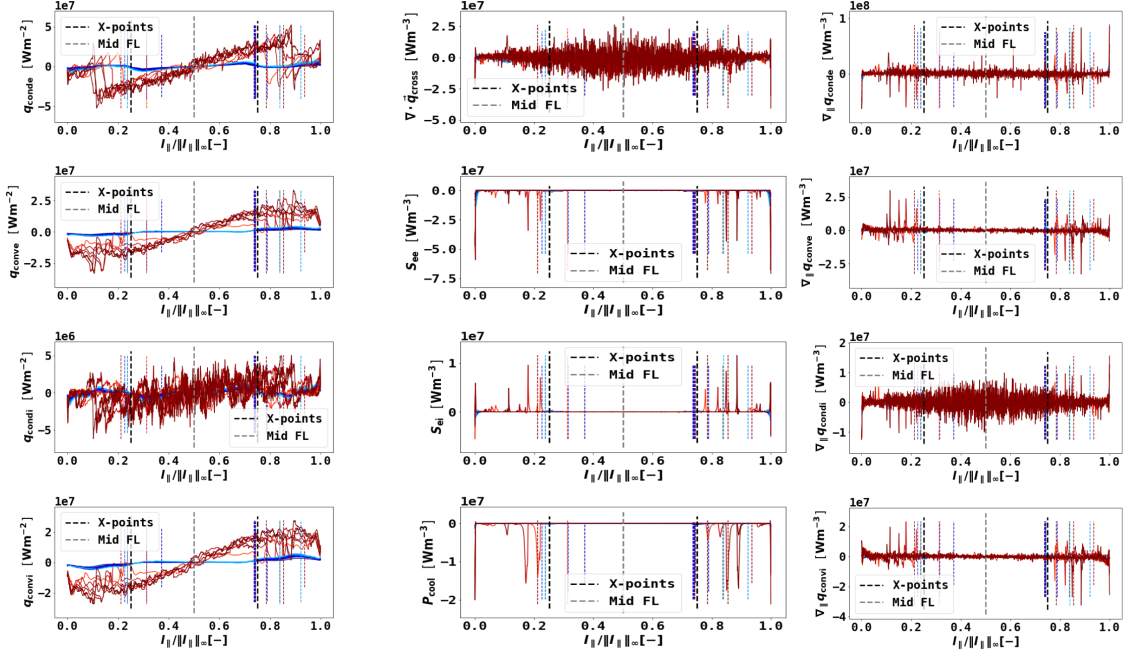
Figure 57: In the left column the profiles of the parallel ion and electron heat flux density along field lines against normalised arclength are shown. The middle column shows the divergence of the cross-field heat flux density and the sources and the sinks. The right column shows the parallel gradient of the heat flux density profiles from the left. All profiles are shown for the high radiation case where $f_{\rm rad} = 0.2$. The colour of the lines indicate the same field lines as in Fig. 54.

The heat flux density profiles shown in Fig. 57 and 58 also exhibit some characteristic differences. The magnitude of the parallel convective terms have been reduced by a factor ~ 2 and the magnitude of the parallel ion conductive term has been reduced by an order of magnitude. The main difference between the profiles shown in Figs. 57 and 58 and the profiles shown in Figs. 41 and 42 is the shape of the parallel electron conductive heat flux density profile. The slope of the temperature profiles of the field lines in the PFR are smaller in the region between the middle of the field line and the X-points leading to a weaker parallel temperature gradient. The effect is seen in the $q_{\|{\rm cond},e}$-profile where the slope is linear, so the $T_e^{5/2}$ seem to be compensated by the slope of the parallel temperature gradient in the region from the X-points to the targets. Furthermore, the ratio between the parallel conduction and convection shown in Fig. 59 shows that the convection channel is relatively larger for the $f_{\rm rad} = 0.8$ case than the $f_{\rm rad} = 0.2$ case.
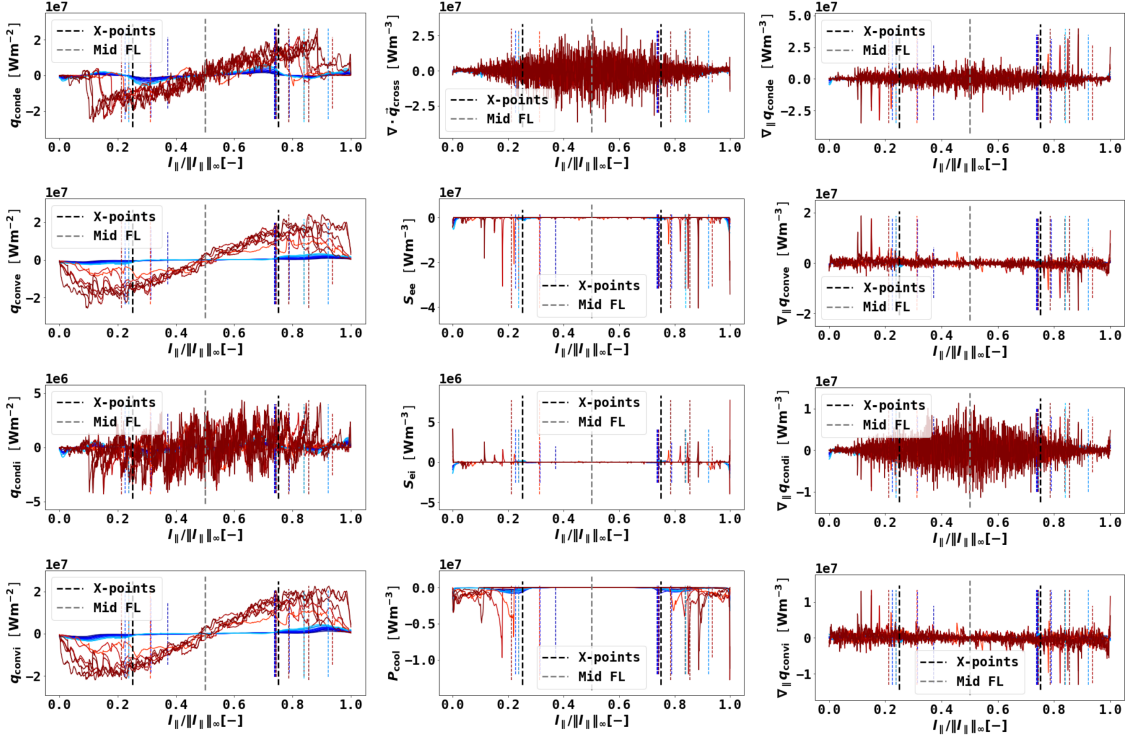
Figure 58: In the left column the ion and electron parallel heat flux density field line profiles against normalised arclength are shown. The middle column shows the divergence of the cross-field heat flux density and the sources and the sinks. The right column shows the parallel gradient of the heat flux density profiles from the left column. All profiles are shown for the high radiation case where $f_{\rm rad} = 0.8$. The colour of the lines indicate the same field lines as in Fig. 54.

(.1) $f_{\rm rad} = 0.2$ (.2) $f_{\rm rad} = 0.8$
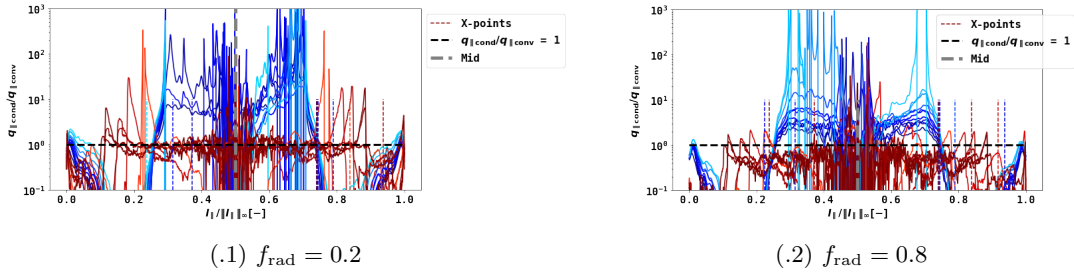
Figure 59: The ratio of between the parallel conduction and parallel convection in the PFR.

The integral terms normalised to $q^2_{\parallel,{\rm cond},e,{\rm u}}/2$ for the field lines in the PFR are shown in Fig. 60. The contribution from the parallel ion conductive transport is negligible. The contributions from I_B has increased and the convective terms have decreased. The left part of the field line ends up at the vertical target, whereas the right part ends up at the horizontal target as seen in Fig. 54. The convective losses are smaller for the left part of the field line attached to the vertical target than the right part attached to the horizontal target. The difference in the magnitude between the left and right part of the field line of the convective integral terms is larger for $f_{\rm rad} = 0.8$ than $f_{\rm rad} = 0.2$.
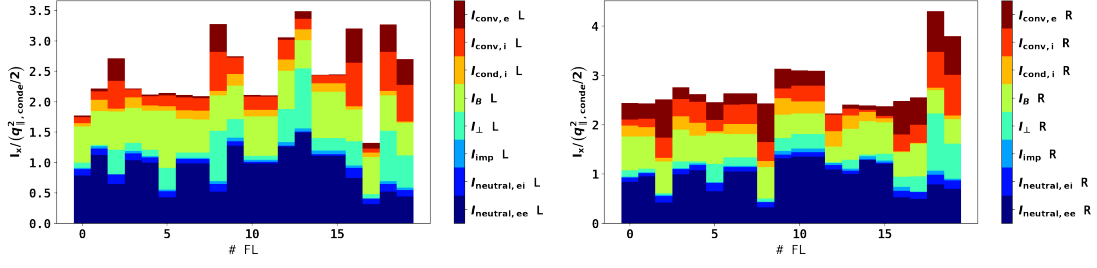
(.1) Integral terms for $f_{\text{rad}} = 0.2$.
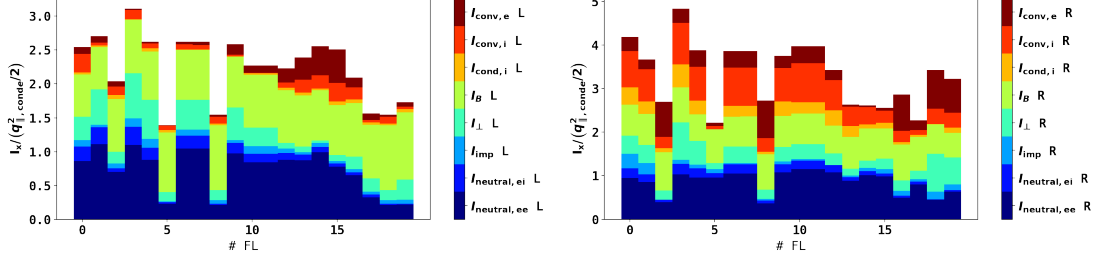
(.2) Integral terms for $f_{\text{rad}} = 0.8$.

Figure 60: The integral terms from Eqs. 46-51 which are terms of the integral of the complete heat flux density transport model given by equation 52. For each field line in the PFR the contribution of each term is shown. The field lines integrated for the plots are the same as in Fig. 54. The field lines are split in a left and right part the same way as the field lines in the SOL.

Moreover, the contribution from the radiation loss is insignificant and the neutral loss due to electron impact stands for ∼ 50% of the energy loss in the PFR. The impurity loss appears relatively small supposedly due to the shorter connection lengths of the field lines in the PFR as shown in Fig. 51, i.e. the radiation will have a limited time to dissipate power. The neutral loss is large because neutrals enter the PFR as shown in Fig. 61 and ionise at a larger part of the field line in the PFR compared to the field lines in the SOL as seen in Figs. 62 and 63. Furthermore, the plot shows that the neutral energy sources and sinks have a broader distribution when the radiated power fraction is increased.
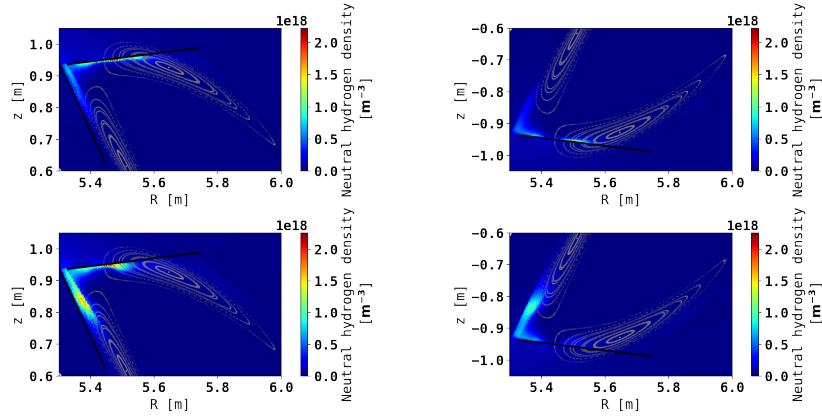
Figure 61: Neutral hydrogen distribution for poloidal cross-section at $\phi = 0°$. The low and high radiation case is plotted in the left and right, respectively.
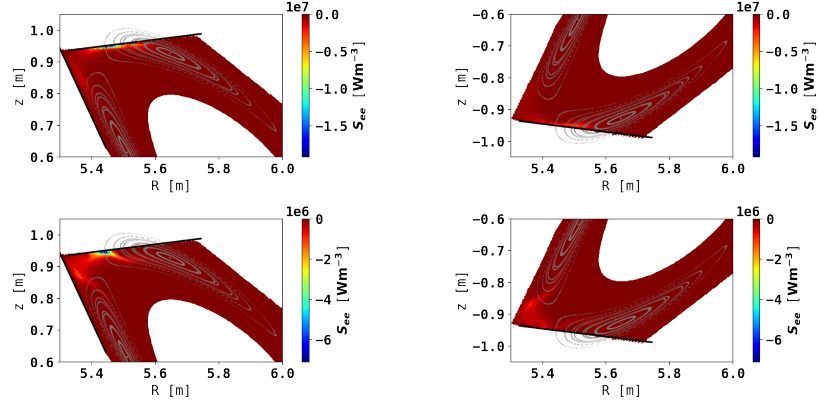
Figure 62: S_{ee} distribution for poloidal cross-section at $\phi = 0°$. The low and high radiation case is plotted in the left and right, respectively.
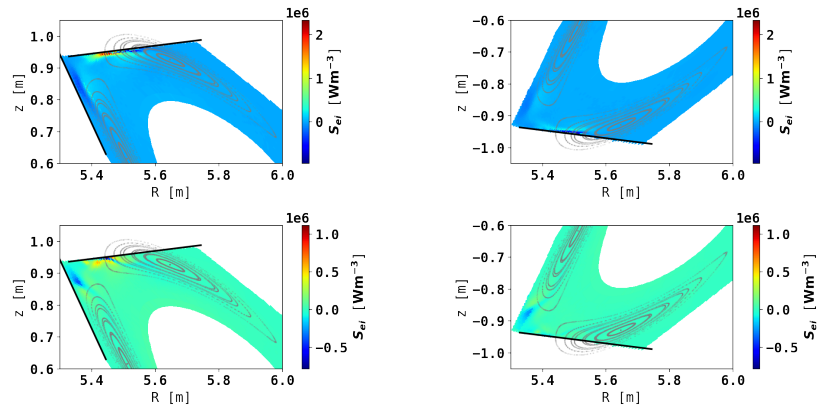
Figure 63: S_{ei} distribution for poloidal cross-section at $\phi = 0°$. The low and high radiation case is plotted in the left and right, respectively.

Considering that the only way that power enters the PFR is via cross-field transport it is strange that this contribution is not larger. However, the field lines never cross the separatrix and enter the PFR, but are already in the PFR. Thus, there is potentially a large contribution from cross-field transport that is not accounted for in Fig. 60 and the results needs to be viewed therein.
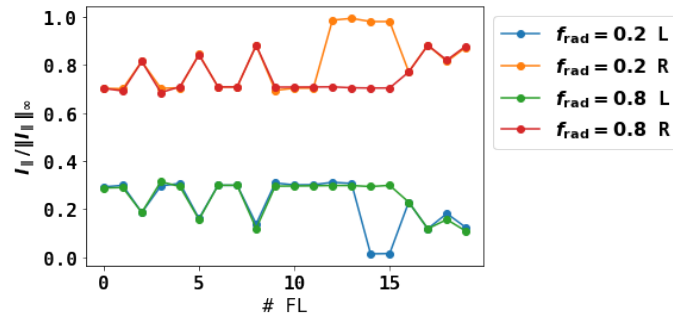
Figure 64: The upstream locations of the field lines in the PFR given in terms of the normalised arclength $l_\parallel / \|l_\parallel\|_\infty$.

The profiles of the parallel electron heat flux density shown in Figs. 57 and 58 have a different shape than the corresponding profiles in the SOL shown in Figs. 41 and 42. It builds up linearly

to around $l_\parallel/\|l_\parallel\|_\infty = 0.1$ and $l_\parallel/\|l_\parallel\|_\infty = 0.9$ where it drops to almost zero. Thus, the relative magnitude of the integral terms to $q^2_{\parallel\text{cond,u},e}/2$ is very sensitive to the upstream definition. The upstream locations with respect to the normalised arclength are plotted in Fig. 64. This is explains why some of the field lines does not show any loss due to impurity radiation as the impurity radiation is active only in the regions $l_\parallel/\|l_\parallel\|_\infty \in [0.1, 0.2]$ and $l_\parallel/\|l_\parallel\|_\infty \in [0.8, 0.9]$. Therefore, the integrand associated with the impurity radiation is small in that region. The upstream definition of these field lines are further downstream than the radiation region. Different upstream definitions gave unreasonable results when computing the normalised contributions of the integral terms $I_x/(q^2_{\parallel\text{cond,u},e}/2)$. This is important to consider when interpreting the results.

4.2.6 Alternative derivation with $q_\parallel$

As the results in Fig. 50 does not capture the energy loss due to impurity radiation an alternative assessment was done. Instead of focusing on $q_{\parallel,\text{cond},e}$ the field line integral from Eq. 52 can be derived by combining the equations for $\nabla_\parallel q_\parallel$ and $q_\parallel$ as opposed to combining Eqs. 42 and 43. Thus the complete derivation for the impurity concentration is:

$$(\nabla_\parallel \mathbf{q}_\parallel)q_\parallel = \left(S - \nabla_\perp \cdot \mathbf{q} + \frac{q_\parallel \nabla_\parallel B}{B} \right) q_\parallel$$

$$\nabla_\parallel \mathbf{q}_\parallel^2/2 =$$

$$\int_t^u dl_\parallel \nabla_\parallel \mathbf{q}_\parallel^2/2 = \int_t^u dl_\parallel (S_{\text{neutral}} + S_{\text{imp}} - \nabla_\perp \cdot \mathbf{q} + \frac{q_\parallel \nabla_\parallel B}{B})q_\parallel \tag{150}$$

$$S_{\text{imp}}q_\parallel = q_{\parallel\text{cond},e}n_e^2 c_\alpha L_\alpha + S_{\text{imp}}(q_{\parallel\text{conv}} + q_{\parallel\text{cond},i})$$

$$\int_t^u dl_\parallel q_{\parallel\text{cond},e}n_e^2 c_\alpha L_\alpha \approx \langle c_\alpha \rangle_t^u \int_t^u dl_\parallel q_{\parallel\text{cond},e}n_e^2 L_\alpha$$

$$\langle c_\alpha \rangle_t^u \int_t^u dl_\parallel q_{\parallel\text{cond},e}n_e^2 L_\alpha \approx q^2_{\parallel\text{u}}/2 - q^2_{\parallel\text{t}}/2 - I$$

$$\langle c_\alpha \rangle_t^u \approx \frac{q^2_{\parallel\text{u}}/2 - q^2_{\parallel\text{t}}/2 - I}{\int_t^u dl_\parallel q_{\parallel\text{cond},e}n_e^2 L_\alpha}$$

$$\langle c_\alpha \rangle_t^u \approx \frac{q^2_{\parallel\text{u}}/2 - q^2_{\parallel\text{t}}/2 - I}{\int_t^u dl_\parallel q_{\parallel\text{cond},e}n_e^2 L_\alpha} \tag{151}$$

where the integral term I is defined as:

$$I = \int_t^u dl_\parallel \left\{ \left(S_{\text{neutral}} + S_{\text{imp}} - \nabla_\perp \cdot \mathbf{q} + \frac{q_\parallel \nabla_\parallel B}{B} \right) q_\parallel - S_{\text{imp}}q_{\parallel\text{cond},e} \right\}. \tag{152}$$

Furthermore, the integral term I is decomposed:

$$I_{\text{neutral}} = \int_t^u dl_\parallel q_\parallel S_{\text{neutral}} \tag{153}$$

$$I_{\text{imp}} = \int_t^u dl_\parallel q_\parallel S_{\text{imp}} \tag{154}$$

$$I_\perp = \int_t^u dl_\parallel q_\parallel \nabla_\perp \cdot \mathbf{q} \tag{155}$$

$$I_B = \int_t^u dl_\parallel q_\parallel \frac{q_\parallel \nabla_\parallel B}{B} \tag{156}$$

$$I_{\text{imp,corr}} = \int_t^u dl_\parallel S_{\text{imp}}q_{\parallel\text{cond},e} \tag{157}$$

This gives bar plots which are comparable to Fig. 50.1, 50.2, 60.1 and 60.2. The results are shown in Figs. 65, 66, 67 and 68.
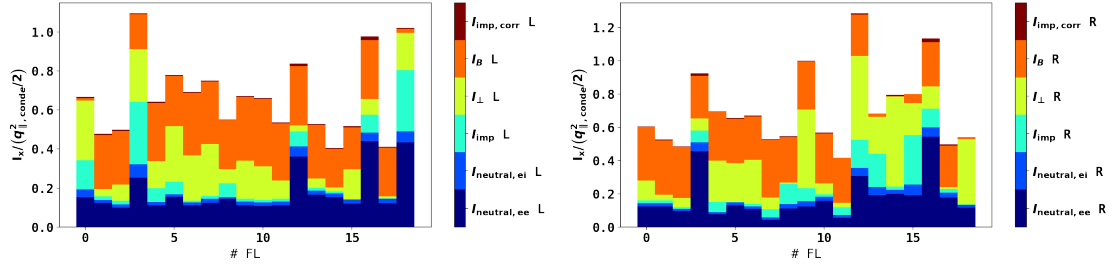
Figure 65: The integral terms from Eqs. 153 - 157 is shown normalised to $q_{\parallel}^2/2$ for $f_{\mathrm{rad}} = 0.2$ case for field lines in the SOL.
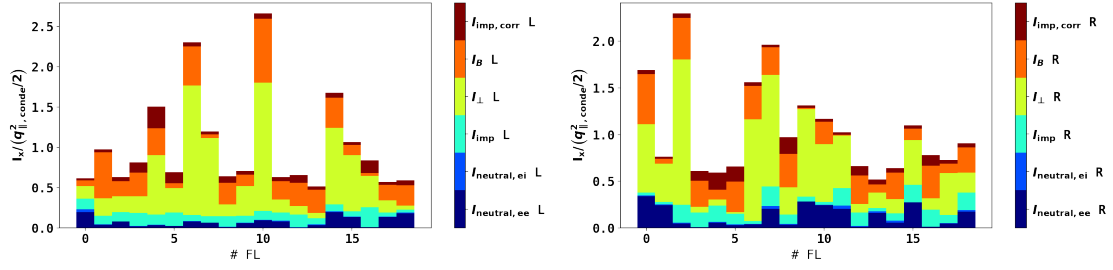
Figure 66: The integral terms from Eqs. 153 - 157 is shown normalised to $q_{\parallel}^2/2$ for $f_{\mathrm{rad}} = 0.8$ case for field lines in the SOL.
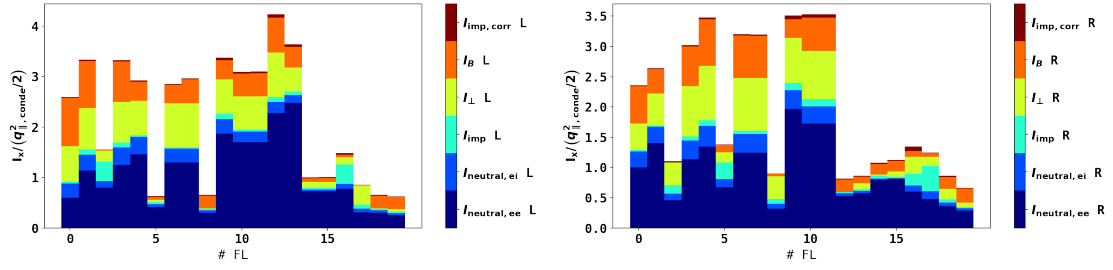
Figure 67: The integral terms from Eqs. 153 - 157 is shown normalised to $q_{\parallel}^2/2$ for $f_{\mathrm{rad}} = 0.2$ case for field lines in the PFR.
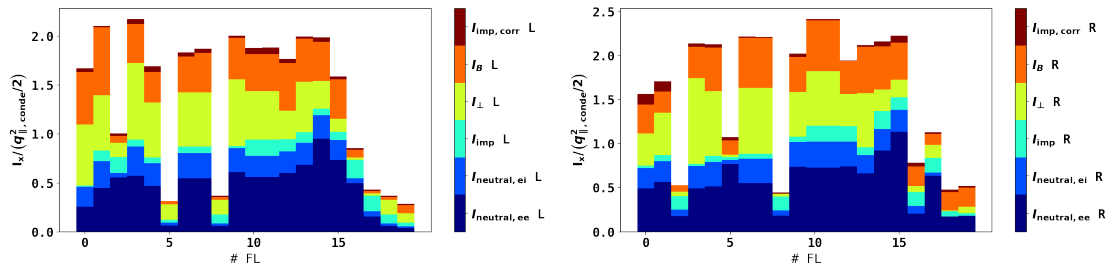
Figure 68: The integral terms from Eqs. 153 - 157 is shown normalised to $q_{\parallel}^2/2$ for $f_{\mathrm{rad}} = 0.8$ case for field lines in the PFR.

The results in Figs. 65 and 66 show similarities with the results in Figs. 50.1 and 50.2, and some significant differences. First, the radiation loss is better captured by the former and show consistent behaviour amongst the field lines. Furthermore, the I_B term is now significantly larger

and cannot be ignored. Second, the cross-field term $I_\perp$ is significant for $f_{\text{rad}} = 0.2$ and has the largest magnitude of all the terms for $f_{\text{rad}} = 0.8$. The neutral loss, have the same tendency of begin small when $f_{\text{rad}} = 0.8$ and is significant for the $f_{\text{rad}} = 0.2$ and insignificant for $f_{\text{rad}} = 0.8$. The results in Figs. 67 and 68 have similar features as the results from Figs. 60.1 and 60.2, but the cross-field term is now larger or the same magnitude as the I_B term. Furthermore, the results in Figs. 67 and 68 does not give insight in the importance of the parallel convective channels. The impurity losses are corrected by $I_{\text{imp,corr}}$ which appears to be larger for increased radiated power fraction in both the SOL and the PFR. The interpretation of $I_{\text{imp,corr}}$ is the power loss from the parallel electron conductive channel, which appears to be significant compared to the loss from the total parallel channel due to impurity radiation.

4.3 Impurity radiation weighted by impurity concentration

The baseline for the assessing the assumptions in the simplified models using the impurity concentration as a measure is the average impurity concentration from upstream to target weighted by the radiation distribution along the field line. The mean values and the profiles of the impurity concentration are shown in Fig. 69 for the SOL and in Fig. 70 for the PFR.

4.3.1 SOL

(.1) $f_{\text{rad}} = 0.2$.   (.2) $f_{\text{rad}} = 0.8$
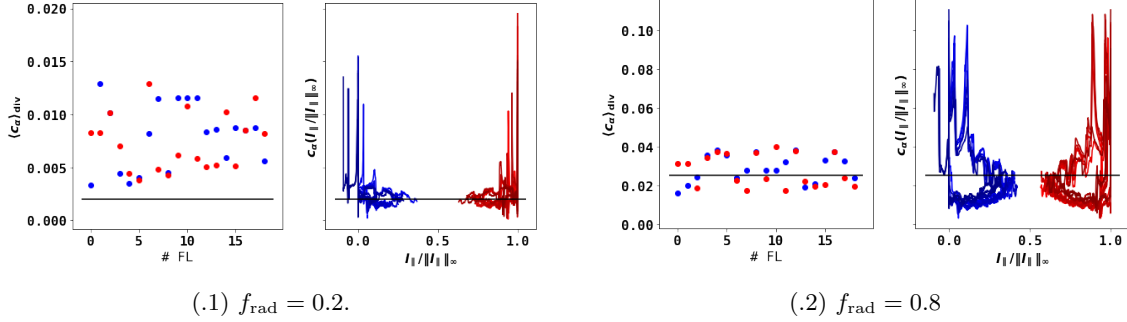
Figure 69: The impurity fraction profiles and the mean impurity fraction from upstream to target for each field line associated with the upper horizontal target are shown in the right and left plot, respectively, for $f_{\text{rad}} = 0.2$ in Fig. 69.1 and $f_{\text{rad}} = 0.8$ in Fig. 69.2. The mean divertor concentration is weighted by the impurity radiation intensity profile. The black horizontal line represent a constant impurity concentration of $c_\alpha = 0.025$.

4.3.2 PFR

(.1) $f_{\mathrm{rad}} = 0.2$ (.2) $f_{\mathrm{rad}} = 0.8$
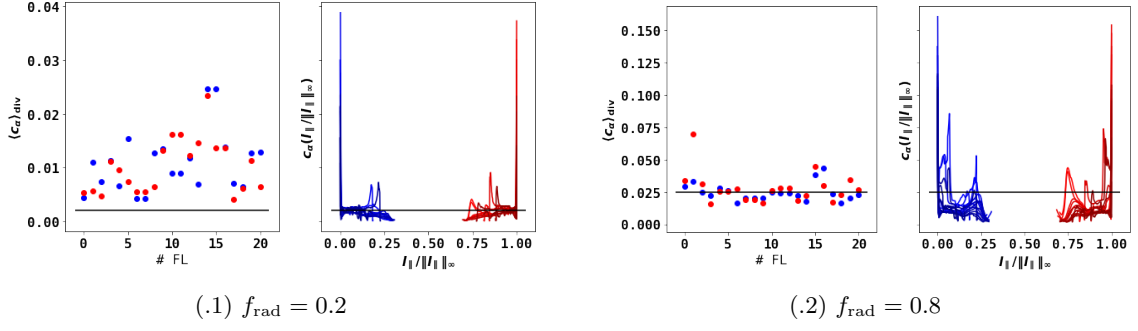
Figure 70: The impurity fraction profiles and the mean impurity fraction from upstream to target for each field line associated with the upper horizontal target are shown in the right and left plot, respectively, for $f_{\mathrm{rad}} = 0.2$ in Fig. 70.1 and $f_{\mathrm{rad}} = 0.8$ in Fig. 70.2. The mean divertor concentration is weighted by the impurity radiation intensity profile. The black horizontal line represent a constant impurity concentration of $c_\alpha = 0.025$.

4.4 Prediction from framework in the SOL

The approximation given in Eq. 91 is the impurity concentration computed by solving the fraction including all the integral terms given in Eqs. 46-51. From the step where the approximation is introduced, the assumptions are imposed on the approximated impurity concentration, and each step is represented by the term removed.

(.1) $f_{\mathrm{rad}} = .2$

(.2) The same as Fig. 71.1, but zoomed in on the y-axis.
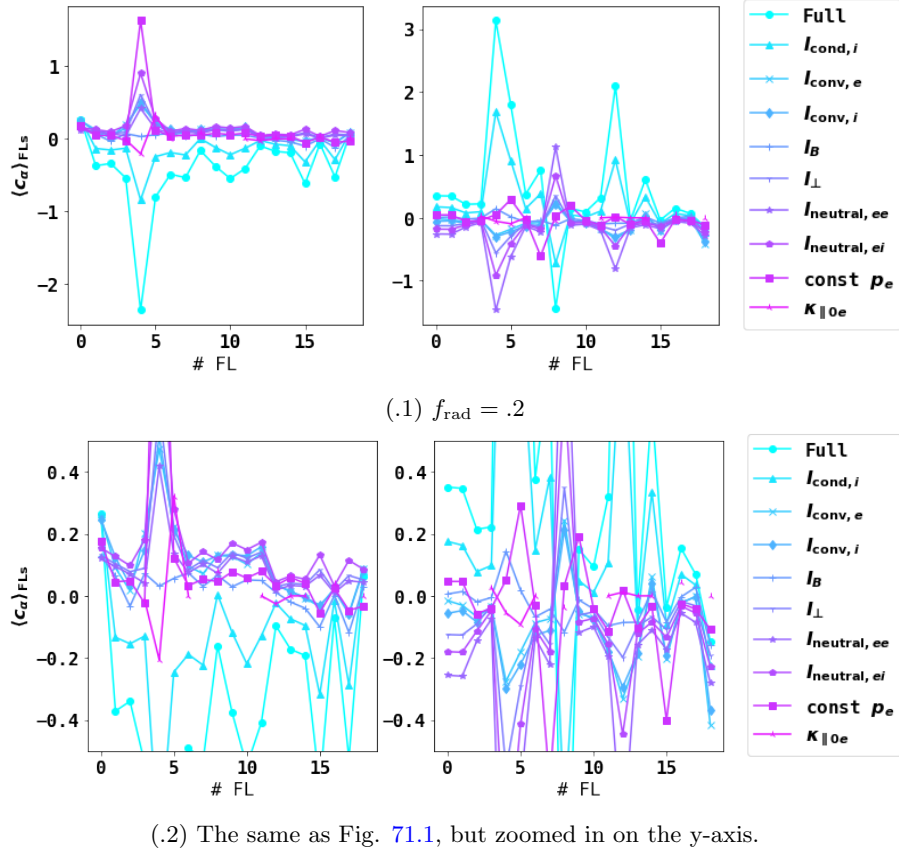
Figure 71: The prediction after imposing each assumption in the framework for each field line in the SOL for the low radiation case.

(.1) $f_{\rm rad} = 0.8$

(.2) The same as Fig. 72.1, but zoomed in on the y-axis.
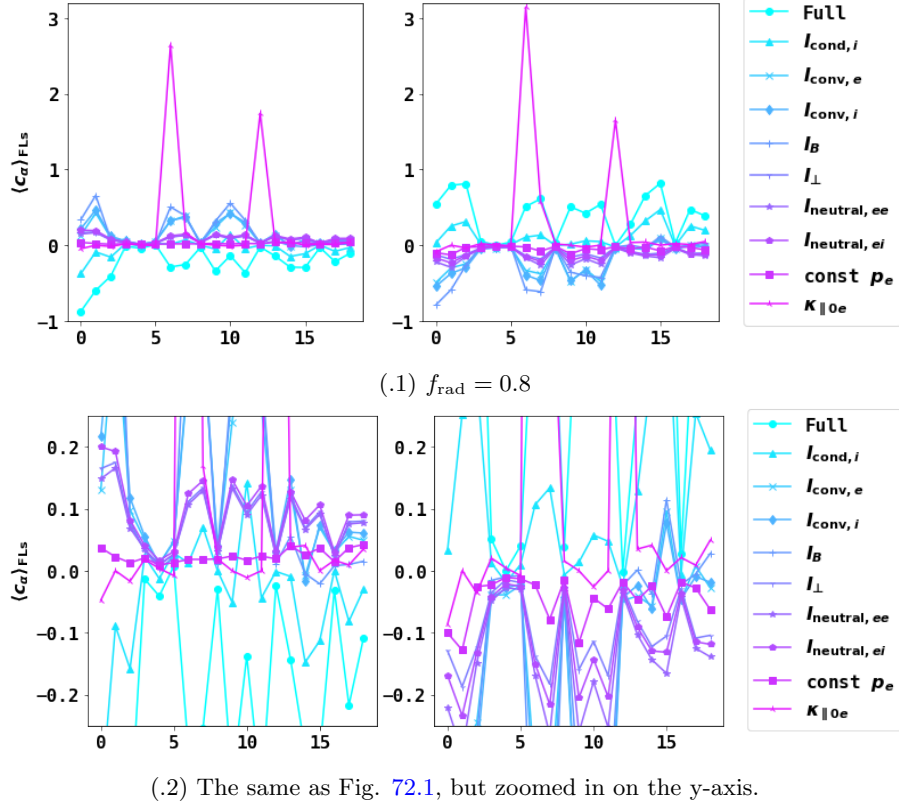
Figure 72: The prediction after imposing each assumption in the framework for each field line in the SOL for the low radiation case.

The scale of the results and the non-physical negative values of the predicted impurity concentration clearly shows that the results are unreasonable. Negative impurity concentrations implies that $q_{\parallel,{\rm cond},e,{\rm t}} > q_{\parallel,{\rm cond},e,{\rm u}}$ meaning energy is gained from upstream to target. Thus, the impurity concentration is predicted as being negative because the impurity radiation will function as a power source to compensate for a power gain from upstream to target. Furthermore, the expected concentration is much larger for the full model than the baseline shown in Fig. 69 and 70. The expected behaviour is that when a term is removed the impurity concentration will be overpredicted as observed in Moulton et al. (2021) [5]. The tendency is opposite in Fig. 71 and 72, i.e. the removal of a term causes underprediction of the impurity concentration needed for a given radiated power fraction. Furthermore, some of the values are negative. The large variation in the predicted impurity concentration can be due to the sensitivity of the upstream definition and that the inappropriate channel was used to derive the impurity concentration approximation. Thus, the unreasonable values of the impurity concentration left the open question if it is possible to use the impurity concentration as measure to assess the assumptions of the simplified models.

5 Conclusion and outlook

The assumptions of simplified models for the energy transport in the SOL of the W7-X island divertor in the standard configuration were assessed by comparing the relative magnitude of the terms involved in the product between the parallel heat flux densities and the sources and sinks integrated along the field line. Specifically, the loss from upstream to the target of the parallel electron conductive channel was derived from comparing with a similar analysis done previously by Moulton et al. (2021) [5]. Furthermore, it made it easier to assess each assumption imposed in Lengyel's model [6]. The loss from the parallel electron conductive channel was compared with the computed loss from the total parallel channel. Furthermore, assuming divertor-relevant field line pitch $\Theta \sim 10^{-3}$, the Feng model was reviewed by comparing the magnitude of the approximated cross-field and the projected parallel heat transport.

It is already clear from inspecting the heat flux density profiles, the global energy balance and the approximated cross-field heat flux densities that the energy transport is not conduction dominated nor dominated by parallel terms. Furthermore, the observed neutral losses in the SOL shown in Figs. 50.1 and 50.2 are significant compared to the radiation losses. However, the computed neutral losses in the SOL decrease for $f_{\mathrm{rad}} = 0.8$. The neutral losses in the PFR are significant for both cases. Thus, the results indicate the invalidity of assumed negligible neutral losses as a significant power loss in both the PFR and the SOL.

The dilution due to the variation of the magnetic field strength along the field lines is significant. However, this strongly depends on the integration bounds through the definition of upstream, which in this thesis is defined at the maximum of the parallel electron heat flux density, which is proportional to the magnetic field strength. Thus, the definition of upstream used in this thesis will most likely overestimate the contribution of the magnetic field strength dilution. Furthermore, the importance of this term is significantly larger in the PFR. So, since a lot of power enters the PFR via cross-field transport, it is a contribution that needs further investigation. In addition, the integrated terms for the PFR show a strong contribution from the neutral interaction, which is dominated by the loss due to electron impact. These observations are consistent for the field line integral representing the loss from upstream to target for the parallel electron conductive and total parallel channels. Thus, the loss due to neutral interaction cannot be ignored. Furthermore, since the field lines in the PFR have shorter connection lengths, as shown in Fig. 51, it is harder to remove power through impurity radiation. Thus, the power deposited at the targets in the PFR might be crucial to consider for the power exhaust handling.

The convective transport seems to dominate the loss from the parallel electron conductive channel, as shown in Figs. 50.1 and 50.2. The 2D profile of the approximated cross-field heat flux density shown in Fig. 33 also implies that the convective transport channel is important and even larger than the conductive channel. *Thus, the observations made in this thesis disagree with the assumption of conduction-dominated energy transport in the stellarator ID SOL locally.* However, if the poloidal and toroidal average of the heat flux is considered, the cross-field convective term is averaged out since it is characterized by both positive and negative regions along the poloidal direction. Thus, after averaging this term, the total heat flux agrees with the global energy analysis and Feng's results.

The loss from the parallel electron conductive channel as a measure to assess the assumptions of the simplified SOL energy transport models gave incomplete results as it did not capture the loss due to impurity radiation. Therefore, a similar computation was carried out for the derivation of the field line integral using the loss of the total parallel channel from upstream to target. The results show a more moderate total loss than the parallel electron conduction channel. For this computation, the dilution due to the magnetic field strength variation is significant in both cases. The contribution was large for $f_{\mathrm{rad}} = 0.2$, but smaller for $f_{\mathrm{rad}} = 0.8$. Furthermore, the cross-field term was observed to be significant for $f_{\mathrm{rad}} = 0.2$, and dominant of the total loss for $f_{\mathrm{rad}} = 0.8$. The neutral loss due to electron impact is significant at $f_{\mathrm{rad}} = 0.2$, but decreases significantly for $f_{\mathrm{rad}} = 0.8$. This observation is consistent with the other alternative computation of the field line integral terms. The neutral loss due to ion impact was also negligible in the SOL but significant in the PFR. The impurity loss is now consistently present for all field lines and the contribution is larger for $f_{\mathrm{rad}} = 0.8$ than $f_{\mathrm{rad}} = 0.2$, as expected. However, it is still unexpectedly low, which

highlights a major weakness of the framework as the radiation loss was expected to be consistent with chosen radiated power fraction for the simulations.

5.1   Outlook

Cross-field transport was observed to be significant and even dominating in some regions. Thus, to address the problem of simplifying SOL energy transport models in the future using EMC3-EIRENE simulations for the W7-X ID SOL, an island-aligned grid that allows computing of the normal and binormal components of the cross-field transport should be generated. Furthermore, the island-aligned grid will enable an accurate comparison of the cross-field and parallel terms through the divertor-relevant field line pitch, which can be computed for field lines traced with such a grid. It will also give additional detailed insight into the transport properties of the SOL.

The Monte Carlo approach the EMC3-EIRENE code is based on is inherently noisy, so more work should be done to identify if there are significant errors in the profiles and if they are statistical. The gradients, divergence terms, sources, and sinks can suffer from low noise levels. So, we suggest a noise study to eliminate or confirm if there are statistical errors that affect the integrals along field lines. The noise study should focus on asymmetries in the integrand profiles because asymmetries tend to increase the area under the curve. If statistical noise is a source of error, the suggested course of action is to smooth the profiles. There are several ways of smoothing the profiles, but the priority should be to average over many iterations for converged simulation cases for a beneficial cost-gain ratio. Furthermore, the profiles can be smoothed in post-processing by interpolating field lines. Interpolation of profiles along field lines was attempted, but a smooth profile could not be obtained without altering the physics of the profiles. So, the challenging task is to separate the profiles' physics and the statistical noise. Furthermore, the field line profiles are discontinuous due to the mapping surface at the triangular cross-sections. The discontinuity can be handled by increasing the grid resolution, but this also implies that one has to increase the total number of particles in the EMC3 simulations to maintain approximately the same amount of particles in the grid cells. If the increase in grid resolution is not compensated by increasing the number of particles within a cell, the scalar and vector fields will be noisier. The required compensation implies that the primary sources of error are coupled. Thus, compensating for these errors is computationally expensive.

The concentration prediction was computed but gave unreasonable results. The origin of the unreasonable predictions is unclear, but some probable candidates exist. First, the sensitivity of the definition of upstream can significantly impact the value of the integral terms. An effect of defining the upstream location is that the integrand is cut such that the profile's left and right parts exhibit an asymmetry. Asymmetries lead to arbitrary integral values as the integral strongly depends on the integration bounds. Another source of error can be the choice of measure used for computing the concentration. The suggested course of action is to do a similar analysis with the integral from target to upstream of $q\nabla_r q$ where the subscript r indicates the radial direction of the corresponding toroidal coordinate system. This derivation is similar to the Feng model but includes convection. The integral $\int_t^u q\nabla_r q dr$ is then interpreted as the total heat flux density loss from upstream to downstream, and see if the approximated impurity concentration improves. Furthermore, as the cross-field convective channel was significantly larger than other channels, it should be attempted to compute this integral under the assumption of dominant cross-field convection. If assuming dominant convection for $\int_t^u q\nabla_r q dr$ gives good results, this would greatly simplify the energy transport model. However, deriving a radiation scaling requires removing the neutral sources that are currently significant, as including this in the energy transport model gives an expression which is too complex.

Appendix

Bibliography

[1] Yuhe Feng, M Jakubowski, R König, M Krychowiak, M Otte, F Reimold, D Reiter, O Schmitz, D Zhang, CD Beidler, et al. Understanding detachment of the w7-x island divertor. *Nuclear Fusion*, 61(8):086012, 2021.

[2] T Pütterich. Investigations on spectroscopic diagnostic of high-z elements in fusion plasmas. Technical report, Max-Planck-Institut für Plasmaphysik, 2006.

[3] Josefine Henriette Elise Proll. *Trapped-particle instabilities in quasi-isodynamic stellarators*. PhD thesis, Ernst-Moritz-Arndt-Universität Greifswald, 2014.

[4] Y Feng, F Sardei, P Grigull, K McCormick, J Kisslinger, and D Reiter. Physics of island divertors as highlighted by the example of w7-as. *Nuclear fusion*, 46(8):807, 2006.

[5] David Moulton, PC Stangeby, X Bonnin, and RA Pitts. Comparison between solps-4.3 and the lengyel model for iter baseline neon-seeded plasmas. *Nuclear Fusion*, 61(4):046029, 2021.

[6] LL Lengyel. Analysis of radiating plasma boundary layers. Technical report, Max-Planck-Institut für Plasmaphysik, 1981.

[7] D Post, N Putvinskaya, FW Perkins, and W Nevins. Analytic criteria for power exhaust in divertors due to impurity radiation. *Journal of nuclear materials*, 220:1014–1018, 1995.

[8] Peter C Stangeby et al. *The plasma boundary of magnetic fusion devices*, volume 224. Institute of Physics Pub. Philadelphia, Pennsylvania, 2000.

[9] Jeffrey Freidberg. *Plasma Physics and Fusion Energy*, volume 1. Cambridge University Press, 2008.

[10] W Fundamenski and OE Garcia. Comparison of coulomb collision rates in the plasma physics and magnetically confined fusion literature. *Report No. EFDA-JET-R (07) 01*, 2007.

[11] JH You, E Visca, Ch Bachmann, T Barrett, F Crescenzi, M Fursdon, H Greuner, D Guilhem, P Languille, M Li, et al. European demo divertor target: Operational requirements and material-design interface. *Nuclear materials and Energy*, 9:171–176, 2016.

[12] Kai Henrik Nordlund et al. European research roadmap to the realisation of fusion energy. *EUROfusion*, 2018.

[13] JH You, G Mazzone, E Visca, H Greuner, M Fursdon, Y Addab, C Bachmann, T Barrett, U Bonavolontà, B Böswirth, et al. Divertor of the european demo: Engineering and technologies for power exhaust. *Fusion Engineering and Design*, 175:113010, 2022.

[14] KC Hammond, Yu Gao, M Jakubowski, C Killer, H Niemann, L Rudischhauser, A Ali, T Andreeva, BD Blackwell, Kai-Jakob Brunner, et al. Drift effects on w7-x divertor heat and particle fluxes. *Plasma Physics and Controlled Fusion*, 61(12):125001, 2019.

[15] Herbert Goldstein, Charles Poole, and John Safko. *Classical mechanics*. American Association of Physics Teachers, 2002.

[16] F Effenberg, S Brezinsek, Y Feng, R König, M Krychowiak, M Jakubowski, H Niemann, V Perseo, O Schmitz, D Zhang, et al. First demonstration of radiative power exhaust with impurity seeding in the island divertor at wendelstein 7-x. *Nuclear Fusion*, 59(10):106020, 2019.

[17] S Brezlnsek, Chandra Prakash Dhard, Marcin Jakubowski, Ralf König, Suguru Masuzaki, Matej Mayer, Dirk Naujoks, Juri Romazanov, Klaus Schmid, Oliver Schmitz, et al. Plasma–surface interaction in the stellarator w7-x: conclusions drawn from operation with graphite plasma-facing components. *Nuclear Fusion*, 62(1):016006, 2021.

[18] J Boscary, R Stadler, A Peacock, F Hurd, A Vorköper, B Mendelevitch, A Cardella, H Pirsch, H Tittes, J Tretter, et al. Design and technological solutions for the plasma facing components of wendelstein 7-x. *Fusion Engineering and Design*, 86(6-8):572–575, 2011.

[19] N Asakura, K Hoshino, S Kakudate, F Subba, C Vorpahl, Y Homma, H Utoh, Y Someya, Y Sakamoto, R Hiwatari, et al. Power exhaust concepts and divertor designs for japanese and european demo fusion reactors. *Nuclear Fusion*, 61(12):126057, 2021.

[20] F Sardei, Y Feng, P Grigull, G Herre, D Hildebrandt, JV Hofmann, J Kisslinger, R Brakel, J Das, J Geiger, et al. Island divertor studies on w7-as. *Journal of nuclear materials*, 241: 135–148, 1997.

[21] T Sunn Pedersen, Matthias Otte, Samuel Lazerson, Per Helander, S Bozhenkov, Christoph Biedermann, T Klinger, Robert C Wolf, and H-S Bosch. Confirmation of the topology of the wendelstein 7-x magnetic field to better than 1: 100,000. *Nature communications*, 7(1):1–10, 2016.

[22] Allen H Boozer. Non-axisymmetric magnetic fields and toroidal plasma confinement. *Nuclear Fusion*, 55(2):025001, 2015.

[23] William D D'haeseleer, William NG Hitchon, James D Callen, and J Leon Shohet. *Flux coordinates and magnetic field structure: a guide to a fundamental tool of plasma theory.* Springer Science & Business Media, 2012.

[24] Allen H Boozer. Physics of magnetically confined plasmas. *Reviews of modern physics*, 76(4): 1071, 2005.

[25] M Jakubowski, M Endler, Y Feng, Y Gao, C Killer, R König, M Krychowiak, V Perseo, F Reimold, O Schmitz, et al. Overview of the results from divertor experiments with attached and detached plasmas at wendelstein 7-x and their implications for steady-state operation. *Nuclear Fusion*, 61(10):106003, 2021.

[26] F Sardei, Y Feng, J Kisslinger, P Grigull, R Koenig, and K McCormick. Island divertor: Concepts and status of experimental and modelling results. Technical report, W7-AS Team, 2001.

[27] D Zhang, R König, Y Feng, R Burhenn, S Brezinsek, M Jakubowski, B Buttenschön, H Niemann, A Pavone, M Krychowiak, et al. First observation of a stable highly dissipative divertor plasma regime on the wendelstein 7-x stellarator. *Physical review letters*, 123(2):025002, 2019.

[28] Takashi Fujimoto. Plasma spectroscopy. In *Plasma Polarization Spectroscopy*, pages 29–49. Springer, 2008.

[29] Hugh P Summers. The ionization equilibrium of hydrogen-like to argon-like ions of elements. *Monthly Notices of the Royal Astronomical Society*, 169(3):663–680, 1974.

[30] Hugh P Summers. The recombination and level populations of ions ii. resolution of angular momentum states. *Monthly Notices of the Royal Astronomical Society*, 178(2):101–122, 1977.

[31] HP Summers, NR Badnell, MG O'Mullane, AD Whiteford, R Bingham, BJ Kellett, J Lang, KH Behringer, Ursel Fantz, KD Zastrow, et al. Atomic data for modelling fusion and astrophysical plasmas. *Plasma physics and controlled fusion*, 44(12B):B323, 2002.

[32] HP Summers, WJ Dickson, MG O'mullane, NR Badnell, AD Whiteford, DH Brooks, J Lang, SD Loch, and DC Griffin. Ionization state, excited populations and emission of impurities in dynamic finite density plasmas: I. the generalized collisional–radiative model for light elements. *Plasma Physics and Controlled Fusion*, 48(2):263, 2006.

[33] HP Summers and MG O'Mullane. Atomic data and modelling for fusion: the adas project. In *AIP Conference Proceedings*, volume 1344, pages 179–187. American Institute of Physics, 2011. URL https://open.adas.ac.uk/about-open-adas.

[34] H Frerichs, Y Feng, X Bonnin, RA Pitts, D Reiter, and O Schmitz. Volumetric recombination in emc3-eirene: Implementation and first application to the pre-fusion power operation phase in iter. *Physics of Plasmas*, 28(10):102503, 2021.

[35] SC Liu, Y Liang, P Drews, C Killer, A Knieps, GS Xu, HQ Wang, N Yan, X Han, D Höschen, et al. The effects of magnetic topology on the scrape-off layer turbulence transport in the first divertor plasma operation of wendelstein 7-x using a new combined probe. *Nuclear fusion*, 59 (6):066001, 2019.

[36] Carsten Killer, Yann Narbutt, Olaf Grulke, et al. Turbulent transport in the scrape-off layer of wendelstein 7-x. *Nuclear Fusion*, 61(9):096038, 2021.

[37] David Bold, Felix Reimold, Holger Niemann, Yu Gao, Marcin Jakubowski, Carsten Killer, Victoria R Winters, et al. Impact of transport models on local measurements in w7-x using synthetic diagnostics with emc3-eirene and comparison to experimental observations in the w7-x island scrape-off layer. *arXiv preprint arXiv:2201.06341*, 2022.

[38] Y Feng, F Sardei, P Grigull, K McCormick, J Kisslinger, D Reiter, and Y Igitkhanov. Transport in island divertors: physics, 3d modelling and comparison to first experiments on w7-as. *Plasma physics and controlled fusion*, 44(5):611, 2002.

[39] David Robert Bates, AE Kingston, and RW Pt McWhirter. Recombination between electrons and atomic ions, i. optically thin plasmas. *Proceedings of the Royal Society of London. Series A. Mathematical and Physical Sciences*, 267(1330):297–312, 1962.

[40] Y Feng, F Sardei, and J Kisslinger. 3d fluid modelling of the edge plasma by means of a monte carlo technique. *Journal of nuclear materials*, 266:812–818, 1999.

[41] Y Feng, F Sardei, J Kisslinger, P Grigull, K McCormick, and D Reiter. 3d edge modeling and island divertor physics. *Contributions to Plasma Physics*, 44(1-3):57–69, 2004.

[42] SI Braginskii. Transport processes in a plasma. *Reviews of plasma physics*, 1, 1965.

[43] Yühe Feng, F Sardei, J Kisslinger, and P Grigull. A 3d monte carlo code for plasma transport in island divertors. *Journal of nuclear materials*, 241:930–934, 1997.

[44] M Kobayash, D Reiter, D Reiser, KH Finken, Y Feng, and F Sardei. Implementation of the emc3-eirene code on textor-ded: accuracy and convergence study. *Contributions to Plasma Physics*, 44, 2004.

[45] Y Feng, F Sardei, and J Kisslinger. A simple highly accurate field-line mapping technique for three-dimensional monte carlo modeling of plasma edge transport. *Physics of plasmas*, 12(5): 052505, 2005.

[46] Nicolaas Godfried Van Kampen. *Stochastic processes in physics and chemistry*, volume 1. Elsevier, 1992.

[47] Jeanne Pellerin, Kilian Verhetsel, and Jean-FranÇois Remacle. There are 174 subdivisions of the hexahedron into tetrahedra. *ACM Transactions on Graphics (TOG)*, 37(6):1–9, 2018.

[48] Sergey A Bozhenkov, Joachim Geiger, Michael Grahl, Johann Kisslinger, Andreas Werner, and Robert C Wolf. Service oriented architecture for scientific analysis at w7-x. an example of a field line tracer. *Fusion Engineering and Design*, 88(11):2997–3006, 2013.

[49] SS Abdullaev. On mapping models of field lines in a stochastic magnetic field. *Nuclear Fusion*, 44(6):S12, 2004.

[50] Douglass Edmund Post, RV Jensen, CB Tarter, WH Grasberger, and WA Lokke. Steady-state radiative cooling rates for low-density, high-temperature plasmas. *Atomic data and nuclear data tables*, 20(5):397–439, 1977.

[51] PG Carolan and VA Piotrowicz. The behaviour of impurities out of coronal equilibrium. *Plasma Physics*, 25(10):1065, 1983.

[52] Y Feng, M Kobayashi, T Lunt, and D Reiter. Comparison between stellarator and tokamak divertor transport. *Plasma physics and controlled fusion*, 53(2):024009, 2011.

[53] Thomas Eich, AW Leonard, RA Pitts, W Fundamenski, Robert James Goldston, TK Gray, A Herrmann, A Kirk, A Kallenbach, O Kardaun, et al. Scaling of the tokamak near the scrape-off layer h-mode power width and implications for iter. *Nuclear fusion*, 53(9):093031, 2013.

[54] Robert James Goldston. Heuristic drift-based model of the power scrape-off width in low-gas-puff h-mode tokamaks. *Nuclear Fusion*, 52(1):013009, 2011.

[55] Robert James Goldston, ML Reinke, and JA Schwartz. A new scaling for divertor detachment. *Plasma Physics and Controlled Fusion*, 59(5):055015, 2017.

[56] Ralph Dux. Strahl user manual. Technical report, Max-Planck-Institut für Plasmaphysik, 2006.

[57] Y Feng, F Sardei, J Kisslinger, P Grigull, K McCormick, D Reiter, L Giannone, R König, N Ramasubramanian, H Thomsen, et al. Physics of the geometry-related detachment stability in w7-as. *Nuclear fusion*, 45(2):89, 2005.

[58] V Perseo, V Winters, Y Feng, F Reimold, OP Ford, R König, SA Bozhenkov, KJ Brunner, R Burhenn, P Drewelow, et al. 2d measurements of parallel counter-streaming flows in the w7-x scrape-off layer for attached and detached plasmas. *Nuclear Fusion*, 61(11):116039, 2021.